# 國立交通大學

# 資訊科學與工程研究所

# 博 士 論 文

知覺式音訊編碼壓縮瑕疵之探討

Compression Artifacts in Perceptual Audio Coding

研 究 生：許瀚文

指導教授：劉啟民　教授

中 華 民 國 九 十 九 年 一 月

知覺式音訊編碼壓縮瑕疵之探討

# Compression Artifacts in Perceptual Audio Coding

研 究 生：許瀚文　　　　　Student：Han-Wen Hsu

指導教授：劉啟民　　　　　Advisor：Dr. Chi-Min Liu

國 立 交 通 大 學
資 訊 科 學 與 工 程 研 究 所
博 士 論 文

A Dissertation
Submitted to Institute of Computer Science and Engineering
College of Computer Science
National Chiao Tung University
in partial Fulfillment of the Requirements
for the Degree of Doctor of Philosophy
in
Computer Science and Engineering

January 2010

Hsinchu, Taiwan, Republic of China

中華民國九十九年一月

# 知覺式音訊編碼壓縮瑕疵之探討

學生：許瀚文　　　　　　　　　　　指導教授：劉啟民 博士

國立交通大學　資訊科學與工程研究所

## 中文論文摘要

知覺式音訊編碼利用與聽覺無關的訊號內容以及資料的累贅性來達到高壓縮率。先進與精良的訊號處理使得 知覺式音訊編碼 造成了與傳統壓縮失真相當不同的編碼瑕疵 (artifacts)。新的音訊技術的成熟需經過對其所引入的編碼瑕疵進行成功的建模、量測與控制。隨著例如 Advanced Audio Coding (AAC), Spectral Band Replication (SBR)與參數編碼等最先進的編碼技術的進步，其編碼瑕疵的建模、量測與控制的困難度遠高於對先前編碼法上的瑕疵。本論文將就原理、產生來源、知覺影響與相關消除法等面向來探討這些新的編碼瑕疵。我們針對 MPEG 音訊編碼，包括 MP3、AAC、SBR、PS (Parametric Stereo coding)，來探討由新技術所引入的編碼瑕疵。我們透過時頻圖來具體化可聽瑕疵、考慮容易觸發瑕疵的音訊種類、分析關鍵編碼器模組，並提供實例驗證。我們提出一種頻譜修補的方法來改善兩種零量化瑕疵，與一種快速奇基數演算法來計算濾波堆中第四型餘弦轉換來控制數值失真與平行運算。我們建立 AAC 上的時域雜訊朔型法(TNS)的公式化描述，並考慮一項已知的時域假頻雜訊瑕疵。最後我們考慮 SBR 與 PS 編碼法上新型態的編碼瑕疵，並驗證了 SBR 所採用的線性預測法的預測偏差。

Compression Artifacts in Perceptual Audio Coding

Student: Han-Wen Hsu                    Advisor: Dr. Chi-Min Liu

Institute of Computer Science and Engineering
National Chiao Tung University

## ABSTRACT

Perceptual audio coding achieves a high compression ratio by exploiting perceptual irrelevance and data redundancy. By using advanced and sophisticated signal processing methods, perceptual audio coding has generated artifacts that are quite different from the traditional distortions. A new audio technology becomes mature through the successful modeling, measuring and control on the artifacts incurred from the technology. With the advance of new coding modules in the state-of-the-art coding methods such as Advanced Audio Coding (AAC), Spectral Band Replication (SBR), and parametric coding, the incurred artifacts are far more difficult to model, measure and control than those caused by previous encoding systems like pulse code modulation. In this dissertation, we take into consideration the MPEG audio, including MP3, AAC, SBR and PS (Parametric Stereo) coding, to explore the compression artifacts from the novel coding methods in terms of principle, generation sources, perception, and related relief methods. We model the audible artifacts through the time-frequency diagrams; consider the artifacts-susceptible music types; analyze the critical encoding technologies incurring these artifacts; and provide empirical verifications for the artifacts. Specifically, we propose an audio patch method for reducing the two zero-quantization artifacts and the fast odd-radix algorithm for computing the type-IV discrete cosine transform in the filterbank computation for breaking the tradeoff of parallelism and numerical distortion in the existing methods. We establish the compact forms for the Temporal Noise Shaping (TNS) in AAC and consider the known artifact named the

time-domain aliasing noise. New kinds of artifacts are explored for SBR and PS. We also

demonstrate the predictive bias of the linear prediction used in SBR.
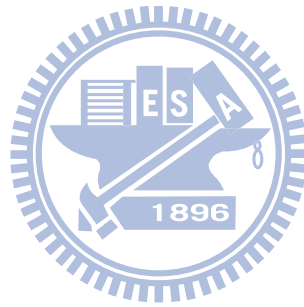
# 誌謝

　　本論文的完成，感謝劉啓民老師所提供的指導與支持，老師學術經驗的大力傳承使我得以進入研究大門 。研究室七年半來 我所共事的每一位學長、同學以及學弟們，謝謝你們在研究與生活上的協助。

　　兩位姑姑與父母的養育之恩，以及家族長輩的照顧，你們的恩情無法言盡。感謝許家眾多兄弟姊妹們的關心與幫忙。

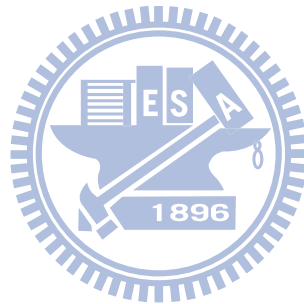　　最後，謝謝所有幫助過我的師長與朋友。

# TABLE OF CONTENTS

# LIST OF TABLES

# LIST OF FIGURES

# CHAPTER 1
# INTRODUCTION

Digital audio coding is a major technology in the multimedia industry. Significant advances in audio compression have facilitated the development of numerous applications, including audio storage, digital audio broadcasting (DAB), mobile applications and Internet streaming video. In addition to the traditional audio coders, such as MPEG-1 Layer-III (MP3) [1], MPEG-2/4 Advanced Audio Coding (AAC) [2], [3] and Dolby Adaptive Transform Coder 3 (AC-3), some state-of-the-art coding methods, such as Spectral Band Replication (SBR) [5]-[9] and spatial audio coding [10]-[17], have been developed to achieve near-transparent CD-quality at very low bit rates.

Advances in recording technologies in the audio industry have led to distortions like wow&flutter, tape saturation, crosstalk, aliasing, quantization nonlinearity, underwater feeling, ringing, drop-outs and metal hissing [18]. Understanding these artifacts has motivated researches on audio restoration, audio enhancement, filter bank design, and objective quality evaluation. Likewise, perceptual audio coding [19] has incurred various annoying artifacts such as pre-echo, birdies, speech reverberation, binaural masking level difference (BLMD) effect and stereo image loosening [18]. The adoption of new coding technologies has led to more "complex" artifacts challenging audio modeling, measuring and listening. To achieve high audio quality, knowing these artifacts is of priority concern in encoder design, post-processing, and understanding the limitations of compression methods. In this dissertation, we aim to explore the audible artifacts from new coding methods.

## 1.1. Technology Evolution of Perceptual Audio Coding

In the technology evolution of perceptual audio coding, the early effort was made to

exploit the psychoacoustic knowledge for the rate-distortion control and to scale the time-frequency resolution of filterbank [19]-[22]. After the success of conventional frequency-domain audio coders such as AC-3, MP3 and AAC, many researches turned to the audio bandwidth extension. Several efficient coding methods for the high frequency (HF) components of audio were proposed, such as PlusV [25] and SBR. Based on the spectral harmonic redundancy, the essential concept of these bandwidth extension methods is to reconstruct the HF components by the replicated low frequency (LF) components or white noise with additional tonality control mechanisms. Since only a small amount of side information is required for the HF reconstruction, the combination of the bandwidth extension modules with the conventional coders can provide the transparent quality at very low bit rate. For example, MPEG-4 High-Efficiency AAC (HE-AAC), which combines SBR with AAC, can generally achieve the comparable quality at 48K bps (bit per second) when compared with AAC at 96K bps. Later, the channel reduction became another dimension for increasing coding efficiency further. The spatial audio coding, such as Binaural Cue Coding (BCC) and Parametric Stereo (PS) coding, can reconstruct a binaural signal from a down-mix monaural signal by means of spatial parameters for recovering stereo sound images. In particular, PS has been merged into HE-AAC as HE-AAC version 2 [10].

## 1.2. Compression Artifacts in MPEG Audio

As a typical representation among the related coding methods, in this dissertation, the MPEG audio [23], [24], including MP3, AAC, SBR and PS, are taken into consideration to explore the compression artifacts from the traditional and novel coding methods. We model the audible artifacts from new coding methods through the time-frequency diagrams, consider the artifact-susceptible music types, analyze the critical encoder modules leading to the artifacts, and provide empirical verifications for the artifacts. We first consider the two common zero-quantization artifacts in frequency-domain audio coders, the "band-limited"

and "birdie" artifacts [18], [35]. Under bit rate constraint, most audio coders discard the HF part of audio to preserve the quality of the LF part but decrease the brightness of audio. Another artifact due to insufficient bits is the birdie artifact that comes from a zero band where all frequency lines are zero-quantized. We propose an audio patch method for reducing the two artifacts. On the other hand, we concern the numerical distortion of the type-IV DCT (DCT-IV) that is the fundamental module in the efficient computation of MDCT. Various composite lengths have been used in several audio applications such as the 12/36-point MDCT in MP3. In the literature, there exist four algorithms for computing DCT-IV of composite lengths based on the fast algorithms for DCT-II/DCT-III computation [26]. However, these methods involve either serial computations or reciprocal cosine coefficients which result in large dynamic ranges. In other words, such parallel implementations inherently introduce large numerical distortion due to finite precision. We present a fast radix-$q$ algorithm for the DCT-IV computation with merits in parallelism, numerical stability and computational complexity.

We next consider the Temporal Noise Shaping (TNS) module [27]-[30] in AAC. TNS, which is a linear predictive coding method in the frequency domain, is one of the effective methods for handling the pre-echo artifact [18], [19]. Although Herre and Johnston have explained the principle of the discrete cosine transform (DCT)-domain TNS through the duality between the squared temporal Hilbert envelope and the power spectrum for continuous-time signals, there is no exact formulation for the DCT-domain TNS for finite discrete sequences. Based on the autoregressive (AR) modeling formulation with discrete trigonometric transforms (DTTs), we establish the compact forms for the DTT-domain TNS in a unified way for DCTs and DSTs (discrete sine transforms). Then we concern the artifacts of TNS due to the time-domain aliasing property of MDCT (modified DCT) [74], [75] and propose an artifact reduction method.

Subsequently, we consider the artifacts in the two major modules, SBR and PS, in

HE-AAC version 2. To approximate the original spectral harmonics and envelopes, SBR allows adaptive time-frequency resolutions and different envelop adjustment modes. For this new kind of audio coding, we explore six new artifacts that are quite different from the traditional coding distortions. On the other hand, in SBR, the second-order linear prediction is applied to LF subbands to clip the undesired tonal components and smooth the associated spectra for the replication to HF bands. Such a process is referred to as the whitening filtering. To avoid the alias artifact from spectral adjustment, SBR adopts a complex-valued filterbank instead of a real-valued filterbank. We demonstrate that the linear prediction defined in the SBR standard results in predictive bias. A new whitening filter is proposed to eliminate the predictive bias. Finally, for PS, we consider the crosstalk artifacts due to the down-mix processing. According to different down-mix approaches, we classify the loss of stereo image and concern the spectral modulation effect due to the varying down-mix coefficients.

## 1.3. Organization

This dissertation is organized as follows. Chapter 2 considers the two zero-quantization artifacts, "band-limited" and "birdie" artifacts, and develops a fast radix-$q$ algorithm of DCT-IV for handling the tradeoff of parallelism and numerical distortion. Chapter 3 derives the theoretic fundamental of TNS, considers the artifacts of TNS, and proposes the related artifacts reduction method. In Chapter 4 and Chapter 5, the artifacts of SBR and PS are concerned, respectively. Chapter 6 concludes this dissertation.

# CHAPTER 2
# COMMON ARTIFACTS BY ZERO-QUANTIZATION AND NUMERICAL DISTORTION

In this chapter, we first concern two common zero-quantization artifacts which lead to the loss of high or middle frequency. On the other hand, to achieve the best system efficiency, the sequence lengths other than a power of two have been used in many audio applications. We develop a fast odd radix algorithm for computing DCT-IV of composite lengths with low numerical distortion artifacts and high parallelism.

## 2.1. Band-Limited and Birdie Artifacts

The two most common compression artifacts from audio coding are the "band-limited" and the "birdie" artifacts [18], [35]. The bit-rate constraint inflicts the artifacts on critical audio segments showing up in spectrum as the "spectral valley" or the "spectral clipping". Spectral valley, as shown in Figure 2.1 (b), means a band in which all frequency lines are zero-quantized. Spectral valley phenomenon is mainly due to unsuitable bit-allocation policies or excessive masking energy measured from the psychoacoustic model in audio encoders. Spectral valleys may appear and disappear successively due to unsteady demand for bits between frames. This causes the changes in timbre and the energy variation in spectrum and results in the birdie effect to which the human hearing is very sensitive.

Spectral clipping, as shown in Figure 2.2 (b), results from cutting the high frequency (HF) content during audio compression. The loss of HF may lead to "muffled" audio. Because of the limited bit rate, most audio coding approaches save the bits required for HF spectra and put all available bits to low frequency (LF) spectra, which are more relevant for the human hearing.

(a)



(b)



(c)
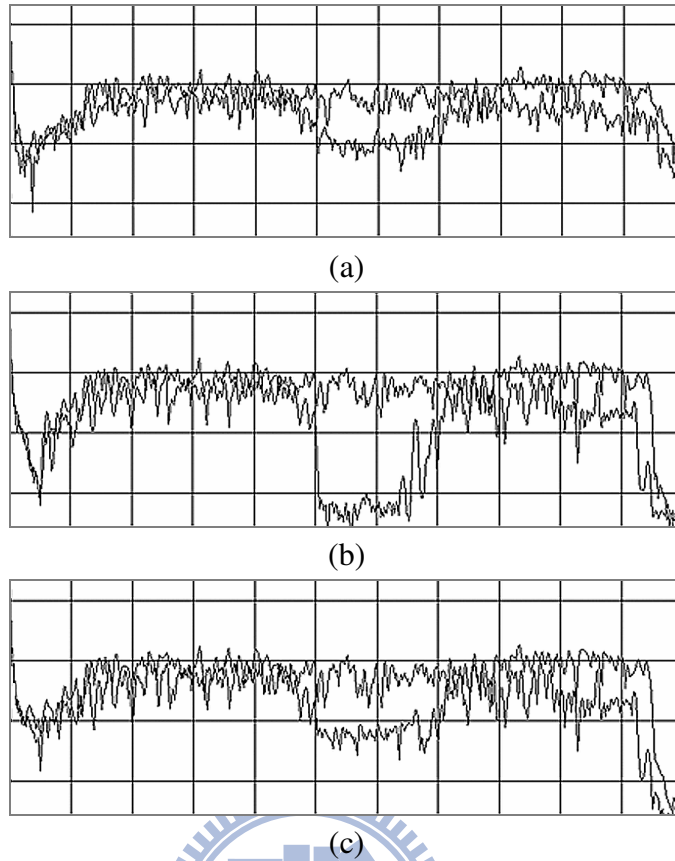
Figure 2.1. Spectral valley phenomenon and its concealment: (a) original audio signal spectrum; (b) compressed spectrum with two zero bands in low and middle frequency parts; (c) compressed spectrum enhanced by ZBD.

For instance, the bandwidth in MP3 is generally restricted to 16 kHz due to the protocol constraint, and the speech signal can even be limited to 7–8 kHz with good clarity. However, the HF loss significantly degrades the signal with rich HF components. Handling the two artifacts is a tradeoff for the encoder design owing to the limited available bits. A coding method that aggressively retains HF contents brings more risk to spectral valleys to which the human hearing is more sensitive among the two artifacts. Therefore, the HF content is generally cut to reduce the risk of spectral valleys.

Many attempts [36]-[44] have been made to reduce the two artifacts. For instance, our work [36]-[38] presented an audio patch method comprising two schemes, Zero Band Dithering (ZBD) and High Frequency Reconstruction (HFR), to handle the artifacts in decoder.

Figure 2.1 (c) and Figure 2.2 (c) illustrate the enhanced spectra resulting from the patch method. The method can be included in frequency-domain decoders, such as MP3, AAC and HE-AAC, to conceal the artifacts without prior information. The ZBD module can be applied to frequency lines after dequantization and dithers zero lines with random noises. On the other hand, the HFR module can be applied to the transform coefficients before the inverse transform or the QMF subbands before the synthesis filterbank and regenerate the clipped HF spectrum by linear extrapolation. For instance, Figure 2.3 and Figure 2.4 illustrate the incorporation of the two models into AAC and HE-AAC decoders, respectively. Figure 2.5 illustrates the application of the audio patch method to a HE-AAC audio. As can be seen, the ZBD method patches the LF part of the HE-AAC audio spectrum is dupliated to middle HF part; moreover, the HFR method extends the bandwidth.



(a)



(b)



(c)
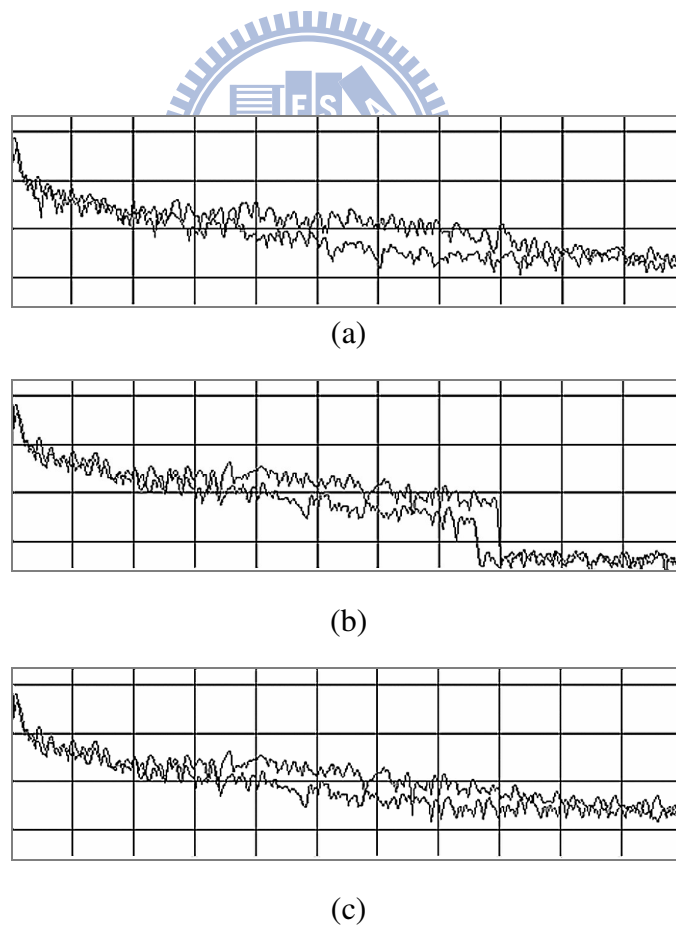
Figure 2.2. Spectral clipping phenomenon and its concealment: (a) original audio signal spectrum; (b) compressed spectrum with narrow bandwidth; (c) compressed spectrum with bandwidth extension by HFR.
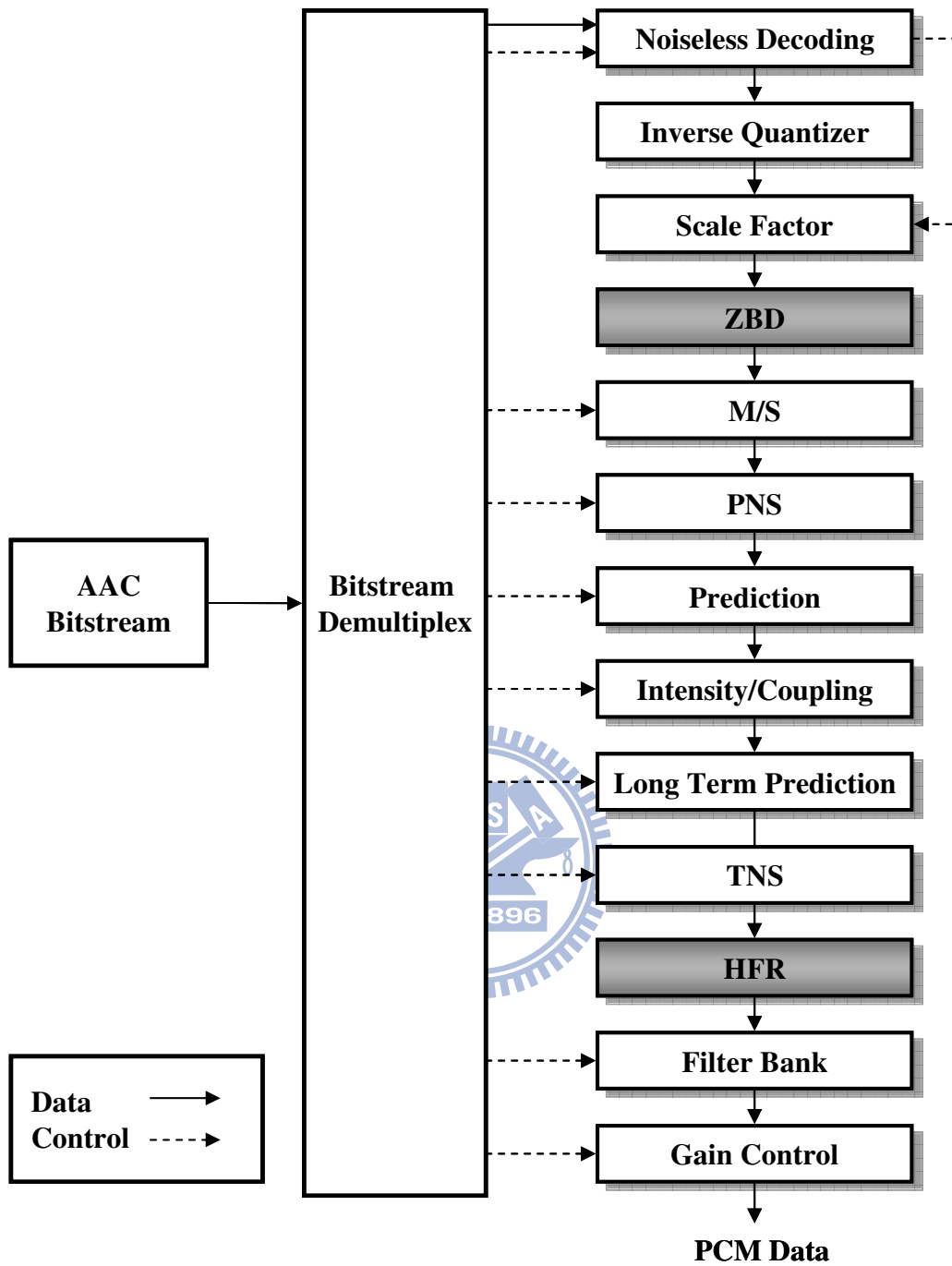
Figure 2.3. The incorporation of ZBD and HFR into AAC decoder.
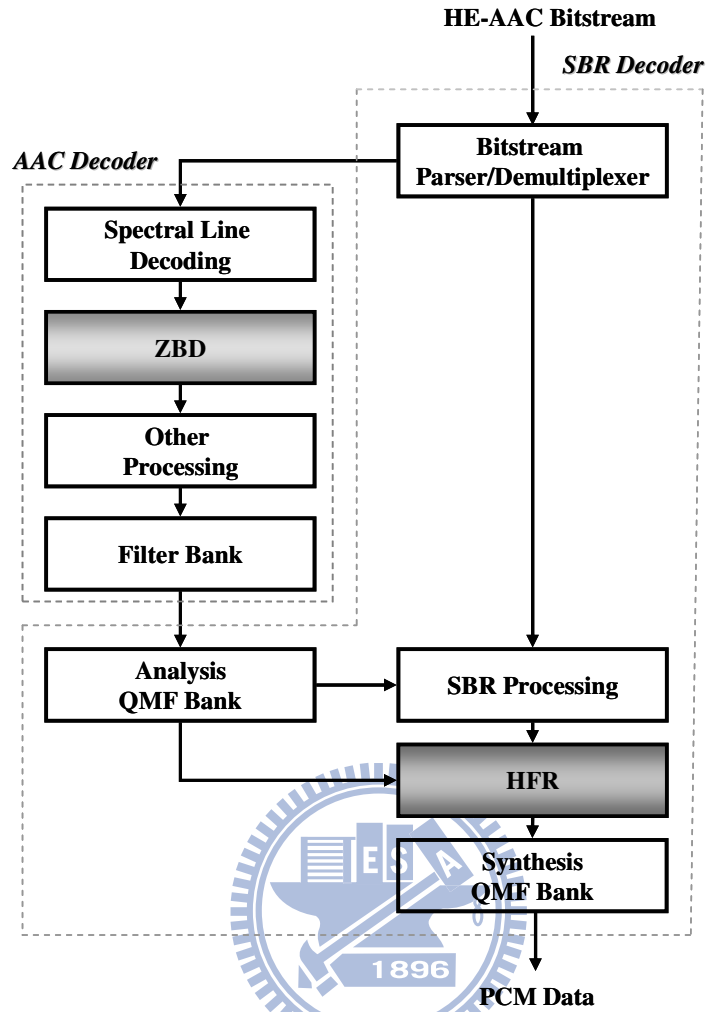
Figure 2.4. The incorporation of ZBD and HFR into HE-AAC decoder.



(a)



(b)
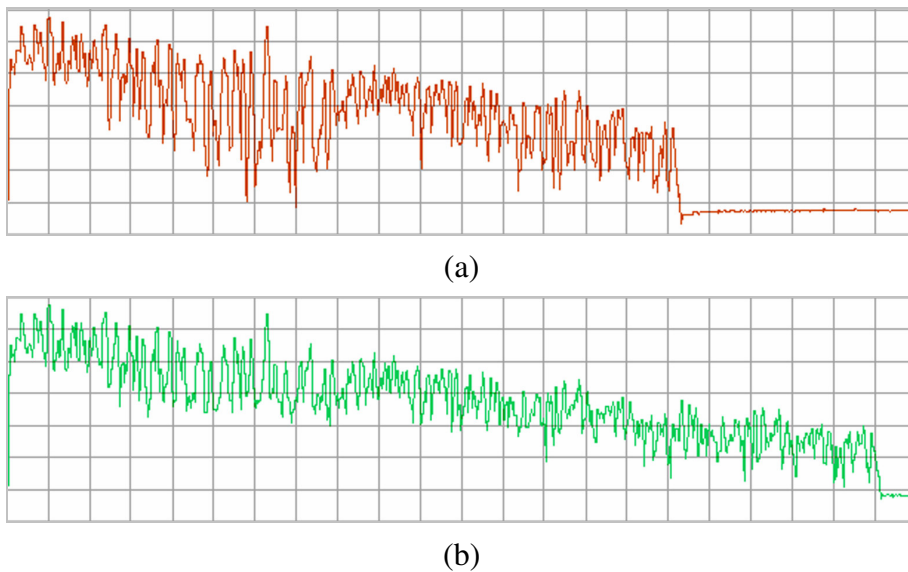
Figure 2.5. Enhancement of HE-AAC audio by the audio patch method: (a) the HE-AAC audio spectrum; (b) the enhanced spectrum.

# 2.2. Fast Radix-*q* Algorithm for DCT-IV with Low Numerical Distortion Artifact and High Parallelism

The DCT-IV as defined in (1) is the fundamental module in the efficient computation of the lapped orthogonal transforms and cosine modulated filter banks known as MDCT.

$$y_k = \sum_{n=0}^{N-1} x_n \cos[(n+\tfrac{1}{2})(k+\tfrac{1}{2})/N], \quad k = 0, 1, 2,\ldots, N-1. \tag{1}$$

The sequence length of a power of two is most popular due to the computational efficiency and structure simplicity of the existing radix-2 algorithms. However, various sequence lengths other than a power of two have been used to achieve the best efficiency in audio coding and processing, such as the 12/36-point MDCT in MP3 audio coding.

In the literature, there exist various fast radix-2 algorithms for computing DCT-II and DCT-III [45], [46]. The fast radix-*q* algorithms for the DCT-II/DCT-III computation have been also developed and extended to the fast mixed-radix algorithms for composite lengths [47], [48]. On the computation of DCT-IV, we can consider the four existing approaches, which convert DCT-IV into DCT-II or DCT-III [26]. The four fast algorithms are represented in matrix form as

$$C_N^{IV} = LC_N^{II}D = D^{-1}C_N^{III}D_1L^{-1} = D^T C_N^{III}L^T = (L^{-1})^T D_1^T C_N^{II}(D^{-1})^T, \tag{2}$$

where the DCT-II/ DCT-III/ DCT-IV matrices are respectively defined as

$$[C_{II}^{IV}]_{k,n} = \cos[(n+1/2)k/N],$$

$$[C_{III}^{IV}]_{k,n} = \cos[n(k+1/2)/N],$$

$$[C_{IV}^{IV}]_{k,n} = \cos[(n+1/2)(k+1/2)/N],$$

for *n*, *k* = 0, 1, 2, …, *N* − 1; diagonal matrices $D$ and $D_1$ of order *N* are defined by *diag*{2cos(π(*i*+1/2)/2*N*) | *i* = 0, 1,…, *N* − 1} and *diag*{1/2, 1, 1,…, 1} respectively; lower

triangular matrix $L$ is defined by the serial computation: $[\,y_0, y_1,\dots, y_{N-1}\,]^T = L[\,x_0, x_1,\dots,x_{N-1}\,]^T$ $= [\,x_0/2,\; x_1 - y_0, x_2 - y_1,\dots,\; x_{N-1}\; -\; y_{N-2}\,]^T$. However, as depicted in Figure 2.6, the four methods indicated in (2) involve either serial computations or reciprocal cosine coefficients which result in large numerical distortion artifact due to large dynamic ranges. In other words, these DCT-II/DCT-III-based fast algorithms have a tradeoff between numerical distortion and parallelism. In this section, we propose a fast radix-$q$ algorithm for the DCT-IV computation with merits in parallelism, numerical stability and computational complexity, where $q$ is an odd positive integer. The proposed radix-$q$ algorithm can be extended to the fast mixed-radix DCT-II/DCT-IV computation for composite lengths.
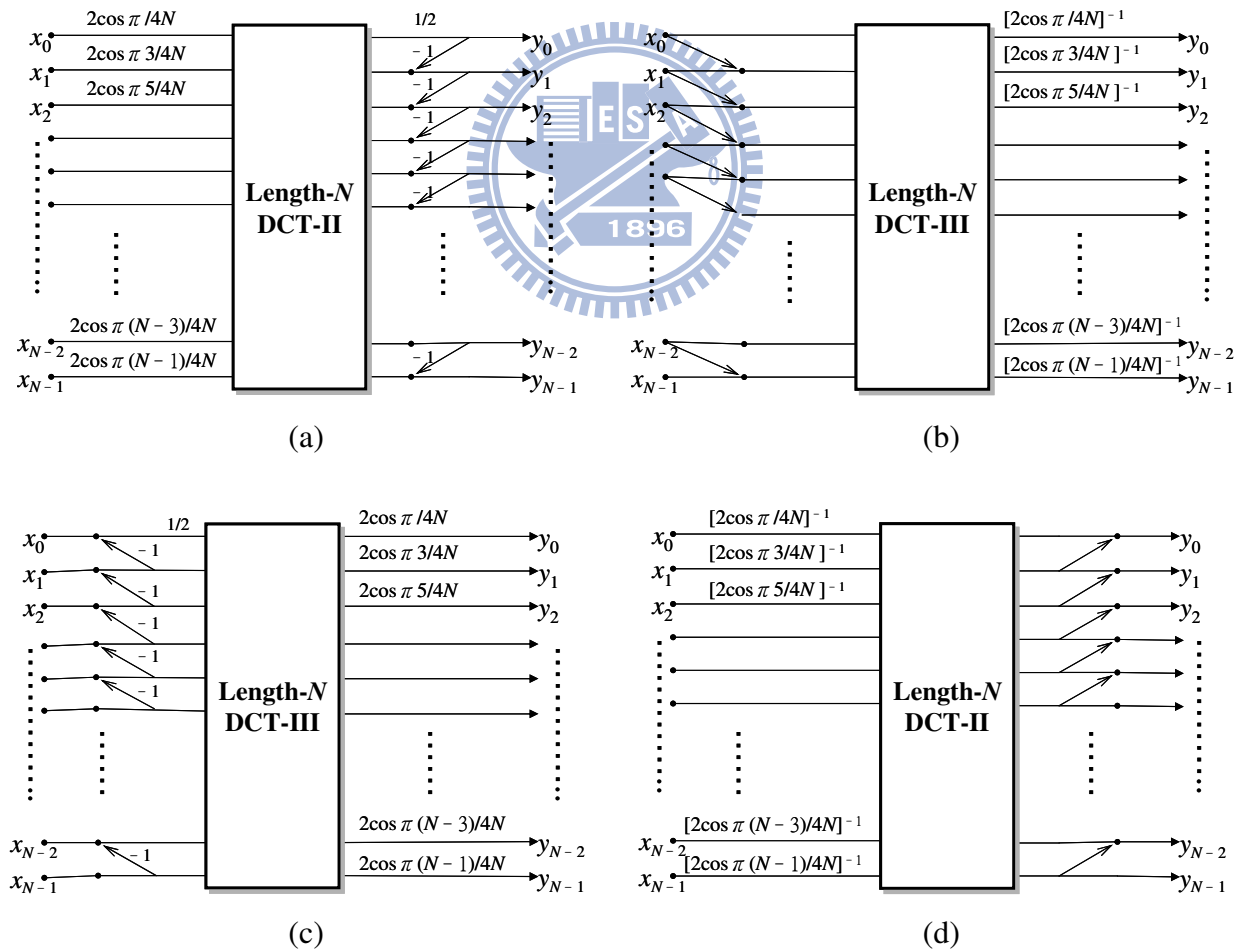


Figure 2.6. Signal flow graphs of the four DCT-IV algorithms indicated in (2).

### 2.2.1. Fast Radix-*q* Algorithm for DCT-IV Computation

We begin with the scaled DCT-IV (SDCT-IV) defined as

$$Y_k = \sqrt{2} \cdot \sum_{n=0}^{N-1} x_n \cos \Phi_{n,k}^N, \ k = 0, 1, \ldots, N-1, \tag{3}$$

where $\Phi_{n,k}^N$ denotes $\pi(n + 1/2)(k + 1/2)/N$. For the case of length 1, DCT-IV requires one multiplication, but SDCT-IV requires no multiplication. Let the sequence length $N$ be a multiple of $q$ that is an odd positive integer. Equation (3) can be partitioned into $q$ superpositions by grouping the terms with the same indices under the module $q$ as

$$Y_k = \sqrt{2} \sum_{n=0}^{\frac{N}{q}-1} x_{qn+\frac{q-1}{2}} \cos \Phi_{n,k}^{\frac{N}{q}} + \sqrt{2} \sum_{m=0}^{\frac{q-3}{2}} \sum_{n=0}^{\frac{N}{q}-1} x_{qn+m} \cos \Phi_{qn+m,k}^N + \sqrt{2} \sum_{m=0}^{\frac{q-3}{2}} \sum_{n=0}^{\frac{N}{q}-1} x_{qn+q-1-m} \cos \Phi_{qn+q-1-m,k}^N. \tag{4}$$

Combining the second and the third terms of (4) and using the trigonometric identity $\cos(a+b) = \cos(a)\cos(b) - \sin(a)\sin(b)$, we obtain

$$Y_k = A_k + \sum_{m=0}^{\frac{q-3}{2}} \left( C_k^m \cos \Theta_{m,k}^N + S_k^m \sin \Theta_{m,k}^N \right), \tag{5}$$

where

$$\Theta_{m,k}^N = \frac{\pi}{N}\left(\frac{q-1}{2} - m\right)\left(k + \frac{1}{2}\right), \tag{6}$$

$$A_k = \sqrt{2} \sum_{n=0}^{\frac{N}{q}-1} x_{qn+\frac{q-1}{2}} \cos \Phi_{n,k}^{\frac{N}{q}}, \tag{7}$$

$$C_k^m = \sqrt{2} \sum_{n=0}^{\frac{N}{q}-1} (x_{qn+m} + x_{qn+q-1-m}) \cos \Phi_{n,k}^{\frac{N}{q}}, \tag{8}$$

$$S_k^m = \sqrt{2} \sum_{n=0}^{\frac{N}{q}-1} (x_{qn+m} - x_{qn+q-1-m}) \sin \Phi_{n,k}^{\frac{N}{q}}, \tag{9}$$

or

$$S_{\frac{N}{q}-1-k}^m = \sqrt{2} \sum_{n=0}^{\frac{N}{q}-1} (-1)^n (x_{qn+m} - x_{qn+q-1-m}) \cos \Phi_{n,k}^{\frac{N}{q}}, \tag{10}$$

for $m = 0, 1, \ldots, (q-3)/2$, $k = 0, 1, \ldots, N-1$.

Equation (5) consists of $q$ length-$N/q$ SDCTs-IV defined by (7)-(10). Further, it can be shown

that for any integer $p$,

$$A_{\frac{2pN}{q}+k} = A_{\frac{2pN}{q}-1-k} = (-1)^p A_k, \tag{11}$$

$$C_{\frac{2pN}{q}+k}^m = C_{\frac{2pN}{q}-1-k}^m = (-1)^p C_k^m, \tag{12}$$

$$S_{\frac{2pN}{q}+k}^m = -S_{\frac{2pN}{q}-1-k}^m = (-1)^p S_k^m. \tag{13}$$

In order to save multiplications, by using properties (11)-(13), we form the two sequences $U_k^p$

and $V_k^p$ that are 1/2 of the sum and difference of $Y_{\frac{2pN}{q}+k}$ and $Y_{\frac{2pN}{q}-1-k}$ as follows:

$$U_k^p = (-1)^p A_k + \sum_{m=0}^{\frac{q-3}{2}} \left( C_k^m \cos\Theta_{m,k}^N + S_k^m \sin\Theta_{m,k}^N \right) \cos\frac{p(2m+1)\pi}{q}, \tag{14}$$

for $p = 0, 1,\ldots, (q-1)/2, k = 0, 1,\ldots, N/q - 1$;

$$V_k^p = \sum_{m=0}^{\frac{q-3}{2}} \left( C_k^m \sin\Theta_{m,k}^N - S_k^m \cos\Theta_{m,k}^N \right) \cdot \sin\frac{p(2m+1)\pi}{q}, \tag{15}$$

for $p = 1, 2,\ldots, (q-1)/2, k = 0, 1,\ldots, N/q - 1$.

Similar to the strategy utilized in [47], for each $k$ and each $p$, $(q-1)/2$ multiplications can be

saved by moving the cosine coefficients outside the brackets in (14) and (15), respectively.

However, the range of the angles $\Theta_{m,k}^N$ is from 0 to $\pi/2$, and thus the dynamic range of tangent

values is large. To control numerical stability, (14) and (15) are rewritten as

$$U_k^p = (-1)^p A_k + \sum_{m=0}^{\frac{q-3}{2}} T_k^m \cdot (\Lambda_k^m \cos\frac{p(2m+1)\pi}{q}), \tag{16}$$

for $p = 0, 1,\ldots, (q-1)/2, k = 0, 1,\ldots, N/q - 1$;

$$V_k^p = \sum_{m=0}^{\frac{q-3}{2}} H_k^m \cdot (\Lambda_k^m \sin\frac{p(2m+1)\pi}{q}), \tag{17}$$

for $p = 1, 2,\ldots, (q-1)/2, k = 0, 1,\ldots, N/q - 1$,

where

$$(\Lambda_k^m, T_k^m, H_k^m) = \begin{cases} (\cos\Theta_{m,k}^N, C_k^m + S_k^m \tan\Theta_{m,k}^N, C_k^m \tan\Theta_{m,k}^N - S_k^m) & if\ \Theta_{m,k}^N \le \frac{\pi}{4} \\ \\ (\sin\Theta_{m,k}^N, C_k^m \cot\Theta_{m,k}^N + S_k^m, C_k^m - S_k^m \cot\Theta_{m,k}^N) & if\ \Theta_{m,k}^N > \frac{\pi}{4} \end{cases}. \tag{18}$$
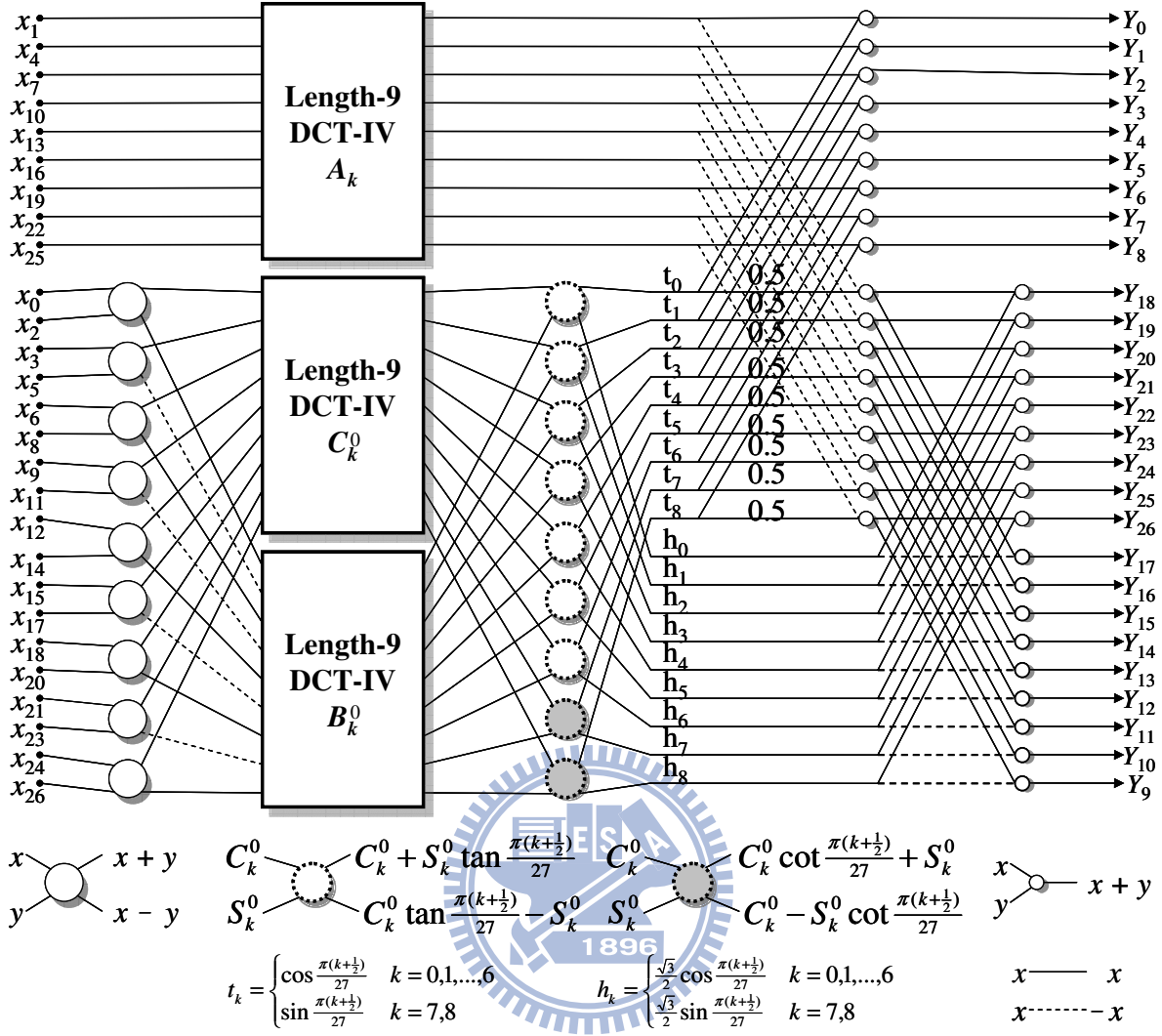
Figure 2.7. Signal flow graphs of length-27 SDCT-IV.

The figure shows signal flow graphs with blocks labeled:
- Length-9 DCT-IV $A_k$
- Length-9 DCT-IV $C_k^0$
- Length-9 DCT-IV $B_k^0$

Inputs $x_1, x_4, x_7, x_{10}, x_{13}, x_{16}, x_{19}, x_{22}, x_{25}$ to the first block; $x_0, x_2, x_3, x_5, x_6, x_8, x_9, x_{11}, x_{12}, x_{14}, x_{15}, x_{17}, x_{18}, x_{20}, x_{21}, x_{23}, x_{24}, x_{26}$ to the lower blocks. Intermediate nodes $t_0 \ldots t_8$ (each with weight 0.5) and $h_0 \ldots h_8$. Outputs $Y_0 \ldots Y_{26}$.

Butterfly/node definitions:

$$\begin{array}{l} x \\ y \end{array} \longrightarrow \begin{array}{l} x+y \\ x-y \end{array}$$

$$C_k^0 \longrightarrow C_k^0 + S_k^0 \tan\frac{\pi(k+\frac{1}{2})}{27}$$
$$S_k^0 \longrightarrow C_k^0 \tan\frac{\pi(k+\frac{1}{2})}{27} - S_k^0$$

$$C_k^0 \longrightarrow C_k^0 \cot\frac{\pi(k+\frac{1}{2})}{27} + S_k^0$$
$$S_k^0 \longrightarrow C_k^0 - S_k^0 \cot\frac{\pi(k+\frac{1}{2})}{27}$$

$$\begin{array}{l} x \\ y \end{array} \longrightarrow x+y$$

$$t_k = \begin{cases} \cos\frac{\pi(k+\frac{1}{2})}{27} & k=0,1,\ldots,6 \\ \sin\frac{\pi(k+\frac{1}{2})}{27} & k=7,8 \end{cases} \qquad h_k = \begin{cases} \frac{\sqrt{3}}{2}\cos\frac{\pi(k+\frac{1}{2})}{27} & k=0,1,\ldots,6 \\ \frac{\sqrt{3}}{2}\sin\frac{\pi(k+\frac{1}{2})}{27} & k=7,8 \end{cases} \qquad x \longrightarrow x \qquad x \cdots\cdots -x$$

In (18), the dynamic range of the tangent and cotangent values is controlled within the interval [0, 1]. The final SDCT-IV outputs are obtained from

$$Y_k = U_k^0, \quad \text{for } k = 0, 1,\ldots, N/q -1; \tag{19}$$

$$Y_{\frac{2pN}{q}+k} = U_k^p + V_k^p \quad \text{and} \quad Y_{\frac{2pN}{q}-1-k} = U_k^p - V_k^p, \tag{20}$$

$$\text{for } p = 1, 2,\ldots, (q - 1)/2, \ k = 0, 1,\ldots, N/q - 1.$$

Equation (19) is obtained from the symmetry around $k = -1/2$ of DCT-IV output. For a length-$q^\lambda$ SDCT-IV, the decomposition must be repeated until the lengths of subsequences are one. To obtain the output of DCT-IV or IDCT-IV, $N$ multiplications are required for the scaling

operations. Absorbing the scaling factors into (16) and (17) yields

$$U_k'^p = (-1)^p \delta \cdot A_k + \sum_{m=0}^{\frac{q-3}{2}} T_k^m \cdot \Lambda_k^m \cdot \delta \cdot \cos \frac{p(2m+1)\pi}{q} ,$$

(21)

for $p = 0, 1,\ldots, (q - 1)/2$, $k = 0, 1,\ldots, N/q - 1$;

$$V_k'^p = \sum_{m=0}^{\frac{q-3}{2}} H_k^m \cdot \Lambda_k^m \cdot \delta \cdot \sin \frac{p(2m+1)\pi}{q} ,$$

(22)

for $p = 1, 2,\ldots, (q - 1)/2$, $k = 0, 1,\ldots, N/q - 1$,

where $\delta$ is $1/\sqrt{2}$ and $\sqrt{2}/N$ for DCT-IV and IDCT-IV, respectively. The number of scaling operations can be reduced from $N$ to $N/q$. To summarize, the proposed algorithm comprises (7)-(10) and (16)-(22). Figure 2.7 shows the signal flow graph for a length-27 SDCT-IV after the first stage decomposition.

### 2.2.1.1 Parallelism and Numerical Stability

Each DCT-II-based algorithm for DCT-IV computation illustrated in (2) involves either serial computations or reciprocal cosine coefficients. However, the proposed radix-$q$ algorithm avoids reciprocal cosine coefficients, especially due to the mechanism in (18), and thus has good numerical stability. On the other hand, if the latency of hardware implementation is considered, the length of the critical path of the DCT-II-based algorithm involving the serial computation is $N$ because of the recursive computation for matrix $L$. The unit of the length is one multiplication or addition operation. For the proposed radix-$q$ algorithm, the length of the critical path is $ceiling\{log_2[(q - 3)/2]\}$ because of the summation in (21). This result shows the critical path of the proposed radix-$q$ algorithm is significantly shorter than that of the DCT-II-based algorithm involving the serial computation.

15

## 2.2.1.2 Computational Complexity

The recursive forms of the cost functions for the proposed algorithm are shown in Appendix A. Let $N = q^\lambda$, the non-recursive forms are given by

$$M_{IV}(N) = (q - 1)(q + 2)/(2q) \cdot Nlog_q N + N/q, \qquad (23)$$

$$A_{IV}(N) = (q - 1)(q + 5)/(2q) \cdot Nlog_q N. \qquad (24)$$

In general, a lower computational cost than that induced from (23) and (24) can be achieved by rearranging the operation factors. Furthermore, the optimization of the initial case for small length-$q$ SDCT-IV can reduce the overall complexity. In Appendix A.2-A.4, we derive and tune the fast algorithms for radix-3, radix-5, and radix-9 DCT-IV computation.

The arithmetic complexity of the DCT-II-based algorithm indicated in (2) is given by

$$M_{IV}(N) = M_{II}(N) + N, \qquad (25)$$

$$A_{IV}(N) = A_{II}(N) + N - 1. \qquad (26)$$

Table 2.1 compares the arithmetic complexity of the proposed DCT-IV algorithm and the DCT-II-based algorithm, where the fast algorithm [47] is adopted for computing DCT-II of length $N = q^\lambda$. The comparison shows that the proposed algorithm not only is free from the serial computation and numerical instability but also achieves a lower arithmetic complexity than the DCT-II-based algorithm for $q = 3$ and 9.

Table 2.1. Arithmetic Complexity Comparison for DCT-IV of $N = q^\lambda$

| | The proposed algorithm | | DCT-II based algorithm | |
|---|---|---|---|---|
| $q$ | $M_{IV}(N)$, $N > q$ | $M_{IV}(q)$ | $M_{IV}(N)$, $N > q$ | $M_{IV}(q)$ |
| 3 | $4/3 \cdot N \, log_3 N - 7N/6 + 5/2$ | 3 | $4/3 \cdot N \, log_3 N - 17N/18 + 3/2$ | 4 |
| 5 | $11/5 \cdot N \, log_5 N$ | 11 | $11/5 \cdot N \, log_5 N - 7N/10 + 3/2$ | 9 |
| 7 | $27/7 \cdot N \, log_7 N + N/7$ | 28 | $27/7 \cdot N \, log_7 N - N/2 + 3/2$ | 25 |
| 9 | $20/9 \cdot N \, log_9 N - 177N/216 + 11/8$ | 16 | $23/9 \cdot N \, log_9 N - 7N/8 + 15/8$ | 17 |
| $q$ | $A_{IV}(N)$, $N > q$ | $A_{IV}(q)$ | $A_{IV}(N)$, $N > q$ | $A_{IV}(q)$ |
| 3 | $8/3 \cdot N \, log_3 N - N + 1$ | 6 | $8/3 \cdot N \, log_3 N - 7N/9 + 1$ | 6 |
| 5 | $21/5 \cdot N \, log_5 N$ | 21 | $21/5 \cdot N \, log_5 N - N + 1$ | 17 |
| 7 | $36/7 \cdot N \, log_7 N$ | 36 | $36/7 \cdot N \, log_7 N - N + 1$ | 30 |
| 9 | $53/9 \cdot N \, log_9 N \; - 103N/72 - 1/8$ | 40 | $50/9 \cdot N \, log_9 N - N + 1$ | 42 |

### 2.2.2. Fast Mixed-Radix DCT-II /DCT-IV Algorithm

For composite lengths, i.e., $N = 2^{\lambda_0} \cdot q_1^{\lambda_1} \cdot q_2^{\lambda_2} \cdot \ldots \cdot q_n^{\lambda_n}$, for odd integers $0 < q_1 < q_2 < \ldots < q_n$ and any non-negative integers $\lambda_0, \lambda_1, \ldots, \lambda_n$, the proposed radix-$q$ algorithm can be flexibly combined with the existing fast DCT-II/DCT-IV algorithms for composite lengths. The illustrated radix-2 DCT-II/DCT-IV algorithm consisting of Wang's [49, eq. (50)] and Britanak's [50, eq. (16)] algorithms is described in Appendix A.5. As depicted in Figure 2.8 and Figure 2.9, the radix-2 DCT-II/DCT-IV algorithm decomposes a length-$N$ DCT-II into a length-$N/2$ DCT-II and a length-$N/2$ DCT-IV and decomposes a DCT-IV into two length-$N/2$ DCTs-II without involving serial computations and reciprocal cosine coefficients. The proposed radix-$q$ DCT-IV algorithm can be combined with the radix-2 DCT-II/DCT-IV algorithm and the radix-$q$ DCT-II algorithm [47] to constitute a mixed-radix algorithm for DCT-II/DCT-IV computation to achieve the demands in parallelism and numerical stability. Furthermore, as shown in Appendix A.6, the mixed-radix algorithm obtains the merit in computational complexity.
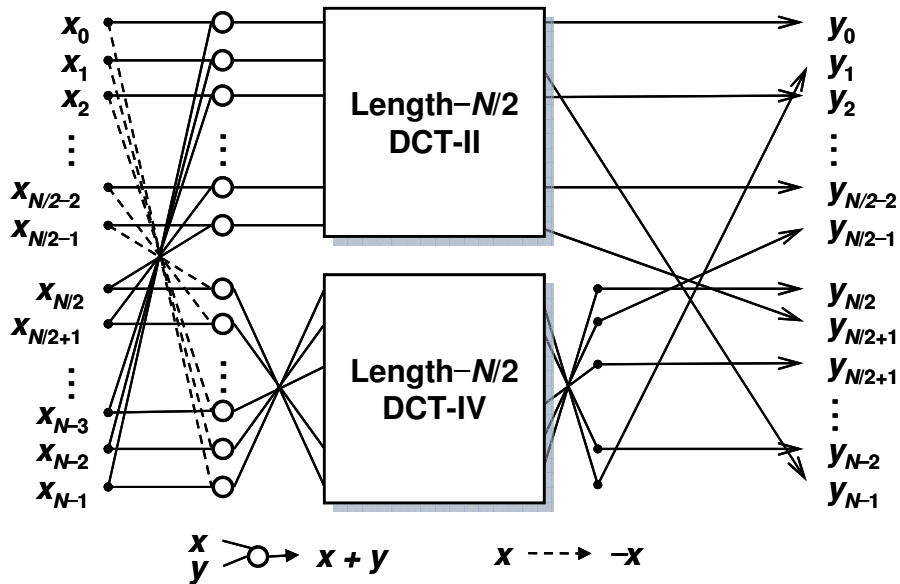


Figure 2.8. Signal flow graph of the length-$N$ DCT-II decomposition.
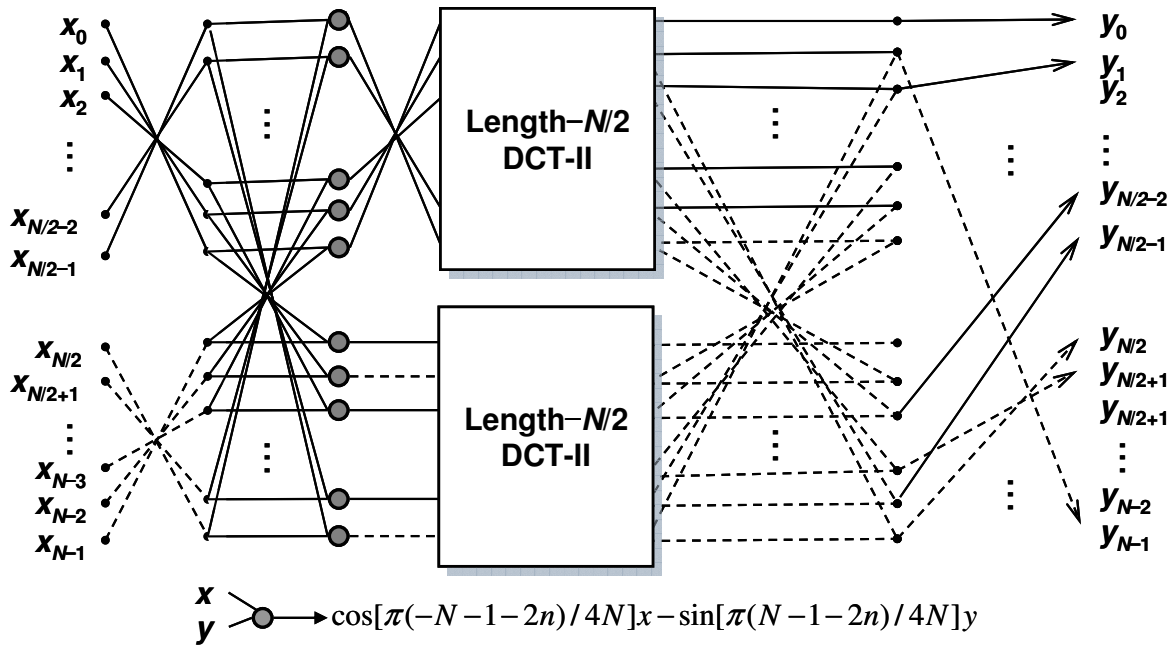
Figure 2.9. Signal flow graph of the length-*N* DCT-IV decomposition.

## 2.3. Concluding Remarks

In this chapter, we have considered the two common zero-quantization artifacts, "band-limited" and "birdie" artifacts. An audio patch method comprising two schemes, ZBD and HFR, has been proposed to reduce the two artifacts. The patch method can be incorporated into transform or subband based audio decoders, such as MP3, AAC and HE-AAC. On the other hand, for the computation of the cosine modulated filterbank, we have proposed a fast radix-*q* DCT-IV algorithm to handle the conflict between parallelism and numerical distortion artifact in the existing algorithms. The radix-*q* algorithm can be extended into a mixed-radix algorithm for the DCT-IV computation of composition lengths with the merits in parallelism, numerical stability and computational complexity.

# CHAPTER 3
# ARTIFACTS IN
# TEMPORAL NOISE SHAPING

The TNS method [27]-[30] has been utilized in MPEG-2/4 AAC for attenuating the quantization noise preceding the attack signal known as the pre-echo artifact [18], [19]. As illustrated in Figure 3.1, the quantization noise spreads throughout the entire signal block in the time domain. The TNS module can shape and control the spread of quantization noise to improve audio quality.

Since the TNS in AAC is applied to the MDCT coefficients that are highly related to the even DCT-IV, based on the theory of the spectral AR modeling in the DTT domain, we establish the compact form of the TNS in the DTT domain and explain the "time-domain aliasing noise" [30], which has an unusual noise around the attack segment. We also concern the degradation of the artifact with the TNS filter orders. Finally, we compare the TNS by the Hilbert and power envelope methods.
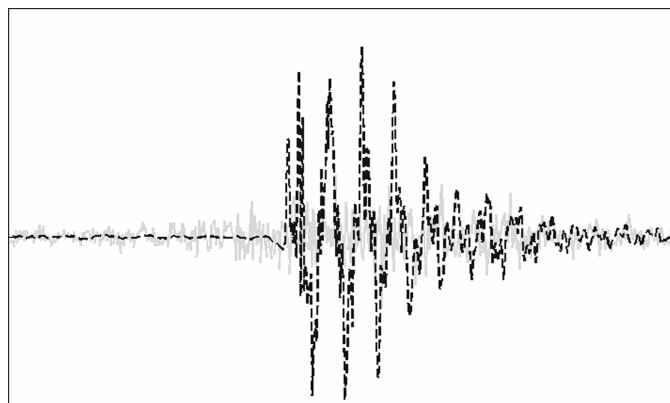


Figure 3.1. Pre-echo artifact (dashed line: original waveform; solid line: quantization noise).

# 3.1. TNS Formulation in DTT Domain

TNS aims to shape the temporal envelope of the quantization noise by incorporating an open-loop predictive coding [31] across frequency lines in audio encoders/decoders. In terms of $z$-transform, the concept of TNS can be explained as follows. As depicted in Figure 3.2, $x(k)$ and $d(k)$ denote the input and the predictive residual signals in the frequency domain in the analysis part, whereas $x_r(k)$ and $d_r(k)$ denote the reconstructed signals related to $x(k)$ and $d(k)$ in the synthesis part. The relation between the reconstruction error $r(k)$, i.e., $x(k) - x_r(k)$, and the quantization noise $q(k)$, i.e., $d(k) - d_r(k)$, is expressed in $z$-transform as

$$R(z) = \frac{Q(z)}{1 - H(z)}, \tag{27}$$

where $R(z)$ and $Q(z)$ are the $z$-transforms of $r(k)$ and $q(k)$. If the magnitude response of the inverse or whitening filter $1/(1-H(z))$ can approximate the temporal envelope of the frequency-domain input signal $x(k)$, the quantization noise $Q(e^{-j\omega})$ (in the time domain) can be amplified or attenuated with the temporal shape. Figure 3.3 illustrates the shaping effect of the TNS applied in the MDCT domain.

In [27]-[30], Herre and Johnston have proposed the TNS predictive filter by exploiting the duality between the squared temporal Hilbert envelope and the power spectrum for continuous-time signals. Since, in the literature, there is no derivation for the finite discrete sequences in the DTT domain, this section derives the compact form for the TNS in the DTT domain through the theory of the AR modeling in the DTT domain.
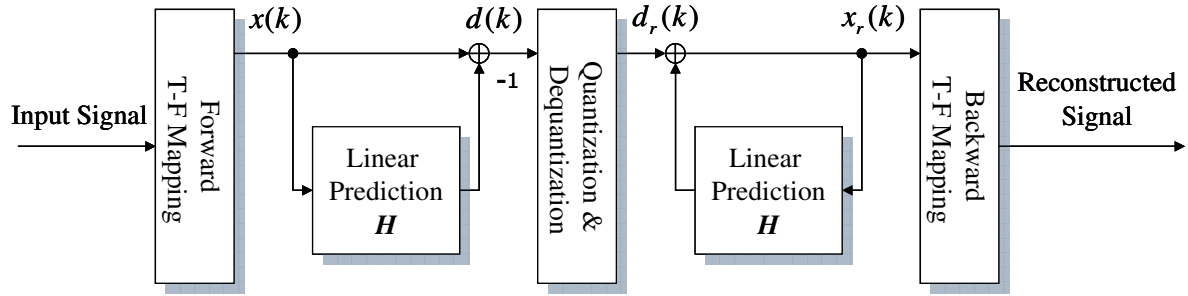
Figure 3.2. Open-loop predictive coding scheme in TNS



(a)



(b)



(c)
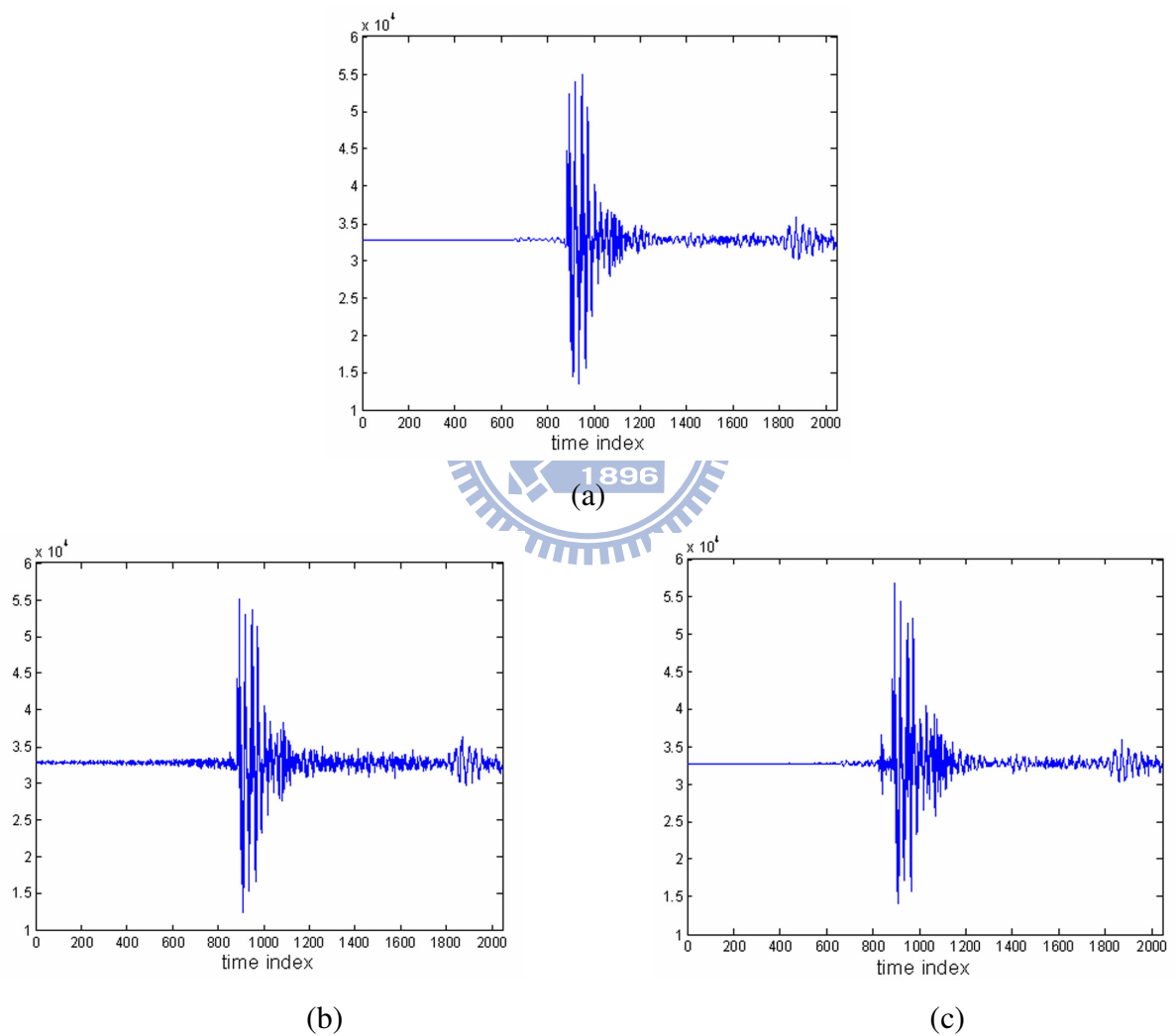
Figure 3.3. TNS effect. (a) original signal in the time domain; (b) decoded signal without TNS; (c) decoded signal with TNS.

### 3.1.1.Autoregressive Modeling in DTT Domain

The AR modeling [53], [64], also known as linear prediction (LP), has received more and more applications in audio coding. The theoretical fundamental for AR modeling of temporal/spectral envelopes with various DTTs has been established in Appendix B. Here, we summarize the critical results related to the TNS formulation.

Through this chapter, we consider all transforms as matrices that left-multiply the input sequence represented as a column vector.

#### 3.1.1.1 Generalized Discrete Fourier Transform

The $N \times N$ generalized DFT (GDFT) [77] matrix is defined by

$$[\boldsymbol{G}_{a,b}]_{k,n} = \exp\left[\frac{-j2\pi(k+a)(n+b)}{N}\right], \text{ for } k, n = 0, 1, \ldots, N-1. \tag{28}$$

Four special forms of the GDFT arise when $a$ and $b$ take on the values 0 or 1/2. They are classified and named as follows [76]:

(i) DFT (Discrete Fourier transform): $a = 0$ and $b = 0$.

(ii) OTDFT (Odd-Time DFT): $a = 0$ and $b = 1/2$.

(iii) OFDFT (Odd-Frequency DFT): $a = 1/2$ and $b = 0$.

(iv) O$^2$DFT (Odd-Time Odd-Frequency DFT): $a = 1/2$ and $b = 1/2$.

The last three transforms can be regarded as the modified versions of the DFT with a 1/2-sample delay in the time domain and/or a 1/2-sample advance in the frequency domain. The inverse GDFT (IGDFT) matrix is the scaled Hermitian transpose of the forward GDFT matrix:

$$\boldsymbol{G}_{a,b}^{-1} = \tfrac{1}{N}\boldsymbol{G}_{a,b}^{H} = \tfrac{1}{N}\boldsymbol{G}_{b,a}^{*}, \tag{29}$$

where superscripts ($H$) and (*) denote the Hermitian transpose and conjugate operations, respectively.

### 3.1.1.2 Convolution-Multiplication Property of GDFT

The circular and skew-circular convolutions of two vectors $\boldsymbol{x}$ and $\boldsymbol{y}$ of length $N$ are defined as

$$(\boldsymbol{x} \; \text{©} \; \boldsymbol{y})_n = \sum_{k=0}^{n} x_k y_{n-k} + \sum_{k=n+1}^{N-1} x_k y_{n-k+N} \text{ , for } n = 0, 1, \ldots, N-1. \tag{30}$$

$$(\boldsymbol{x} \; \text{ⓢ} \; \boldsymbol{y})_n = \sum_{k=0}^{n} x_k y_{n-k} - \sum_{k=n+1}^{N-1} x_k y_{n-k+N} \text{ , for } n = 0, 1, \ldots, N-1. \tag{31}$$

The DFT has the convolution-multiplication property that the inverse transformation after entry-wise multiplication gives the same result as the circular convolution of the original sequences. Vernet [78] and Martucci [76] derived such properties for other GDFTs. We summarize the results in matrix form as follows.

Let $\boldsymbol{u} = \boldsymbol{x} \; \text{©} \; \boldsymbol{y}$ and $\boldsymbol{w} = \boldsymbol{x} \; \text{ⓢ} \; \boldsymbol{y}$, then the following hold:

$$\boldsymbol{u} = \boldsymbol{G}_{0,0}^{-1}[(\boldsymbol{G}_{0,0}\boldsymbol{x}) \circ (\boldsymbol{G}_{0,0}\boldsymbol{y})]. \tag{32}$$

$$\boldsymbol{u} = \boldsymbol{G}_{0,\frac{1}{2}}^{-1}[(\boldsymbol{G}_{0,\frac{1}{2}}\boldsymbol{x}) \circ (\boldsymbol{G}_{0,0}\boldsymbol{y})]. \tag{33}$$

$$\boldsymbol{w} = \boldsymbol{G}_{\frac{1}{2},0}^{-1}[(\boldsymbol{G}_{\frac{1}{2},0}\boldsymbol{x}) \circ (\boldsymbol{G}_{\frac{1}{2},0}\boldsymbol{y})]. \tag{34}$$

$$\boldsymbol{w} = \boldsymbol{G}_{\frac{1}{2},\frac{1}{2}}^{-1}[(\boldsymbol{G}_{\frac{1}{2},\frac{1}{2}}\boldsymbol{x}) \circ (\boldsymbol{G}_{\frac{1}{2},0}\boldsymbol{y})]. \tag{35}$$

### 3.1.1.3 Discrete Trigonometric Transform

The family of DTTs comprises eight versions of the discrete cosine transform (DCT) and eight versions of the discrete sine transform (DST). Martucci formulated the DTTs through the convolution forms as defined in [76, Appendix]. The orthogonal-like relations between the inverse and forward DTTs are

$$\boldsymbol{T}_I^{-1} = \tfrac{1}{M}\boldsymbol{T}_I \text{ , } \boldsymbol{T}_{II}^{-1} = \tfrac{1}{M}\boldsymbol{T}_{III} \text{ , } \boldsymbol{T}_{III}^{-1} = \tfrac{1}{M}\boldsymbol{T}_{II} \text{ , and } \boldsymbol{T}_{IV}^{-1} = \tfrac{1}{M}\boldsymbol{T}_{IV} \text{ ,} \tag{36}$$

where the DTTs in both sides of each equality must be the same in the categories of cosine or sine and even or odd; and $M$ is $2N$ and $2N-1$ for the even and odd cases, respectively.

### 3.1.1.4 Analytic Transform based on GDFT and IGDFT

Marple proposed a DFT-based method for computing the analytic signal corresponding to a real-valued finite sequence of an even length [79]. We extend the result to the GDFTs as described in the following.

Via each GDFT, we can define the generic form for the analytic transform matrix:

$$A_q^+ = F_q^{-1} Z_q^+ W_q^+ (Z_q^+)^T F_q, \tag{37}$$

where $A_q^+$ is the $M \times M$ analytic transform matrix, $F_q$ is the GDFT matrix, $Z_q^+$ is the zero-padding matrix, and $W_q^+$ is the weighting matrix. Figure 3.4 depicts pictorially the reconstruction of the analytic transforms. The specific matrices are tabulated in Table 3.1, where $Z_{r,p,q}$ is defined as $[0_{p \times r} \; I_p \; 0_{p \times q}]^T$, where $I_p$ is the identity matrix of order $p$, and $0_{p \times q}$ is the $p \times q$ zero matrix. For instance, the $2N \times 2N$ O$^2$DFT-based analytic transform matrix $A_{IV}^{e+}$ is defined as

$$A_{IV}^{e+} = G_{\frac{1}{2},\frac{1}{2}}^{-1} \cdot \begin{bmatrix} I_N \\ 0_{N \times N} \end{bmatrix} \cdot 2 I_N \cdot [I_N \quad 0_{N \times N}] \cdot G_{\frac{1}{2},\frac{1}{2}}. \tag{38}$$

As can be seen in (37), the analytic transformation can discard the negative GDFT frequencies. Especially, let $x$ denote the real-valued column vector of length $M$ and $a = A_q^+ x$, then the analytic vector $a$ has two important properties. First, the real part of $a$ exactly equals the original vector:

$$\text{Re}(a_n) = x_n, \text{ for } n = 0, 1, \ldots, M - 1. \tag{39}$$

Second, the real and imaginary parts of $a$ are orthogonal:

$$\sum_{n=0}^{M-1} \text{Re}(a_n) \cdot \text{Im}(a_n) = 0. \tag{40}$$

24

For example, let $x = [1, -2, -3, 7, 11]^T$, then

$$A_{II}^{o+}x = [1+ j6.5489, -2+ j1.8809, -3- j4.0867, 7- j8.1816, 11+ j3.8385]^T,$$

$$A_{III}^{o+}x = [1- j6.1211, -2- j0.1534, -3- j6.9929, 7- j8.7628, 11+ j4.1978]^T.$$
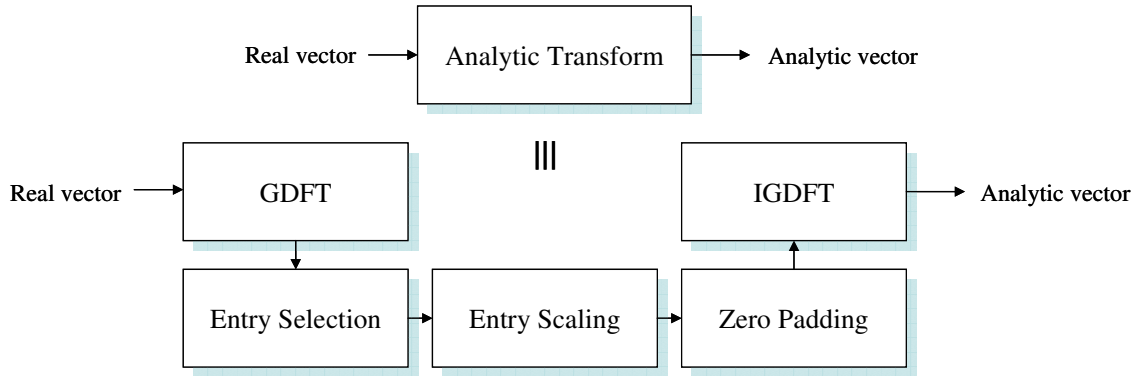


Figure 3.4. Reconstruction of analytic transform based on GDFT.

Table 3.1. Definitions of Related Matrices for Analytic Transforms

|  | $A_q^+$ | $F_q$ | $Z_q^+$ | $W_q^+$ |
|---|---|---|---|---|
| $M = 2N$ | $A_I^{e+}$ | $G_{0,0}$ | $Z_{0,N+1,N-1}$ | $diag\{12,2,...,2,1\}$ of order $N+1$ |
|  | $A_{II}^{e+}$ | $G_{0,\frac{1}{2}}$ |  | $diag\{12,2,...,2,1\}$ of order $N+1$ |
|  | $A_{III}^{e+}$ | $G_{\frac{1}{2},0}$ | $Z_{0,N,N}$ | $diag\{2,2,...,2\}$ of order $N$ |
|  | $A_{IV}^{e+}$ | $G_{\frac{1}{2},\frac{1}{2}}$ |  | $diag\{2,2,...,2\}$ of order $N$ |
| $M = 2N-1$ | $A_I^{o+}$ | $G_{0,0}$ | $Z_{0,N,N-1}$ | $diag\{1,2,2,...,2\}$ of order $N$ |
|  | $A_{II}^{o+}$ | $G_{0,\frac{1}{2}}$ |  | $diag\{1,2,2,...,2\}$ of order $N$ |
|  | $A_{III}^{o+}$ | $G_{\frac{1}{2},0}$ |  | $diag\{2,2,...,2,1\}$ of order $N$ |
|  | $A_{IV}^{o+}$ | $G_{\frac{1}{2},\frac{1}{2}}$ |  | $diag\{2,2,...,2,1\}$ of order $N$ |

### 3.1.1.5 DTT and Analytic Transform

The DTT spectra can be interpreted as the GDFT spectra of analytic vectors in the following way. Given a temporal column vector $x$ and the DTT vector $y = T_q x$. Then the IGDFT of the zero-padded scaled DTT equals the analytic transform of the symmetrized temporal vector, that is

$$A_q^+(E_q x) = F_q^{-1}(Z_q W_q'^+ y),$$

(41)

where $A_q^+$ is the analytic transform matrix, $E_q$ is the symmetric extension operator, $F_q^{-1}$ is the IGDFT matrix, $Z_q$ is the zero-padding matrix, and $W_q'^+$ is the weighting matrix. The specific types and definitions of the related matrices are defined in Tables B.2 and B.4 in Appendix B. The relation illustrated in (41) is depicted pictorially in Figure 3.5. We take the even DCT-IV for instance. For a real-valued column vector $x$ of length $N$, the specific expression of (41) is given by

$$A_{IV}^{e+} \cdot \left( \begin{bmatrix} I_N \\ -J_N \end{bmatrix} x \right) = G_{\frac{1}{2},\frac{1}{2}}^{-1} \cdot \left( \begin{bmatrix} I_N \\ 0_{N \times N} \end{bmatrix} \cdot 2I_N \cdot C_{IV}^e x \right),$$

(42)

where $J_N$ is the reversal matrix of order $N$.
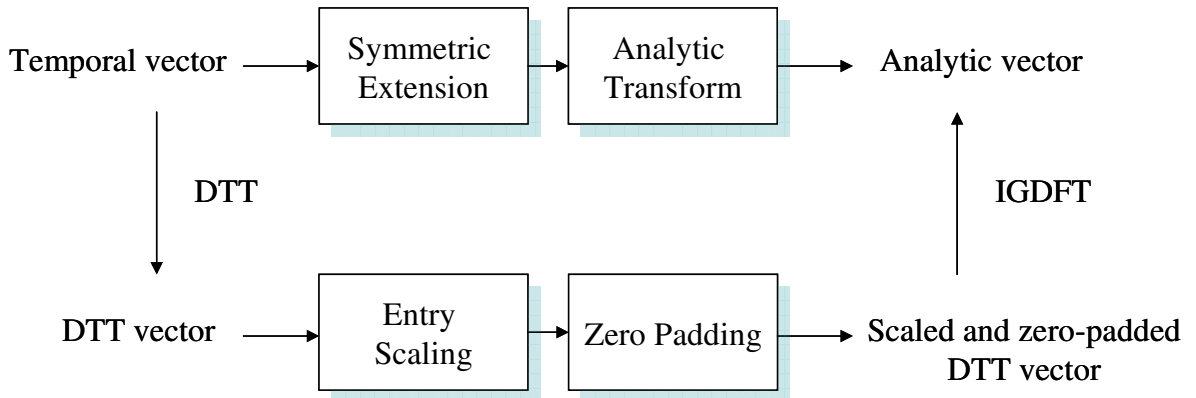


Figure 3.5. A pictorial representation of (41).

### 3.1.1.6 Autocorrelation and Temporal Envelope

The circular and skew-circular autocorrelations of a vector $\boldsymbol{x}$ of length $N$ are defined as

$$(\boldsymbol{r}_x^C)_n = \frac{1}{N}\left( \sum_{k=0}^{N-n-1} \boldsymbol{x}_k^* \cdot \boldsymbol{x}_{n+k} + \sum_{k=N-n}^{N-1} \boldsymbol{x}_k^* \cdot \boldsymbol{x}_{n+k-N} \right), \text{ for } n = 0, 1,\ldots, N-1. \tag{43}$$

$$(\boldsymbol{r}_x^S)_n = \frac{1}{N}\left( \sum_{k=0}^{N-n-1} \boldsymbol{x}_k^* \cdot \boldsymbol{x}_{n+k} - \sum_{k=N-n}^{N-1} \boldsymbol{x}_k^* \cdot \boldsymbol{x}_{n+k-N} \right), \text{ for } n = 0, 1,\ldots, N-1. \tag{44}$$

Just like the time-frequency duality between circular autocorrelations and DFT power spectra, we can have dualities between the GDFT-domain circular or skew-circular autocorrelations and the temporal (IGDFT-domain) envelopes as follows.

■  Consider a column vector y of length $N$.

(i) The relation between its skew-circular autocorrelation and IOTDFT/IO²DFT power spectra is given by

$$\boldsymbol{r}_y^S = \boldsymbol{G}_{0,\frac{1}{2}}[(\boldsymbol{G}_{0,\frac{1}{2}}^{-1}\boldsymbol{y}) \circ (\boldsymbol{G}_{0,\frac{1}{2}}^{-1}\boldsymbol{y})^*] = \boldsymbol{G}_{0,\frac{1}{2}}[(\boldsymbol{G}_{\frac{1}{2},\frac{1}{2}}^{-1}\boldsymbol{y}) \circ (\boldsymbol{G}_{\frac{1}{2},\frac{1}{2}}^{-1}\boldsymbol{y})^*]. \tag{45}$$

(ii) The relation between its circular autocorrelation and IDFT/IOFDFT power spectra is given by

$$\boldsymbol{r}_y^C = \boldsymbol{G}_{0,0}[(\boldsymbol{G}_{0,0}^{-1}\boldsymbol{y}) \circ (\boldsymbol{G}_{0,0}^{-1}\boldsymbol{y})^*] = \boldsymbol{G}_{0,0}[(\boldsymbol{G}_{\frac{1}{2},0}^{-1}\boldsymbol{y}) \circ (\boldsymbol{G}_{\frac{1}{2},0}^{-1}\boldsymbol{y})^*]. \tag{46}$$

Here the notation ( ◦ ) denotes the Hadamard product (i.e., the entry-wise product of two vectors or matrices).　　　　　　　　　　　　　　　　　　　□

By substituting (41) to (45) and (46), we immediately obtain two dualities between the DTT-domain circular or skew-circular autocorrelation and the temporal envelopes. In the following, the two dualities are expressed in generic form, and the specific types of transforms and autocorrelations are defined in Table B.3 in Appendix B.1.6.4.

■ Given a temporal vector $x$ and its DTT vector $y = T_q x$.

(i) Let $\hat{y} = Z_q W_q'^{+} y$, then

$$r_{\hat{y}} = K_q[(A_q^{+} E_q x) \circ (A_q^{+} E_q x)^{*}]. \tag{47}$$

(ii) Let $\ddot{y} = E_q' y$, then

$$r_{\ddot{y}} = K_q[(E_q x) \circ (E_q x)]. \tag{48}$$

Here $r_{\hat{y}}$ and $r_{\ddot{y}}$ are the circular or skew-circular autocorrelation of $\hat{y}$ and $\ddot{y}$ depending

on the type of $K_q$. □

For example, given a real-valued column vector $x$ of length $N$, the two dualities for even

DCT-IV are expressed below.

(i) Let $\hat{y} = \begin{bmatrix} I_N \\ 0_{N \times N} \end{bmatrix} \cdot 2I_N \cdot C_{IV}^{e} x$, then $r_{\hat{y}}^{S} = G_{0,\frac{1}{2}} \left[ \left( A_{IV}^{e+} \begin{bmatrix} I_N \\ -J_N \end{bmatrix} x \right) \circ \left( A_{IV}^{e+} \begin{bmatrix} I_N \\ -J_N \end{bmatrix} x \right)^{*} \right]$.

(ii) Let $\ddot{y} = \begin{bmatrix} I_N \\ -J_N \end{bmatrix} \cdot C_{IV}^{e} x$, then $r_{\ddot{y}}^{S} = G_{0,\frac{1}{2}} \left[ \left( \begin{bmatrix} I_N \\ -J_N \end{bmatrix} x \right) \circ \left( \begin{bmatrix} I_N \\ -J_N \end{bmatrix} x \right) \right]$.

To summarize, the dualities (47) and (48), corresponding to the Hilbert and power

envelopes respectively, provide the fundament for AR modeling in the DTT domain. In

Appendix B, we also confirm that the traditional Yule-Walker equations can be solved to yield

the AR parameters in the GDFT AR modeling problem.

## 3.1.2. Evaluation and Representation of Whitening Filter

Let $x$ denote the data vector and $y = T_q x$. According to (47) and (48), we can have the

squared Hilbert envelope or power envelope for shaping the reconstruction noise. As defined

in the two dualities, $r_{\hat{y}}$ and $r_{\ddot{y}}$ consist of the circular or skew-circular autocorrelation of

$\hat{y}$ and $\ddot{y}$ respectively, where

$$\hat{\pmb{y}} = [\hat{y}(0), \hat{y}(1),..., \hat{y}(M-1)]^T = \pmb{Z}_q \pmb{W}_q'^{+} \pmb{y} \quad \text{and} \quad \ddot{\pmb{y}} = [\ddot{y}(0), \ddot{y}(1),..., \ddot{y}(M-1)]^T = \pmb{E}_q' \pmb{y}.$$

Subsequently, the parameters of the whitening filter are obtained by solving the Yule-Walker equations. Since the relations in the two dualities are based on length $M$ instead of $N$, we assume that the whitening filter is applied to $\hat{\pmb{y}}$ covering $\pmb{y}$ in our derivation.

The whitening filter can be represented as a circulant or skew-circulant matrix [32] in the case of the circular or skew-circular convolution. By taking conjugate of both sides of (32)-(35) and assuming that the operands $\pmb{x}$ and $\pmb{y}$ are real-valued, we have the alternative relations:

$$\pmb{u} = N \cdot \pmb{G}_{0,0}[(\pmb{G}_{0,0}^{-1}\pmb{x}) \circ (\pmb{G}_{0,0}^{-1}\pmb{y})] ;$$

$$\pmb{u} = N \cdot \pmb{G}_{\frac{1}{2},0}[(\pmb{G}_{\frac{1}{2},0}^{-1}\pmb{x}) \circ (\pmb{G}_{0,0}^{-1}\pmb{y})] ;$$

$$\pmb{w} = N \cdot \pmb{G}_{0,\frac{1}{2}}[(\pmb{G}_{0,\frac{1}{2}}^{-1}\pmb{x}) \circ (\pmb{G}_{0,\frac{1}{2}}^{-1}\pmb{y})] ;$$

$$\pmb{w} = N \cdot \pmb{G}_{\frac{1}{2},\frac{1}{2}}[(\pmb{G}_{\frac{1}{2},\frac{1}{2}}^{-1}\pmb{x}) \circ (\pmb{G}_{0,\frac{1}{2}}^{-1}\pmb{y})] . \tag{49}$$

Hence, the matrix representation $\pmb{H}$ for the whitening filter can be diagonalized by GDFTs as

$$\pmb{H} = \pmb{F}_q \cdot \pmb{\Phi} \cdot \pmb{F}_q^{-1}, \tag{50}$$

where $\pmb{\Phi} = N \cdot diag\{(\pmb{G}_{0,b}^{-1}\pmb{\alpha})_n \mid n = 0,1,...,M-1\}$, where $b$ is 0 or 1/2 depending on the convolution type.

In the MPEG standard [2], [3], the TNS predictive error filter is performed through the linear convolution (filtering) in the transform domain. In matrix form, the linear convolution $\pmb{L}$ which is lower triangular is the same as the periodic convolution $\pmb{H}$ except for the upper triangular entries. Thus, by padding the input data with suitable zeros, the periodic convolution equals the linear convolution. However, to reconstruct $\pmb{y}$, all $M$ residuals are necessary to be transmitted to the decoder to perform the periodic deconvolution $\pmb{H}^{-1}$. In contrast, only the residuals corresponding to $\pmb{y}$ are required for the linear deconvolution $\pmb{L}^{-1}$ for

it is still lower triangular. Interestingly, if $L^{-1}u = v$ and $v_n = 0$ for $M - P \le n \le M - 1$, then $H^{-1}u = H^{-1}(Lv) = H^{-1}(Hv) = v$. Hence, $H$ and $H^{-1}$ are equivalent to $L$ and $L^{-1}$ on $\hat{y}$ and the related residuals respectively, and thus we can develop the TNS formulation on $\hat{y}$ in the periodic convolution/deconvolution manner.

### 3.1.3.  Formulation of TNS

We now establish the formulation of the shaping effect of TNS. First, the dequantized residual $d_r$ is given by

$$d_r = d + \varepsilon = H\hat{y} + \varepsilon, \tag{51}$$

where $d$ is the original residual, and $\varepsilon$ is the additive quantization noise. After deconvolution, the reconstructed spectral sequence $\hat{y}_r$ is given by

$$\hat{y}_r = H^{-1}d_r = H^{-1}(H\hat{y} + \varepsilon) = \hat{y} + H^{-1}\varepsilon. \tag{52}$$

In other words, the quantization noise $\varepsilon$ can be shaped by the periodic deconvolution $H^{-1}$ in the transform domain. Notice that only the part of $d$ corresponding to $y$ is quantized and transmitted from the encoder to the decoder. Let the zero-padded part be perfectly reconstructed, then the reconstructed noise exists only for non-zero-padded samples of $\hat{y}$. Thus we can confirm the equivalency of $H^{-1}$ and $L^{-1}$ on $\varepsilon$ to have $H^{-1}\varepsilon = L^{-1}\varepsilon = Z_q n$, where $Z_q$ is the zero-padding matrix corresponding to $T_q$, and $n$ denotes the reconstruction noise related to $W_q'^+ y$. This implies that some quantization noise should be "virtually" imposed on the $P$ samples after $y$ to correct the noise propagation in the open-loop prediction. To check the temporal shaping effect, $T_q^{-1}$ is applied to the part of $\hat{y}_r$ related to $y$, i.e., $(W_q'^+)^{-1}Z_q^T \hat{y}_r$, to yield the reconstructed temporal sequence $x_r$, where $(W_q'^+)^{-1}$ is multiplied for removing the scaling of $W_q'^+$ on $\hat{y}$. Before formulating $x_r$, we consider

another relation between IDTT and IGDFT as follows. For an arbitrary vector $z$, (41) can be rewritten as

$$A_q^+ E_q T_q^{-1} z = F_q^{-1} Z_q W_q'^+ z. \tag{53}$$

Thus, by the property that the real part of the analytic transform exactly equals the original sequence, for an arbitrary data vector $z$, we have

$$E_q T_q^{-1} z = \mathrm{Re}\{F_q^{-1} Z_q W_q'^+ z\}. \tag{54}$$

Consequently, by setting $z$ as $(W_q'^+)^{-1} Z_q^T \hat{y}_r$ to (54), the reconstructed symmetrized temporal sequence is given by

$$E_q x_r = E_q T_q^{-1} (W_q'^+)^{-1} Z_q^T \hat{y}_r = \mathrm{Re}\{F_q^{-1} Z_q W_q'^+ (W_q'^+)^{-1} Z_q^T \hat{y}_r\}. \tag{55}$$

Substituting (52) into (55) leads to

$$
\begin{aligned}
E_q x_r &= \mathrm{Re}\{F_q^{-1} Z_q Z_q^T (\hat{y} + H^{-1}\varepsilon)\} \\
&= \mathrm{Re}\{F_q^{-1} Z_q Z_q^T (Z_q W_q'^+ y + H^{-1}\varepsilon)\} \\
&= \mathrm{Re}\{F_q^{-1} Z_q W_q'^+ y + F_q^{-1} Z_q Z_q^T H^{-1}\varepsilon\} \\
&= \mathrm{Re}\{F_q^{-1} Z_q W_q'^+ y\} + \mathrm{Re}\{F_q^{-1} Z_q Z_q^T H^{-1}\varepsilon\} \\
&= E_q T_q^{-1} y + \mathrm{Re}\{F_q^{-1} H^{-1}\varepsilon\}.
\end{aligned}
\tag{56}
$$

In the last step in (56), the property (54) is used, and the product $Z_q Z_q^T$ can be removed due to $H^{-1}\varepsilon = Z_q n$. Then substituting (50) to (56) yields

$$E_q x_r = E_q x + \mathrm{Re}\{\Phi^{-1} F_q^{-1}\varepsilon\} = E_q x + \eta \circ \mathrm{Re}\{\psi \circ F_q^{-1}\varepsilon\}, \tag{57}$$

where column vectors $\eta$ and $\psi$ are defined by $\eta_i = |(\Phi^{-1})_{ii}|$ and $\psi_i = (\Phi^{-1})_{ii} \cdot \eta_i^{-1}$ for $i = 0,1,\ldots, M-1$. Hence, $\eta$ results in the temporal shaping effect. Furthermore, due to $\psi$, the imaginary part of $F_q^{-1}\varepsilon$ is also involved in the reconstruction noise.

Figure 3.6 illustrates a TNS analysis result based on order-12 AR modeling on the even DCT-IV coefficients of 64 audio samples at 8 kHz sampling rate. As shown in Figure 3.6 (c),

although only 64 quantization noise samples are applied to the 64 residual samples transmitted, the 12 "virtual" quantization noises indexed from 64 to 75 occur when analyzed with the skew-circular convolution. In Figure 3.6 (d), the original time-domain samples and the reconstructed noise are depicted to show the shaping effect. Also notice that the TNS processing is applied to a data segment of length 64 but is analyzed in the $O^2DFT$ domain of length 128. Because of symmetry, only one side is shown in this illustration.
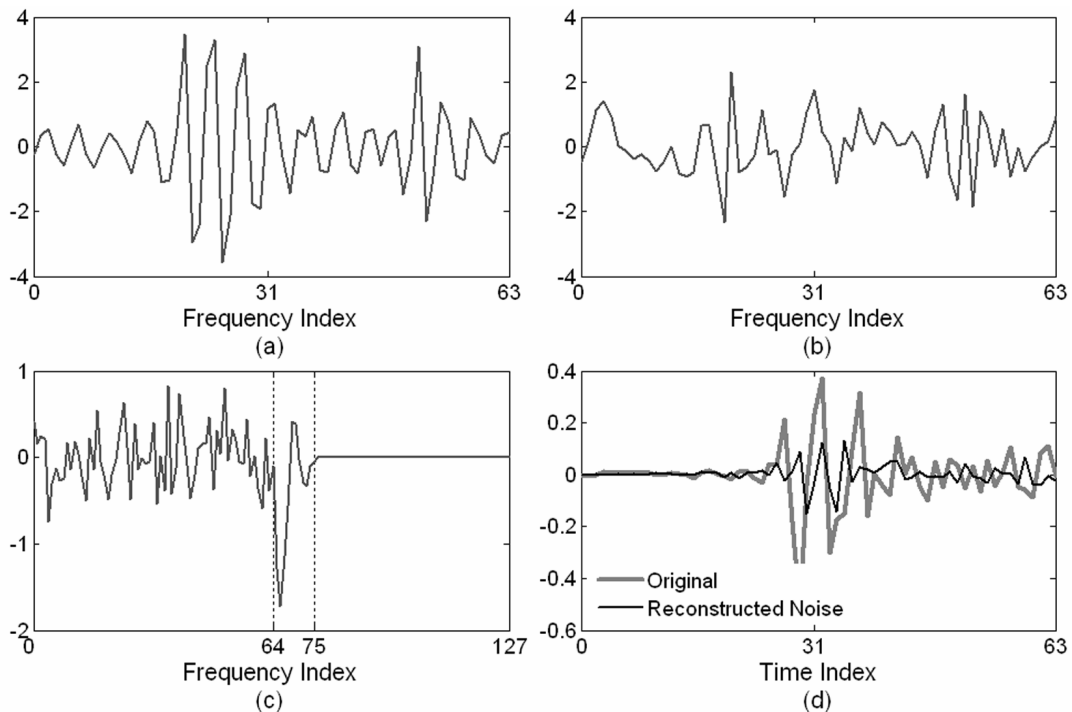


Figure 3.6. TNS analysis. (a) The even DCT-IV coefficients of an audio segment of 64 samples at 8 kHz. (b) The predictive residuals by the order-12 whitening filter corresponding to temporal Hilbert envelope. (c) The quantization noise on the residuals indexed 0~63, and the virtual quantization noise indexed 64~75. (d) The original time-domain samples and the reconstruction time-domain noise.

# 3.2. Artifacts in TNS
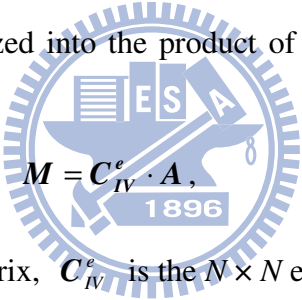
It has been known that the lapping operation of MDCT creates the time-domain aliasing and results in the undesired shaping of TNS at silence or weak-energy segments [27]. In this section, we explain the phenomenon through the relation between the MDCT and DCT-IV together with the fundamentals of AR modeling in DTTs.

## 3.2.1. Time-Domain Aliasing Noise

The $N \times 2N$ MDCT matrix $\boldsymbol{M}$ is defined as

$$[\boldsymbol{M}]_{k,n} = \cos\left(\frac{\pi(k+1/2)(n+1/2+N/2)}{N}\right) \text{ for } 0 \leq k \leq N-1 \text{ and } 0 \leq n \leq 2N-1. \quad (58)$$

The MDCT matrix can be factorized into the product of the "time-domain aliasing" matrix and the even DCT-IV matrix: [26]

$$\boldsymbol{M} = \boldsymbol{C}_{IV}^e \cdot \boldsymbol{A}, \quad (59)$$

where $\boldsymbol{M}$ is the $N \times 2N$ MDCT matrix, $\boldsymbol{C}_{IV}^e$ is the $N \times N$ even DCT-IV matrix, and $\boldsymbol{A}$ is the $N \times 2N$ time-domain aliasing matrix defined as

$$\boldsymbol{A} = \begin{bmatrix} \boldsymbol{0}_{N/2} & \boldsymbol{0}_{N/2} & -\boldsymbol{J}_{N/2} & -\boldsymbol{I}_{N/2} \\ \boldsymbol{I}_{N/2} & -\boldsymbol{J}_{N/2} & \boldsymbol{0}_{N/2} & \boldsymbol{0}_{N/2} \end{bmatrix}, \quad (60)$$

where $\boldsymbol{I}_{N/2}$ is the identity matrix and $\boldsymbol{J}_{N/2}$ is the reversal matrix. The factorization of the MDCT matrix is depicted pictorially in Figure 3.7. Consequently, the MDCT of a finite sequence of length $2N$ is equal to the even DCT-IV of the aliased sequence of length $N$. According to the time-domain aliasing cancellation (TDAC) principle [74], the aliasing effect can be perfectly removed by the overlap-and-add operation, which makes the MDCT especially attractive in audio coding for the blocking effect reduction. However, the time-domain aliasing operation of MDCT brings the "time-domain aliasing noise" artifact in TNS.

According to (47), when the linear predictive parameters are estimated in the DCT domain, the spectral magnitude response of the corresponding inverse filter should fit the temporal Hilbert envelope of the time-domain original signal. Equation (59) implies that the predictor evaluated from the MDCT of an audio segment is equal to that evaluated from the DCT-IV of the aliased one. More specifically, the duality formula (47) in this situation is given as follows.

Let $\hat{\boldsymbol{y}} = \begin{bmatrix} \boldsymbol{I}_N \\ \boldsymbol{0}_{N \times N} \end{bmatrix} \cdot 2\boldsymbol{I}_N \cdot \boldsymbol{C}_{IV}^e (\boldsymbol{A}\hat{\boldsymbol{x}})$ , then $\boldsymbol{r}_{\hat{\boldsymbol{y}}}^S = \boldsymbol{G}_{0,\frac{1}{2}} \left[ \left( \boldsymbol{A}_{IV}^{e+} \begin{bmatrix} \boldsymbol{I}_N \\ -\boldsymbol{J}_N \end{bmatrix} (\boldsymbol{A}\hat{\boldsymbol{x}}) \right) \circ \left( \boldsymbol{A}_{IV}^{e+} \begin{bmatrix} \boldsymbol{I}_N \\ -\boldsymbol{J}_N \end{bmatrix} (\boldsymbol{A}\hat{\boldsymbol{x}}) \right)^* \right]$ ,

where $\hat{\boldsymbol{x}}$ means a windowed input signal (e.g., when the sine window is applied, $\hat{\boldsymbol{x}} = diag\{\sin[\pi(n+1/2)/(2N)] \,|\, n = 0,1,2,...,2N-1\} \cdot \boldsymbol{x}$ ). Thus, rather than the original temporal Hilbert envelope, the inverse filter evaluated in the MDCT domain shapes the time-domain quantization noise according to the temporal Hilbert envelope of the aliased time-domain signal. Consequently, as illustrated in Figure 3.8, the artificial pre/post-aliasing artifacts are introduced due to the time-domain aliasing operation of MDCT. The aliasing noise may occur at perceptually sensitive positions (e.g., silence segments) and degrade the audio quality. Figure 3.9 and Figure 3.10 illustrate the pre-aliasing and post-aliasing artifacts, respectively.
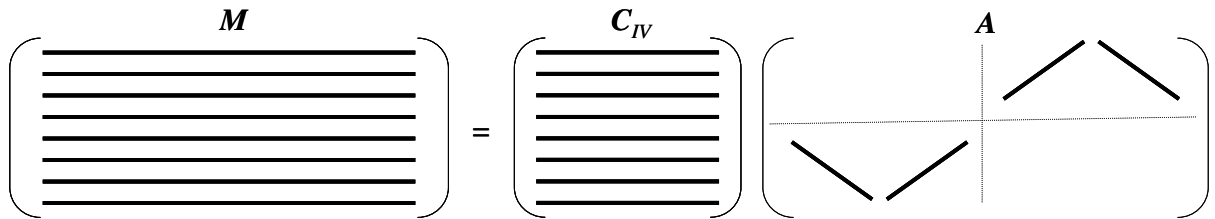


Figure 3.7. MDCT factorization. Identity and reversal matrices are represented by diagonal and anti-diagonal lines and row vectors are represented by horizontal lines.
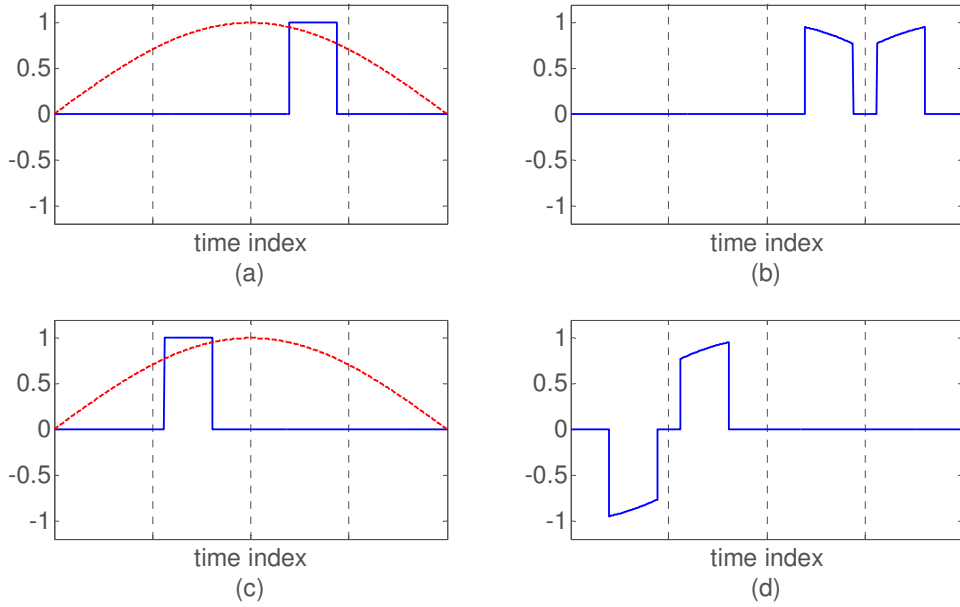
Figure 3.8. The time-domain aliasing of MDCT:(a) the input signal and the analysis sine window; (b) the post-aliasing signal corresponding to (a); (c) the input signal and the analysis sine window; (d) the pre-aliasing signal corresponding to (c).
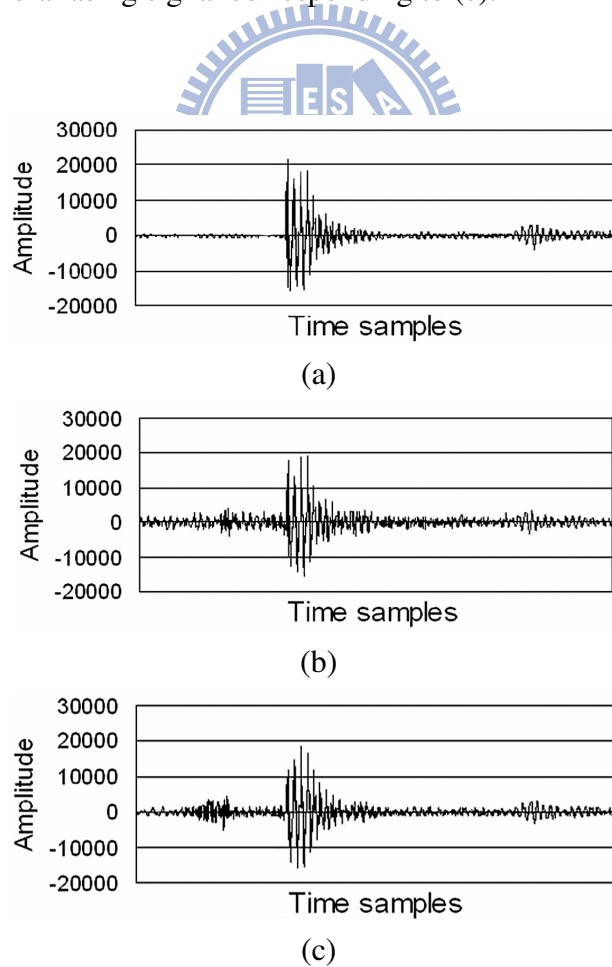


Figure 3.9. TNS pre-aliasing artifact: (a) original signal in time domain; (b) decoded signal without TNS; (c) decoded signal with TNS.

35

(a)



(b)



(c)
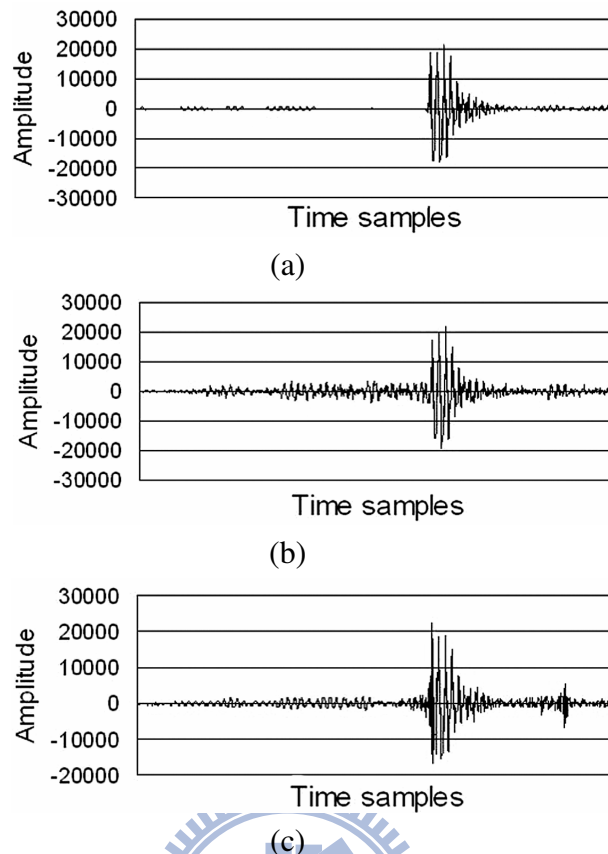
Figure 3.10. TNS post-aliasing artifact: (a) original signal in time domain; (b) decoded signal without TNS; (c) decoded signal with TNS.

### 3.2.2. Aliasing Noise by High-Order TNS

The accuracy of AR modeling generally rises with increasing predictive orders. This implies that the spectral magnitude response of the evaluated inverse filter should fit more and more accurately the temporal envelope of the original time-domain signal when the predictive order increases. For attack signals, the predictor shapes the abrupt changes of temporal attacks. Depending on the time-domain aliasing nature of MDCT mentioned above, the pre-aliasing or post-aliasing artifacts deteriorate with the TNS order due to the higher abrupt shaping. For instance, comparing Figure 3.11 (c) with (b) shows that the TNS of order 12 concentrates the quantization noise within the attack position but worsens the pre-aliasing artifact. Hence, the predictive order cannot be decided purely on complexity or coding gain.
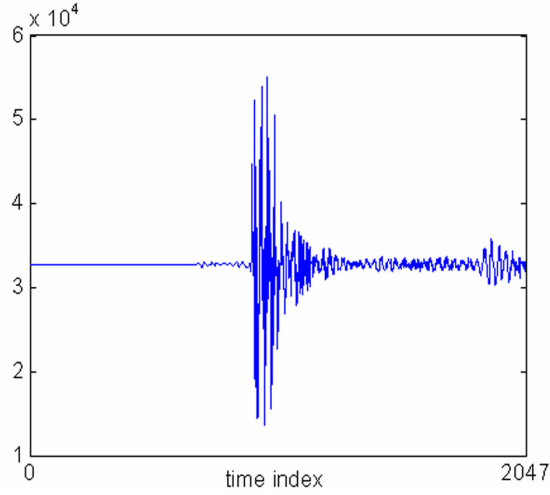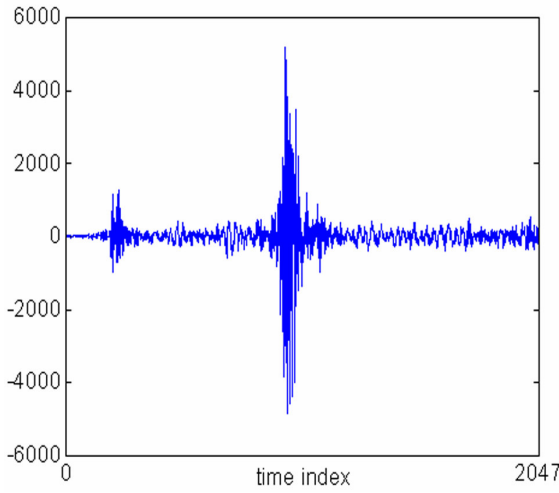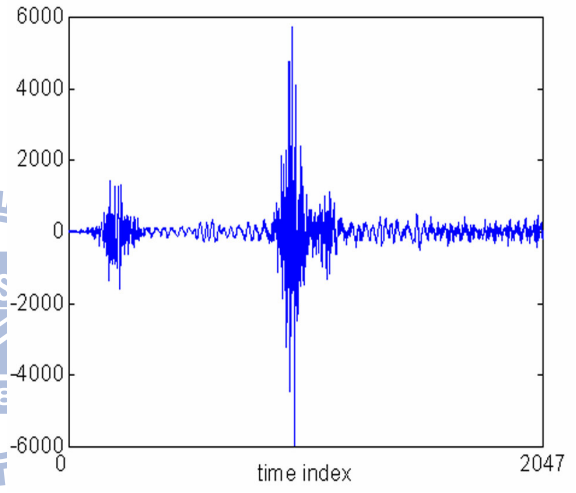
Figure 3.11. Deterioration of TNS aliasing artifact with high TNS orders: (a) original time-domain signal; (b) reconstruction noise with order-3 TNS; (c) reconstruction noise with order-12 TNS.

### 3.2.3. Artifacts Reducing Method

By applying the property that the IMDCT (inverse MDCT) matrix is the scaled transpose of the MDCT matrix to (59), we have

$$\tilde{M} = \frac{1}{N}M^T = \frac{1}{N}A^T C_{IV} = \frac{1}{N} \cdot \begin{bmatrix} 0 & I_{N/2} \\ 0 & -J_{N/2} \\ -J_{N/2} & 0 \\ -I_{N/2} & 0 \end{bmatrix} \cdot C_{IV}, \tag{61}$$

where $\tilde{M}$ is the $2N \times N$ IMDCT matrix. The factorization of the IMDCT matrix is depicted pictorially in Figure 3.12. Equation (61) specifies the symmetric structure of the IMDCT output and implies that the shaped quantization noise by TNS must have the same symmetric structure after the IMDCT conversion. Unlike the aliased original signal, the shaped quantization noise cannot be perfectly cancelled by the overlap-and-add operation. Accordingly, the time-domain aliasing noise always accompanies symmetrically with the shaped noise centralized in an attack. This means that the aliasing artifact cannot be avoided through the TNS filter design.

In audio coding, the window switch [1]-[3] is another mechanism for handling attack signals, where the start and stop windows are used in the transition between a long window and a short window. In [33], a method is proposed to detect attacks and to apply the start and stop windows in AAC to attenuate the aliasing noise (see Figure 3.13). Figure 3.14 illustrates the effect of the stop window. As shown in Figure 3.14 (d), the aliasing term of the original signal can be removed through the windowing operation, instead of the overlap-and-add operation. In the same way, the aliasing noise can be eliminated. Similar concept is adopted in MPEG-4 Low Delay AAC, where a window which exhibits only a small overlap between subsequent frames is provided to minimize the time-domain aliasing noise [34]. Figure 3.15 provides an example to compare the waveforms and spectrograms of several signals including the original signal, the decoded signal without TNS, the decoded signals with the TNS of order 3 and 12, and the decoded signal with the TNS of order 12 and the artifacts reducing method. A comparison of Figure 3.15 (h) and (i) shows that the stronger noise centralized in the aliasing segment arises in the case of TNS order 12. On the other hand, in Figure 3.15 (j), the time-domain aliasing noise of the decoded signal with TNS order 12 is eliminated by the artifacts reducing method.
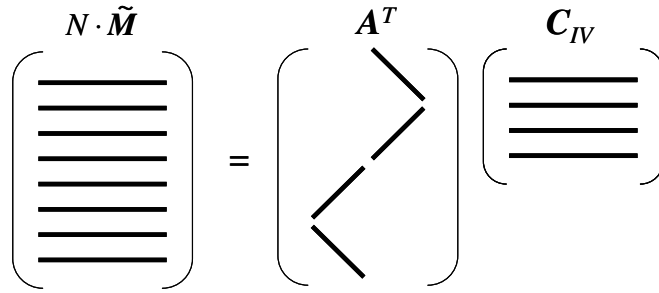
Figure 3.12. IMDCT factorization. Identity and reversal matrices are represented by diagonal and anti-diagonal lines and row vectors are represented by horizontal lines.
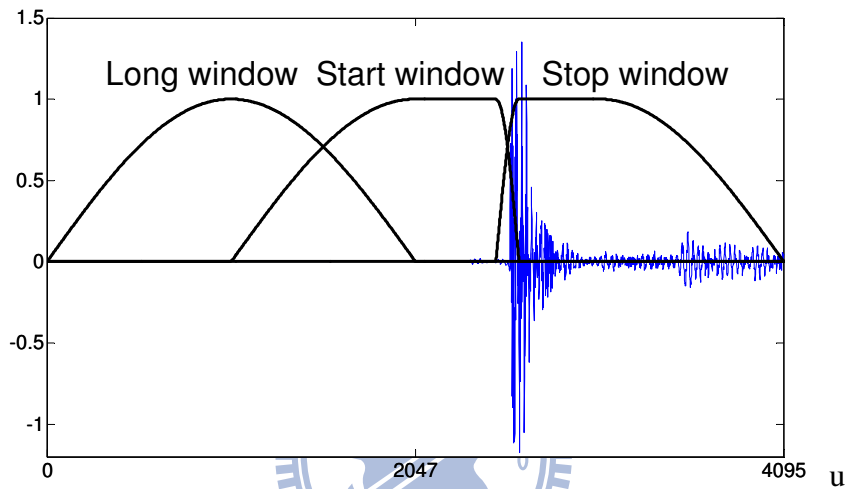


Figure 3.13. Artifact reducing method for TNS time-domain aliasing by the start and stop windows.
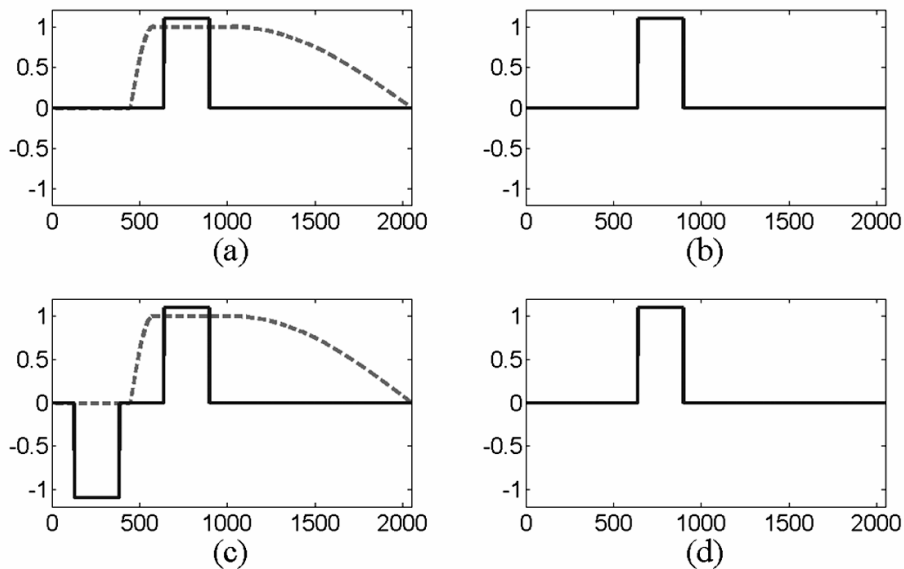


Figure 3.14. The effect of the stop window: (a) the input signal and the analysis stop window; (b) the windowed output; (c) output of IMDCT; (d) final output behind the synthesis stop window.
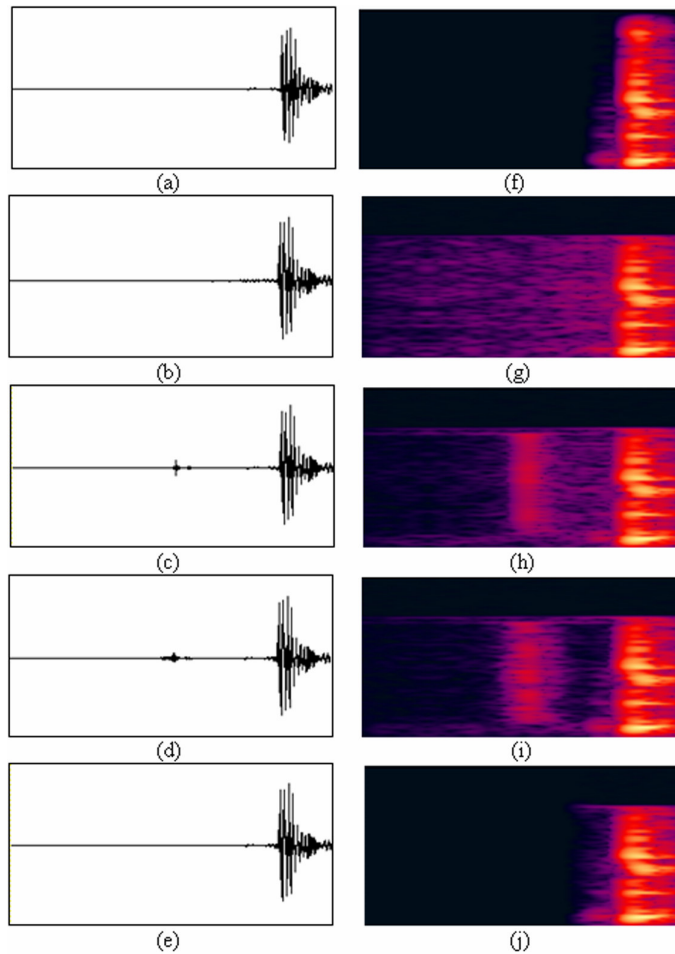
Figure 3.15. TNS artifact—Effect from the different TNS orders: (a) the original waveform; (b) the waveform without TNS; (c) the waveform with TNS order 3; (d) waveform with TNS order 12; (e) the waveform from the artifacts reducing method for the TNS with order 12 and; (f)-(j) the spectrograms corresponding to (a)-(e) respectively.

### 3.2.4. TNS by Hilbert Envelope and Power Envelope

Figure 3.16 illustrates the noise shaping effect of the Hilbert-envelope method and the power-envelope method, where the two order-12 AR modeling methods are applied to a transient audio segment of 2048 samples at 44.1 kHz. The inverted magnitude responses of the two skew-circular predictors corresponding to the Hilbert and power envelopes are aligned in energy and depicted in Figure 3.16 (c). The quantization noises on the residuals are simulated by a white random sequence shown in Figure 3.16 (d). The reconstructed temporal noises by the two predictors are shown in Figure 3.16 (e) and (f). As shown in Figure 3.16 (c),

the magnitude response of the predictor corresponding to the power envelope is sharper than that corresponding to the Hilbert envelope at the silence segment. Therefore, the pre-echo artifact in Figure 3.16 (f) has higher attenuation when compared with that in Figure 3.16 (e). The major difference of the two methods comes from the envelope estimation of the low frequency tones. The Hilbert envelope can avoid the smoothing effect by removing the low frequency lines in the calculation of the filter coefficients while applying the noise shaping to all the frequency lines to achieve similar effects as the power envelope method.
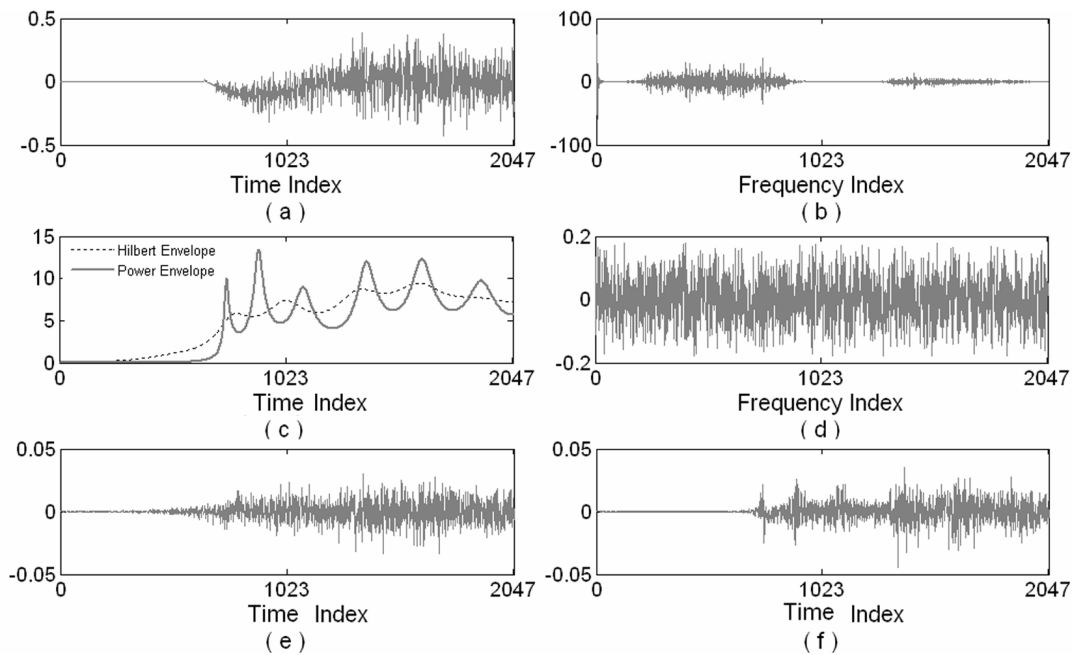


Figure 3.16. Comparison of TNS effect by the order-12 predictors corresponding to the Hilbert and power envelopes. (a) A transient audio segment of 2048 samples at 44.1 kHz. (b) The even DCT-IV coefficients. (c) The energy-aligned inverted magnitude responses of the two skew-circular predictors corresponding to the Hilbert and power envelopes. (d) The simulated quantization noise. (e) The reconstruction temporal noises by the predictor corresponding to the Hilbert envelope. (f) The reconstruction temporal noises by the predictor corresponding to the power envelope.

## 3.3.Concluding Remarks

In this chapter, the compact form of TNS has been established for 16 DTTs through the spectral AR modeling theory of finite discrete signals. According to the compact form, the well-known "time-domain aliasing noise" artifact associated with TNS in the MDCT domain has been explained analytically. The time-domain aliasing noise deteriorates with the TNS predictive order. A reduction method combining TNS and window switch has been proposed to reduce this artifact. We also compared the TNS effects by the Hilbert envelope and power envelope.
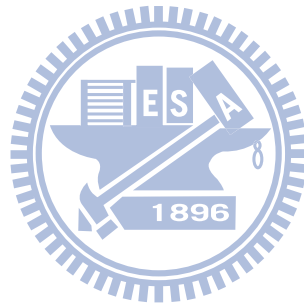
# CHAPTER 4
# ARTIFACTS IN
# SPECTRAL BAND REPLICATION

In contrast to the traditional transform or subband coding methods such as AAC and MP3, the SBR exploits the similarity between low frequency (LF) and high frequency (HF) spectra to reconstruct high bands by replicating low bands. The efficient coding method of HF brings several new types of artifact.

## 4.1. SBR Overview

SBR is a technique of bandwidth extension or high frequency reconstruction and can be combined with any audio core coders such as AAC and MP3. SBR reconstructs high bands by transposing and adjusting the replicated low bands thanks to the strong correlation of spectral harmonic characteristics. Only a small amount of side information, including spectral envelope data and control parameters for additional means such as inverse filtering and noise/sinusoidal addition, is transmitted from the encoder to the decoder for guiding the HF reconstruction. Since SBR requires significantly lower bit rate for high bands and reduces the underlying core coder bandwidth, the core encoder can compress the LF part with most of the available bits to achieve high coding efficiency.

As depicted in Figure 4.1, in addition to the analysis/synthesis filterbank, the SBR decoding has three major procedures. In the HF generator, the low bands split from the decoded LF signal are first transposed to HF. Subsequently, to control tonality, the inverse filtering is applied to the regenerated high bands to clip the undesired sinusoidal components from low bands. The inverse filtering is performed by in-band filtering using an adaptive spectral whitening filter. The second-order covariance method is employed to evaluate the

whitening filters on low bands. Furthermore, a chirp factor given from the bitstream is used to control the amount of inverse filtering by moving the two zeros of the LP filter toward the origin. The regenerated high band $x_k(n)$ for QMF subband $k$ and time slot $n$ is defined as:

$$x_k(n) = x_l(n) - a_l(1) \cdot c_k \cdot x_l(n-1) - a_l(2) \cdot c_k^2 \cdot x_l(n-2) , \qquad (62)$$

where $a_l(1)$ and $a_l(2)$ are the predictive coefficients estimated on the low band $x_l(n)$, and $c_k$ is the chirp factor whose range is between 0 and 0.98. In the envelope adjuster, the envelope of the regenerated high bands is scaled according to the transmitted envelope information that is represented by the average energies in time-frequency (T-F) grids (explained below). Subsequently, additional tones and random noise are compensated to adjust the tonality of the reconstructed high bands. Finally, all low and high bands are synthesized to generate a full-bandwidth decoded signal.

Figure 4.2 illustrates the reconstruction procedures of SBR in HE-AAC decoder. In the HF generator, the low QMF bands analyzed from the decoded LF AAC signal are replicated to HF and further inversely filtered (see Figure 4.2 (c)). In Figure 4.2 (d), the envelope of the replicated bands is adjusted; moreover, the compensation of tone and noise is applied to adjust the tonality of the reconstructed signal.
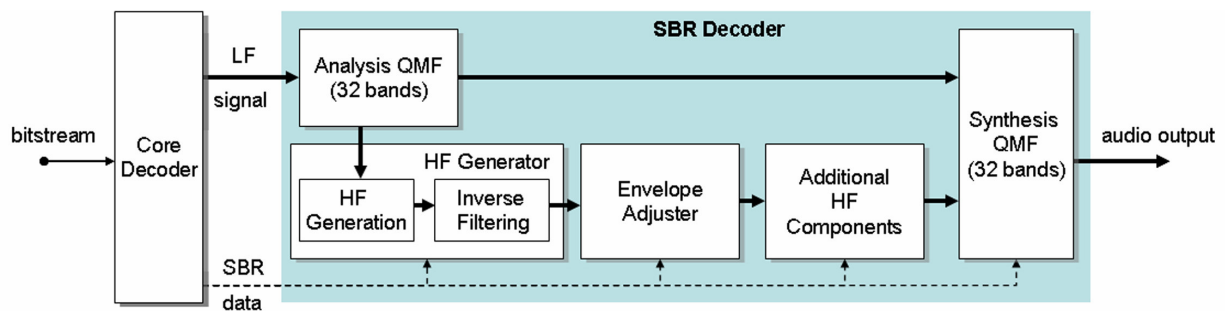


Figure 4.1. The block diagram of the SBR decoder.

(a)



(b)



(c)
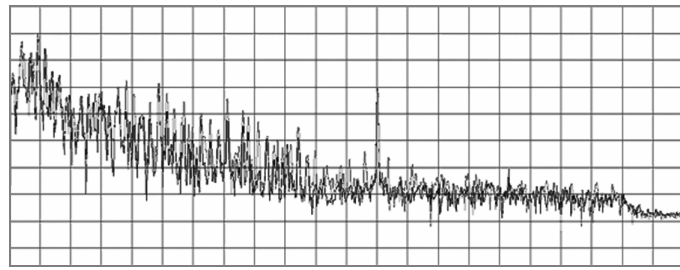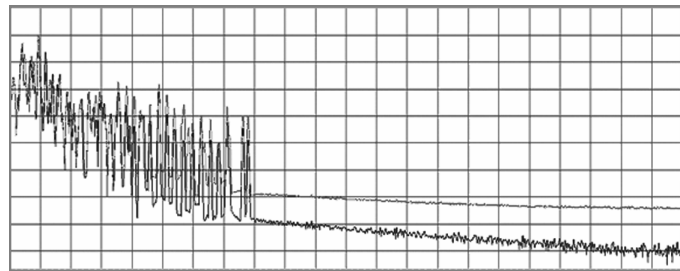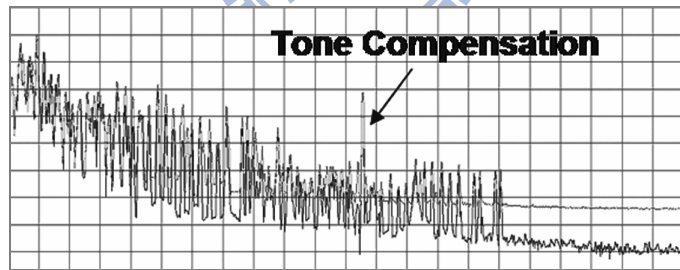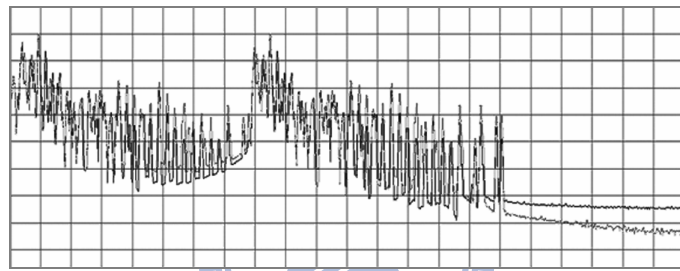


(d)

Figure 4.2. HF reconstruction process of SBR: (a) original spectrum; (b) decoded AAC LF spectrum; (c) HF generation by SBR; (d) HF adjustment by SBR.

The T-F grid for recording energy data (see Figure 4.3) is formed through the "time borders" and the frequency band borders that are indicated in "high/low resolution frequency band tables" [5]. The T-F grid determines the resolutions of data record units in the time and frequency dimensions. In the same way, the "noise-floor frequency table" and "limiter frequency table" are used to define the frequency resolution for noise compensation and

scaling-gain limitation, respectively. All the tables are constructed from the "master frequency band table" that can vary with spectral contents. The decision of T-F grid is one of the most critical design issues of the SBR encoder [61]. More details about the SBR algorithm can be found in [5]-[9].
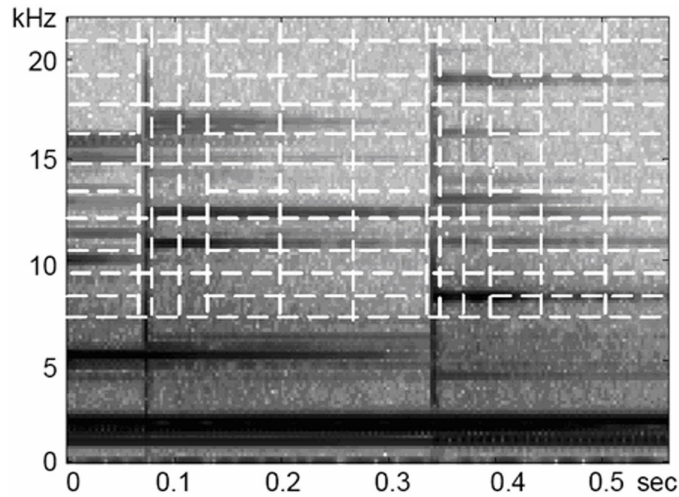


Figure 4.3. An instance of the T-F grid in SBR [7].

## 4.2. Tone Trembling Artifact

SBR aims to reconstruct high bands by replicating low bands. The "patching algorithm" [5] defined in the SBR syntax determines the correspondent relation between replicated low bands and original high bands. The patching algorithm has three constituting factors, namely the master frequency band table and the start as well as the stop boundaries of the SBR range. SBR permits to vary frequency band tables to adapt the frequency resolution of encoding according to spectral envelopes. Furthermore, depending on the encoding difficulty of the LF part, the SBR range is variable to adapt different conditions. However, a flexible design of SBR through switching tables or adjusting the SBR range to control the overall quality generates time-varying LF replication sources and thus leads to spectral discontinuities in

regenerated subbans. As illustrated in Figure 4.4, at the present frame, the 8th low band is replicated to the high band according to the patching algorithm, while the replicated source can be changed to the 10th low band at the next successive frame.

For noise-like signals, the resultant discontinuity level of reconstructed spectra is in general small, and the human hearing is insensitive to the artifact. But, for tonal signals, the human hearing is very sensitive to the artifact. To highlight this problem, Figure 4.5 provides an artificial example with frequently varying tables. The "billow-like" spectrogram originates from the replicated LF tones. This artifact sounds "trembling" and hence is named the "tone trembling" artifact. To analytically model the artifact, each specific replicated LF tone can be represented as

$$s(n) = A(n)\exp(i(\omega(n) \cdot n + \theta)), \tag{63}$$

where $A(n)$ denotes the amplitude which will be scaled by energy adjustment; $\omega(n)$ denotes the frequency; and $\theta$ denotes the phase. When the patching relation alters, $\omega(n)$ also changes with the frequency location. Hence, the replicated tone can be regarded as a frequency modulated signal, making the trembling artifact easy to visualize.
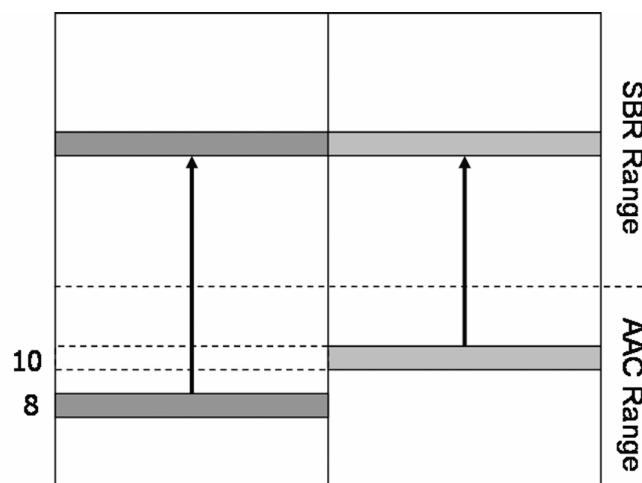


Figure 4.4. Patching source change for low band replication.

<center>(a)                                                      (b)</center>
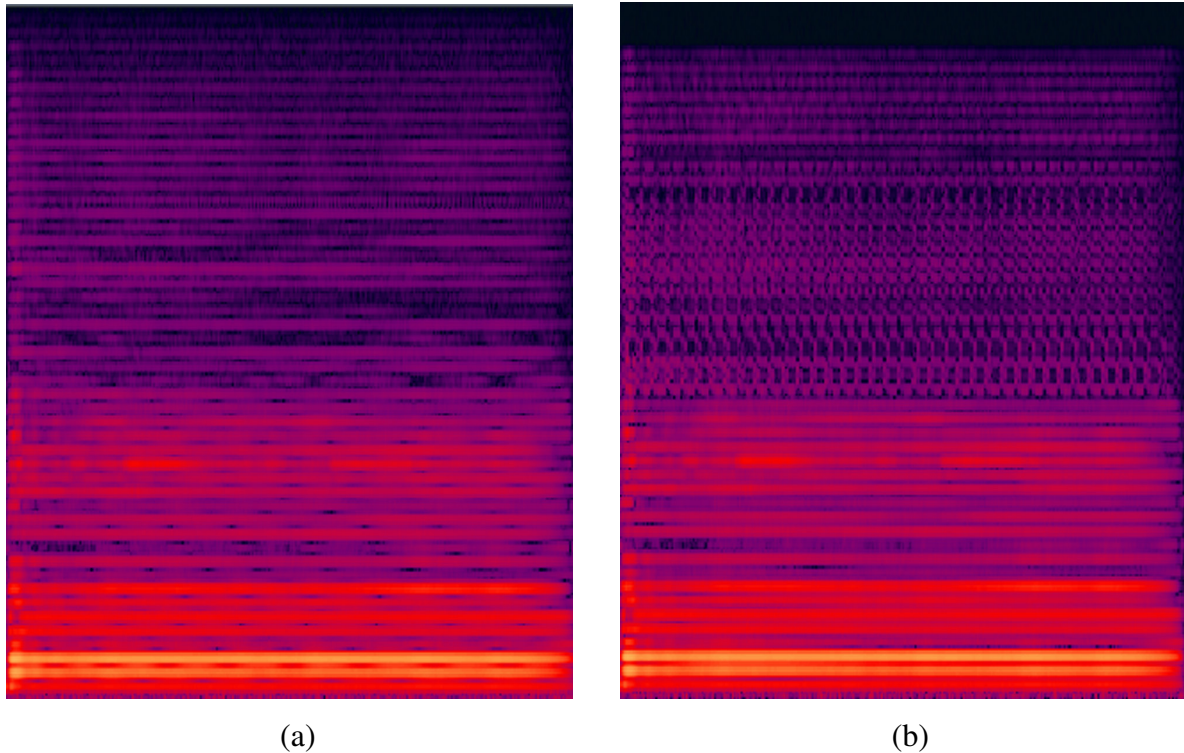
Figure 4.5. Tone trembling effect in spectrogram, where the vertical coordination is the frequency range from 0 to 22 kHz and the horizontal coordination is the time with frames: (a) normal spectrogram; (b) abnormal spectrogram.

## 4.3. Tone Shift Artifact

A tone-rich signal, e.g. flute sound, has a dense harmonic structure with regularly distributed tone series (see Figure 4.6 (a)). Tone-rich signals produce an apparent phenomenon in SBR called the "tone shift" artifact. As illustrated in Figure 4.6 (b), the direct replication of low bands leads to the obvious offsets between the recreated tones and the original ones. Exact matching of tones is almost impossible under direct replication.

SBR provides two mechanisms to correct spectral structures of replicated low bands. The first is the inverse filtering for eliminating undesired tones in replicated low bands. After that, the second mechanism allows to add sinusoids at the centers of the "high resolution frequency bands". Using the two mechanisms still cannot avoid the tone shift artifact owing to the limited locations of tone addition. Fortunately, it is not easy to perceive the slight offsets, which may be due to the lower perceptual resolution of the critical bands at the HF range.

<center>48</center>
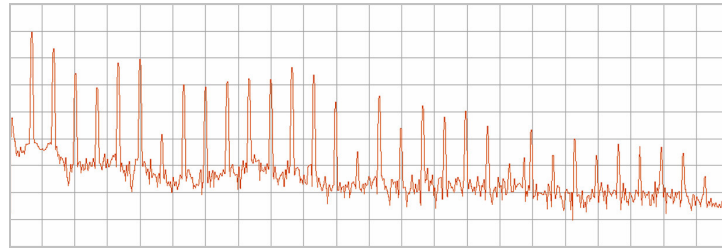
(a)
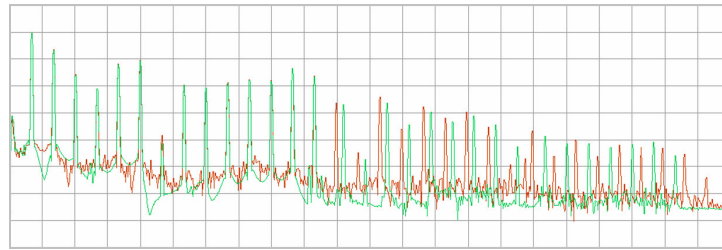


(b)

Figure 4.6. Tone shift effect: (a) original signal spectrum; (b) comparison of the original (with complete noise floor) and decoded spectra.

## 4.4. Noise Overflow and Tonal Spike

SBR can be regarded as a synthesis method for HF bands based on LF bands. The synthesis brings some distortions between the original and the simulated HF bands. The "noise overflow" artifact is a common one in SBR due to the inaccuracy of tone number and tone energy in a T/F grid. The noise overflow artifact (see Figure 4.7) produces a rasping sound and significantly degrades the perceived quality. Tonal signals, such as the glockenspiel signal in Figure 4.7 (b), are very susceptible to this artifact. The accuracy of tonality measure is crucial to this artifact because underestimating tonal energy and/or overestimating noise energy directly leads to the noise overflow. However, since the SBR syntax restricts the frequency location and number of compensated tones, the noise overflow artifact is still unavoidable even with an accurate tonality measure.

Another reason of the noise overflow artifact is on the choice of the two envelope adjustment modes, "interpolation" and "non-interpolation" [5]. Figure 4.8 illustrates the two adjustment modes, where the energies of the original HF bands and those of the

49

corresponding replicated LF bands in a T/F grid are shown in Figure 4.8 (a) and (b) respectively, and the dashed line means the average energy of the original HF bands in the grid. In the interpolation mode, the energy of each subband in a T-F grid is adjusted to fit the average energy of the original high bands as depicted in Figure 4.8 (c). In contrast, in the non-interpolation mode, not adjusted individually, all the replicated bands in a T/F grid are adjusted up or down to fit the average energy as depicted in Figure 4.8 (d). By comparing the resultant envelops in the two modes (see Figure 4.8 (c), (d)), we can observe that the interpolation mode generates a flat envelop in a grid, whereas the non-interpolation mode maintains the original envelop shape of the replicated low bands.



(a)
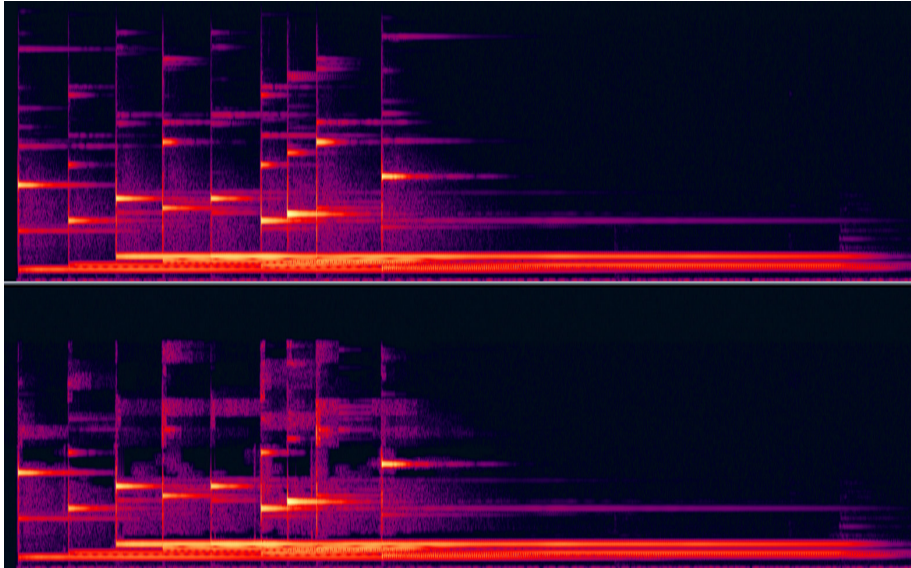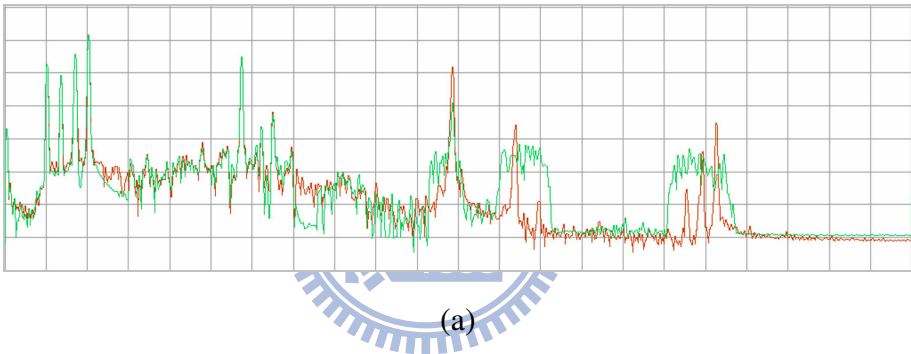


(b)

Figure 4.7. Noise overflow due to tone loss: (a) noise overflow due to the tone losing; (b) the spectrogram of glockenspiel with noise overflow (top: the original, down: the compressed).
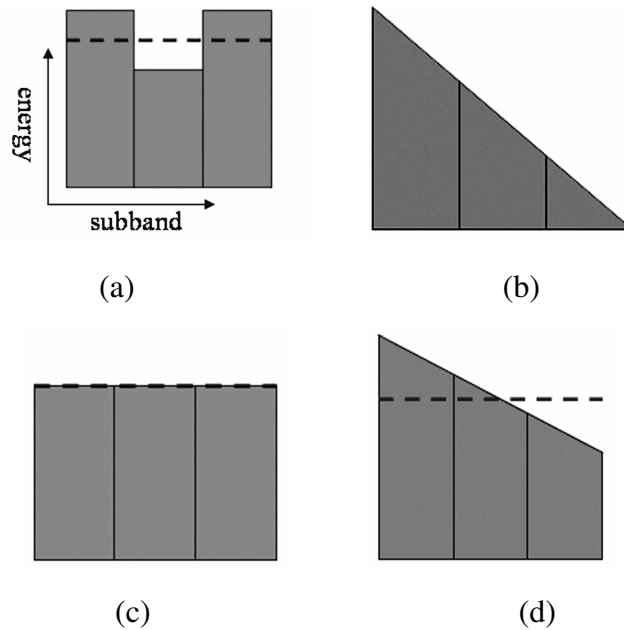
Figure 4.8. Envelope adjustment at interpolation and non-interpolation modes: (a) energies of the original HF bands in a grid; (b) energies of the replicated LF bands in a grid; (c) adjusted energies of the replicated LF bands at interpolation mode; (d) adjusted energies of the replicated LF bands at non-interpolation mode.

In the interpolation mode, the inherent characteristic of flat envelop cannot fit well sharp envelopes of tonal bands. Hence, the interpolation mode needs to be considered carefully for tonal signals due to the noise overflow effect. In Figure 4.9, the original signal contains one tone in the indicated passband. Although a tone is replicated from LF, it is overwhelmed by the amplified noise in the interpolation mode. Compensating the last two tones avoids the artifact because the tonality is maintained by the tone addition mechanism. Figure 4.10 provides a counterpart without tone compensation, which reveals the immunity of the mechanism to the noise overflow artifact in the interpolation mode. Figure 4.11 compares the adjusted spectra in the two modes, where a serious noise overflow artifact occurs in the interpolation mode, whereas the envelop structure of the replicated low bands is maintained in the non-interpolation mode.

51

Oppositely, compensating excessive tones or insufficient noises makes a noise floor underflow and leads to the "tonal spike" artifact (see Figure 4.12) which produces a "metallic" sound.
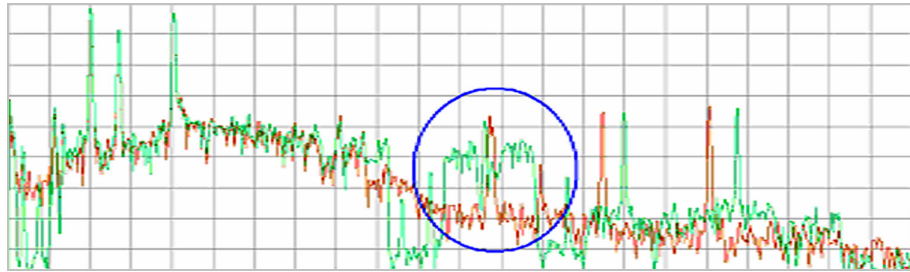


Figure 4.9. Noise overflow with tone compensation in interpolation mode.



Figure 4.10. Noise overflow without tone compensation in interpolation mode.
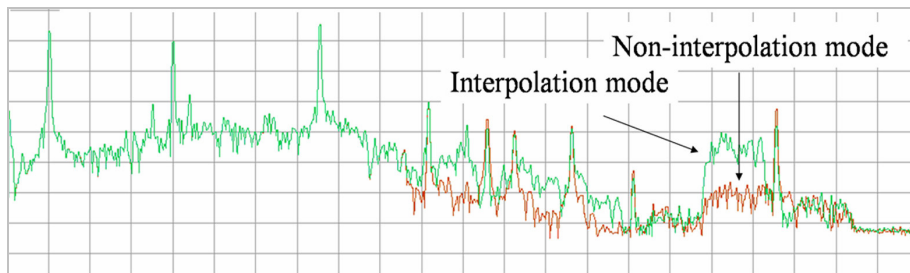


Figure 4.11. Noise overflow in interpolation and non-interpolation modes.
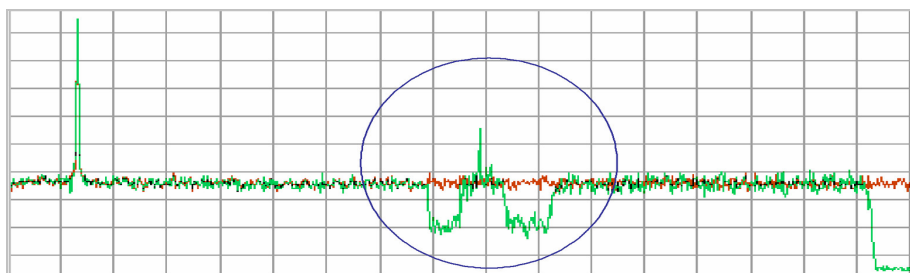


Figure 4.12. Tonal spike artifact.

# 4.5.Sawtooth Artifact

SBR decoder provides the "limited gain" mechanism [5] for avoiding excessive noise substitution which leads to serious noise overflow artifacts. The "limited gain" value $\Phi_g$ is evaluated as (64) for a limiter grid defined by the limiter frequency band table and time borders,

$$\Phi_g = \sqrt{E_g^H / E_g^L} \cdot \kappa,$$
(64)

where $E_g^H$ and $E_g^L$ are the energies of the original HF and the replicated LF bands covered within the $g$th limiter grid; $\kappa$ can be chosen as 0.70795, 1, 1.41254 or $10^{10}$ ($\kappa = 10^{10}$, i.e. the limited gain mechanism is turned off). The limited gain restricts adaptively the upper bound of the maximum gain value for envelope adjustment so as to limit the degree of revision on the replicated low bands. The noise overflow artifact generally arises from a relatively larger scaling gain compared to other gains in a limiter grid. Therefore, restricting the upper bound can restrain the noise overflow artifact.

However, this protection mechanism brings about another artifact, named the "sawtooth" artifact (see Figure 4.13 (b)). In Figure 4.13 (a), the original spectrum has a steep slope in the LF part and a flat slope in the HF part. To flat the steep slop for the HF part, some scaling gains must be much larger than others. The limited gain restrains the larger scaling gains and hence destroys the slop adjustment in the reconstructed spectrum.

(a)

(b)

(c)
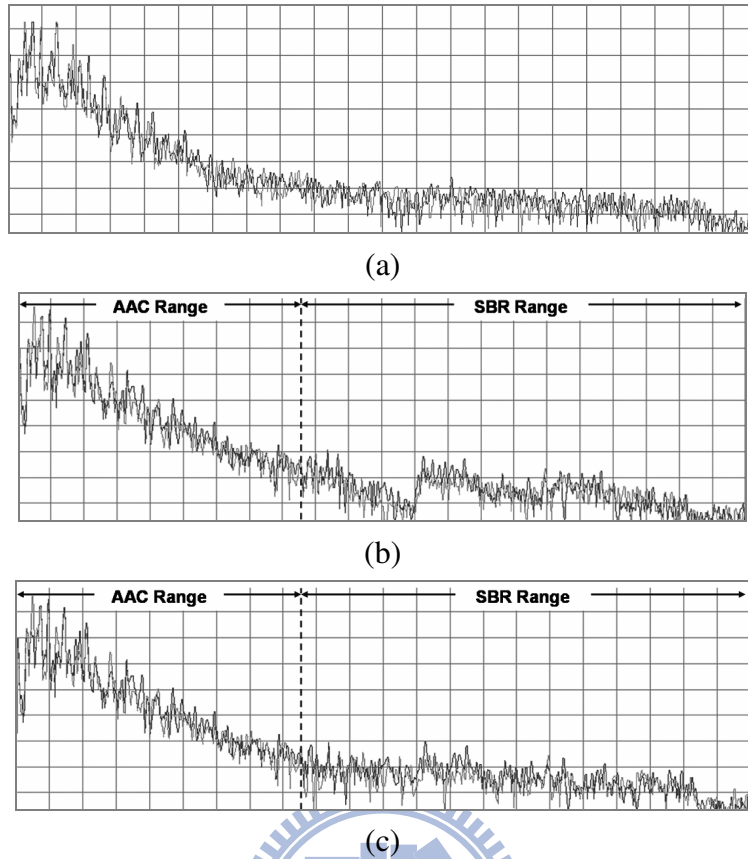
Figure 4.13. Illustration of sawtooth artifact: (a) original audio signal spectrum; (b) decoded spectrum with sawtooth effect due to the limited gain mechanism; (c) decoded spectrum without sawtooth effect by turning off the limited gain mechanism.

## 4.6. Beat Artifact

When two tones are close to each other in frequency, their mutual interference generates amplitude fluctuation at a regular rate. The fluctuation in amplitude is known in the audio industry as the "beat" phenomenon [51]. For instance, when two equal-amplitude sine waves occur simultaneously, the resultant signal can be expressed as

$$x(t) = \sin(\omega_1 t) + \sin(\omega_2 t + \phi) = 2\cos(\Delta\omega \cdot t + \tfrac{\phi}{2})\sin(\overline{\omega}t + \tfrac{\phi}{2}) , \qquad (65)$$

where $\Delta\omega = (\omega_2 - \omega_1) / 2$, and $\overline{\omega} = (\omega_2 + \omega_1) / 2$. Once the frequencies of the two sine waves are close, i.e. $\Delta\omega$ is small, a special period is generated because the very low frequency cosine curve shapes the sine wave of a higher frequency. SBR has risks to generate the beats artifact

54

because the tones patched from low bands or the compensated ones have inaccurate positions. For example, as shown in Figure 4.14 (c), after band replication (also see Figure 4.15), one replicated tone is closed to another tone in the low band. Figure 4.14 (d) shows that the cosine envelope is imposed on the signal waveform. In perception, the fluctuation can be perceived obviously.



(a)

(b)

(c)

(d)
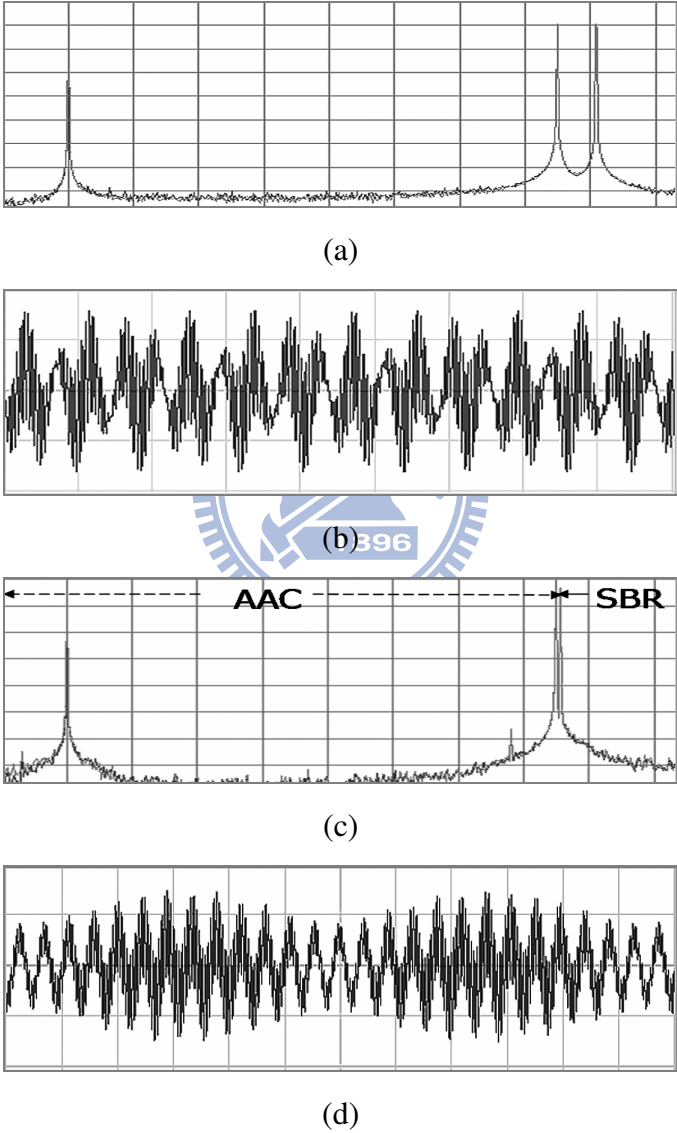
Figure 4.14. Beat artifact: (a) original spectrum containing two tones with large distance; (b) time-domain waveform for (a); (c) decoded spectrum containing two tones with small distance; (d) time-domain waveform for (c).
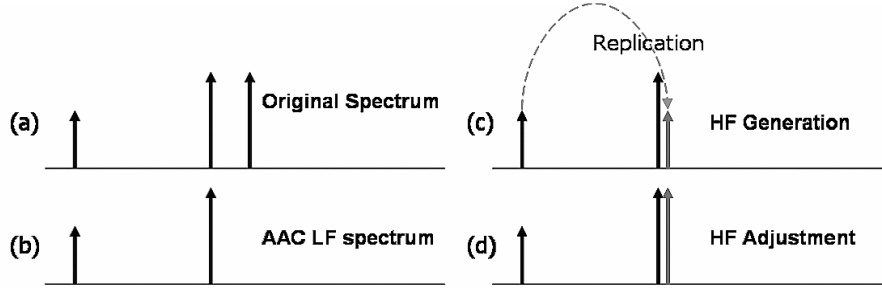
Figure 4.15. Explication of the beat artifact in Figure 4.14: (a) original spectrum; (b) decoded AAC LF spectrum; (c) HF generation by SBR; (d) HF adjustment by SBR.

# 4.7. Linear Predictive Bias on CEMFB Subbands

Rather than the cosine modulated filterbank (CMFB) commonly employed in audio coding, SBR utilizes the comparatively high-complexity complex-exponential modulated filterbank (CEMFB) [8] to eliminate main alias terms and thus avoid the alias artifact introduced from spectral adjustment or equalization. In this section, however, we demonstrate that when applied to the CEMFB subbands, the conventional LP method defined in the SBR standard has natively the predictive bias which affects the whitening effect and the noise-to-signal ratio (NSR) measure. We demonstrate the predictive bias through the first-order and second-order autoregressive (AR) modeling on analytic signals together with the empirical verification on the CEMFB subbands. Subsequently, the new filter, named the decimation-whitening filter, is proposed to remove the bias for the SBR algorithm.

## 4.7.1. CEMFB Subbands and Analytic Signals

The discrete-time analytic signal $x_+(n)$ corresponding to a real signal $x(n)$ [52] is defined as $x(n) + j\hat{x}(n)$, where $\hat{x}(n)$ denotes the discrete-time Hilbert transform of $x(n)$:

$$\hat{x}(n) = \sum_{k=-\infty, k \neq 0}^{\infty} \frac{2}{\pi} \cdot \frac{\sin^2(\pi k / 2)}{k} \cdot x(n-k). \tag{66}$$

In the frequency domain, the relation between the original and analytic signals is given by

$$X_+(\omega) = \begin{cases} 2X(\omega) & \forall\, 0 < \omega < \pi \\ 0 & \forall\, -\pi < \omega < 0 \end{cases}. \tag{67}$$

Similarly, the analytic signal $x_-(n)$ containing merely the negative spectrum can be defined as $x(n) - j\hat{x}(n)$. For convenience, we call $x_+(n)$ and $x_-(n)$ the positive and negative analytic signals, respectively.

The analysis and synthesis filters of the 64-channel CEMFB system used in SBR are defined by

$$h_k(n) = f_k(n) = p(n) \cdot \exp\left( \frac{j\pi}{2M}(2k+1)(n - N/2) \right), \tag{68}$$

for $k = 0,\ldots, M - 1$, where $M$ is the number of channels, and $N$ is the order of the prototype filter $p(n)$. Compared with the CMFB, the CEMFB adds an imaginary part that consists of sine modulated versions of the same prototype filter, which can be interpreted as the Hilbert transforms of the real part. Accordingly, the resultant subbands decimated by $M$ can be approximately regarded as the analytic signals of the real output obtained from the CMFB [8]. Moreover, the CEMFB subbands alternately consist of positive and negative analysis signals. In the absence of either the positive or negative side band, the excitation noise for each CEMFB subband can be also regarded as the analytic signal that has flat power spectrum density (PSD) in the other side band; but it is no longer white. Nevertheless, the whiteness of the noise is a desirable property for confirming the asymptotically unbiased LP estimation of spectral peaks [53]. This property implies that the absence of one side band leads to the predictive bias that is demonstrated in Section 4.7.2.

## 4.7.2. Linear Predictive Bias on Analytic Signals

This subsection demonstrates and quantifies the predictive bias on analytic signals through the first-order and second-order LPs. We first analyze the bias through the theoretical derivation on ideal analytic signals. Next, we confirm through the empirical verification the bias on the CEMFB subbands which are generated by the modulated non-ideal prototype filter.

The affection of the bias in SBR will be discussed in Section 4.7.3. Our derivation and illustration are given according to the positive analytic signal model, and the same result can be extended to the negative analytic signal model.

### 4.7.2.1 First-Order LP on Analytic Signals of First-Order AR Model

Consider the analytic signal modeled by the AR model with single pole $r_0 e^{j\theta_0}$ in the frequency domain:

$$X_+(\omega) = \frac{E(\omega)}{1 - r_0 e^{j\theta_0} e^{-j\omega}}, \tag{69}$$

where the PSD of the excitation signal $E(\omega)$ is assumed to be 1 for $0 < \omega < \pi$ and 0 for $\pi < \omega < 2\pi$, and the pole locates inside the upper half of the unit circle. The mean-square error function of the first-order predictive filter $re^{i\theta}z^{-1}$ on the single-pole analytic signal is expressed as

$$F(r,\theta) = \int_0^\pi \left| \frac{1 - re^{j\theta}e^{-j\omega}}{1 - r_0 e^{j\theta_0} e^{-j\omega}} \right|^2 d\omega = \int_0^\pi \frac{1 - 2r\cos(\omega - \theta) + r^2}{1 - 2r_0 \cos(\omega - \theta_0) + r_0^2} d\omega. \tag{70}$$

The minimum mean-square error (MMSE) predictive filter can be obtained through solving the two equations: $\partial F/\partial \theta = 0$ and $\partial F/\partial r = 0$. Thus, in polar coordinates, the conditions of the zero position $(\tilde{r}, \tilde{\theta})$ of the MMSE filter can be derived as

$$A(\tilde{\theta}) = \int_0^\pi \frac{\sin(\omega - \tilde{\theta})}{1 - 2r_0 \cos(\omega - \theta_0) + r_0^2} d\omega = 0, \tag{71}$$

$$B(\tilde{r}, \tilde{\theta}) = \int_0^\pi \frac{\cos(\omega - \tilde{\theta}) - \tilde{r}}{1 - 2r_0 \cos(\omega - \theta_0) + r_0^2} d\omega = 0. \tag{72}$$

As shown in Appendix C.1, the angle of the zero of the MMSE predictive filter is solved as

$$\tilde{\theta} = \theta_0 + \arctan\left(\frac{S}{C}\right), \tag{73}$$

and the radius of the zero of the MMSE predictive filter is derived as

58

$$\tilde{r} = \frac{\cos\left(\arctan\left(\dfrac{S}{C}\right)\right) \cdot C + \sin\left(\arctan\left(\dfrac{S}{C}\right)\right) \cdot S}{K} = \frac{\sqrt{C^2 + S^2}}{K}, \tag{74}$$

where $S, C$, and $K$ are defined as follows:

$$S = \frac{1}{2r_0} \ln\left( \frac{1 + 2r_0 \cos(\theta_0) + r_0^2}{1 - 2r_0 \cos(\theta_0) + r_0^2} \right), \tag{75}$$

$$C = \frac{(1 + r_0^2)K - \pi}{2r_0}, \tag{76}$$

$$K = \frac{1}{1 - r_0^2}\left[ T + \arctan\left( \frac{\sin(\theta_0)}{\cos(\theta_0) + r_0^{-1}} \right) - \arctan\left( \frac{\sin(\theta_0)}{\cos(\theta_0) - r_0^{-1}} \right) \right], \tag{77}$$

where

$$T = \begin{cases} \pi - \arctan\left( \dfrac{\sin(\theta_0)}{\cos(\theta_0) + r_0} \right) + \arctan\left( \dfrac{\sin(\theta_0)}{\cos(\theta_0) - r_0} \right), & |\cos(\theta_0)| > r_0 \\[2mm] \dfrac{3\pi}{2} + \arctan\left( \dfrac{\sin(\theta_0)}{\cos(\theta_0) - r_0} \right), & \cos(\theta_0) = -r_0 \\[2mm] 2\pi - \arctan\left( \dfrac{\sin(\theta_0)}{\cos(\theta_0) + r_0} \right) + \arctan\left( \dfrac{\sin(\theta_0)}{\cos(\theta_0) - r_0} \right), & |\cos(\theta_0)| < r_0 \\[2mm] \dfrac{\pi}{2} - \arctan\left( \dfrac{\sin(\theta_0)}{\cos(\theta_0) + r_0} \right), & \cos(\theta_0) = r_0 \end{cases} . \tag{78}$$

### 4.7.2.2 General case of $r_0 > 0$

Equation (73) shows an angle bias, $\arctan(S/C)$, between $\tilde{\theta}$ and $\theta_0$, which is non-zero except the case of $\theta_0 = \pi/2$. Moreover, it can be shown that $A(\theta_0) \cdot A(\pi/2) < 0$ except $\theta_0 = \pi/2$. By Root Location Theorem, the root of (71) locates within the open interval between $\theta_0$ and $\pi/2$. Therefore, in general, the angle of the zero of the MMSE filter is biased from $\theta_0$ toward $\pi/2$ and cannot match the pole $r_0 e^{i\theta_0}$ of the AR model. Figure 4.16 illustrates that the angle bias with $r_0 = 1/2$ increases as $\theta_0$ is far away from $\pi/2$. By substituting $\theta_0 = \pi/2$ into (75)-(77) and using the trigonometric property $\arctan(-\beta) = -\arctan(\beta)$ and $\arctan(1/\alpha) = \pi/2 - \arctan(\alpha)$ for $\alpha > 0$, it can be derived that

$$\tilde{r} = r_0 + \frac{1-r_0^2}{r_0} \cdot \frac{2\arctan(r_0)}{\pi + 4\arctan(r_0)}. \tag{79}$$

Although $\theta$ is fitted to $\theta_0 = \pi/2$, there exists a bias between $r$ and $r_0$ in (79). Figure 4.17 depicts the radius curve corresponding to $\theta_0 = \pi/2$ together with those corresponding to $\theta_0 = \pi/4$ and 0. The curves show that the radius bias increases as the pole of the predicted spectrum moves away the unit circle. This trend implies that the prediction on noise-like signals should have a larger radius bias than that on tonal signals.
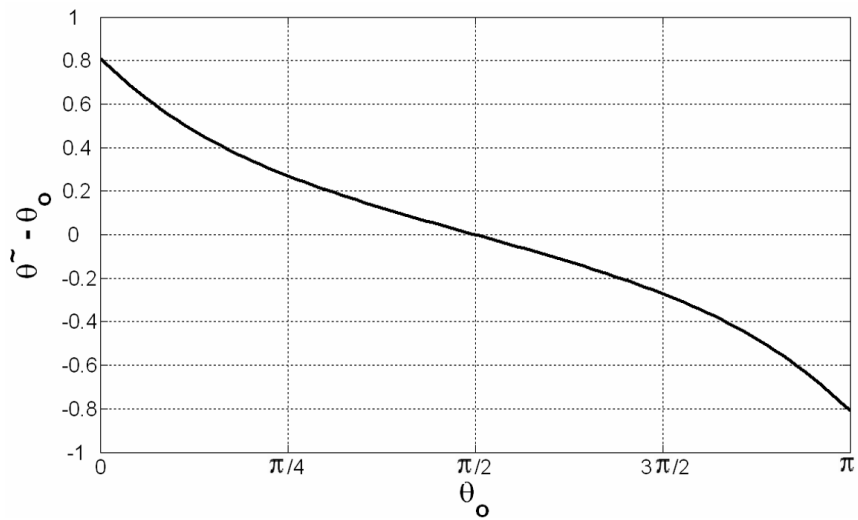


Figure 4.16. The angle biases for different $\theta_0$ values with $r_0 = 1/2$.
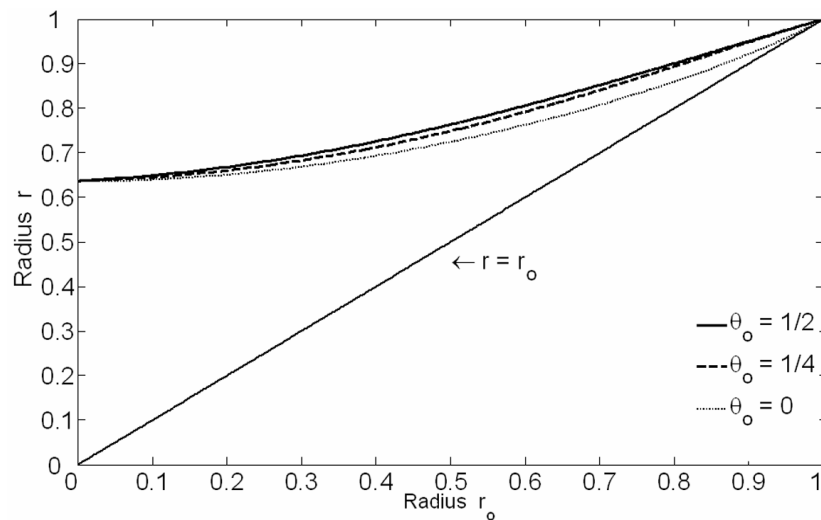


Figure 4.17. The radius of the zero of the MMSE predictive filter on single-pole analytic signals with different $\theta_0$.

### 4.7.2.3 Flat-spectral case of $r_0 = 0$

The analytic signal corresponding to a real white-spectral signal, such as impulse and white noise signals, can be modeled by (69) with $r_0 = 0$. Substituting $r_0 = 0$ into (71) yields $\cos(\pi - \theta) = \cos(\theta)$; thus $\tilde{\theta}$ should be $\pi/2$ or $3\pi/2$. Similarly, with $r_0 = 0$, solving (72) leads to $\tilde{r} = 2\sin(\theta)/\pi$. Since $\tilde{r}$ is nonnegative, the zero of the MMSE filter on the analytic signal positions at $(\tilde{r}, \tilde{\theta}) = (2/\pi, \pi/2)$, instead of the origin. Furthermore, the MMSE is $F(2/\pi, \pi/2) = \pi - 4/\pi$, and the estimated NSR is $(\pi - 4/\pi)/\pi \approx 0.594$ which is much lower than the excepted value 1. Figure 4.18 illustrates the first-order whitening processing on the analytic signals. In the absence of negative bands, all the whitened analytic signals have additional spectral hollows in positive bands.
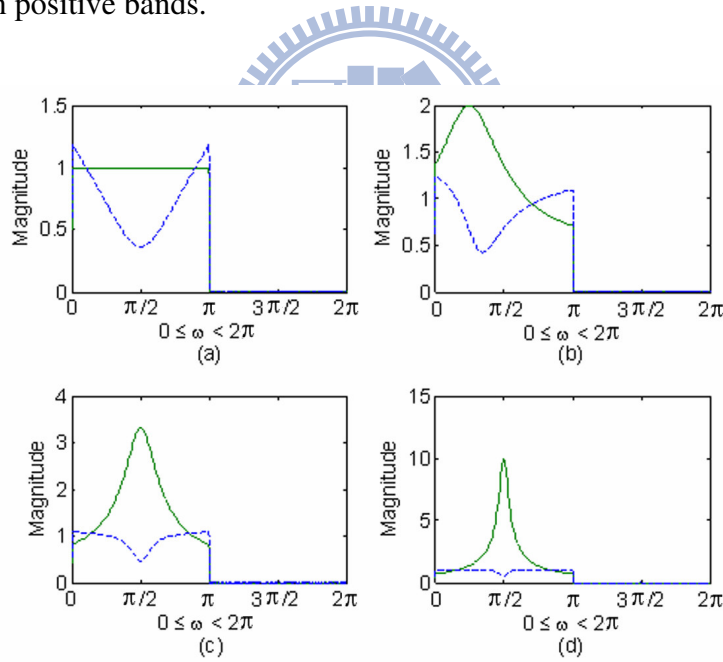


Figure 4.18.Whitening processing on analytic signals of first-order AR model by first-order LP. (a) flat-spectral analytic signal, (b)-(d) single-pole analytic signals with $(r, \theta) = (0.5, \pi/4)$, $(0.7, \pi/2)$ and $(0.9, \pi/2)$. The zero location $(r, \theta)$ of first-order whitening filter in (a)-(d) are $(0.6369, \pi/2)$, $(0.7720, 0.3363\pi)$, $(0.8594, \pi/2)$ and $(0.9510, \pi/2)$, respectively. (Solid line: the original signals, dashed line: the whitened signals; these simulations are implemented via 2048-point DFT.) For ensuring the orthogonality of the real and imaginary parts of the analytic signals simulated by DFT, the frequency response of the excitation signal at $\omega = 0$ and $\pi$ is 1/2, not 1.

### 4.7.2.4  Second-Order LP on Flat-Spectral Analytic Signals

The mean-square error function $F(r_1, r_2, \theta_1, \theta_2)$ of the second-order LP filter on the analytic signal corresponding to white-spectral signals is expressed as

$$\int_0^\pi \left|(1 - r_1 e^{j\theta_1} e^{-j\omega})(1 - r_2 e^{j\theta_2} e^{-j\omega})\right|^2 d\omega, \tag{80}$$

where the PSD of the analytic signal is assumed to be 1 for $0 < \omega < \pi$ and 0 for $-\pi < \omega < 0$. As shown in Appendix C.2, the radiuses and angles of zeros of the MMSE filter are given by

$$\tilde{r}_1 = \tilde{r}_2 = \frac{2}{\sqrt{\pi^2 - 4}} \approx 0.826, \tag{81}$$

$$\tilde{\theta}_1 = \arcsin\left(\frac{\pi}{2\sqrt{\pi^2 - 4}}\right) \approx 0.2245\pi \text{ and } \tilde{\theta}_2 \approx 0.7755\pi. \tag{82}$$

Also, the MMSE is $\pi(\pi^2 - 8)/(\pi^2 - 4) \approx 0.3185\pi$; the estimated NSR is about 0.317, which is lower than that evaluated by the first-order LP. Figure 4.19 shows the resultant spectral hollows on the flat-spectral analytic signal by the second-order LP.
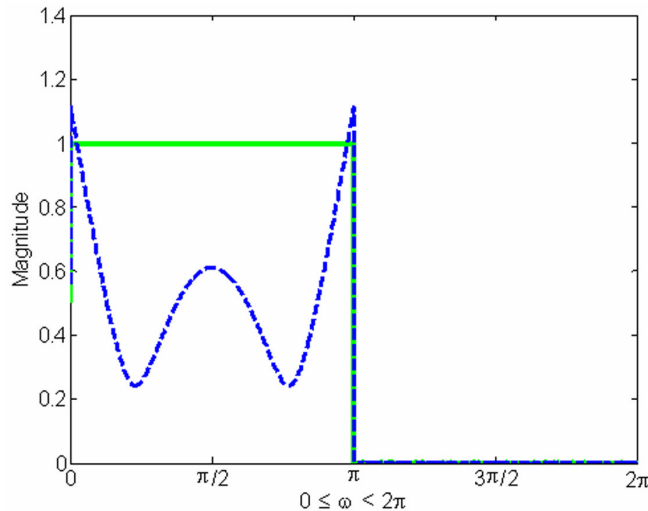


Figure 4.19. Whitening processing on the flat-spectral analytic signal by second-order LP. The estimated NSR value is 0.3181, and the two zeros position at $(r, \theta) = (0.8257, 0.2247\pi)$ and $(0.8257, 0.7753\pi)$. (Solid line: original signals, dashed line: whitened signals; the simulation is implemented via 2048-point DFT and covariance method.)

**4.7.2.5** Empirical Verification for SBR

The empirical example is conducted in Figure 4.20 for first-order and second-order LP by the covariance method. In the example, the original signal is a 32-point CEMFB subband signal of an impulse. The power spectrum of the input signal approximates the PSD of the white-spectral subband signal filtered by one modulated prototype filter and decimated by $M$. As can be seen, the spectral hollows are shaped on the whitened signals in the frequency domain.   For the first-order case in Figure 4.20 (a), the radius and angle of the zero of the LP filter are 0.5676 and $\pi/2$, and the estimated NSR value is 0.6778.   For the zeros of second-order LP filter in Figure 4.20 (b), their common radius is 0.6891 and their angles are $0.2078\pi$ and $0.7922\pi$; the estimated NSR value is 0.5249. Hence, in SBR, the estimated NSR for the white-spectral or noise-like signals will be underestimated by about 30 and 50 percent for the first-order and second-order LP, respectively. Through the above analysis on the ideal analytic signal model, we can also expect that the predictive bias becomes significant as the NSR of the predicted spectrum increases. This result is different from the intuition that the inverse filter should keep or slightly shape the spectrum of noise-like signals.



(a)                                             (b)
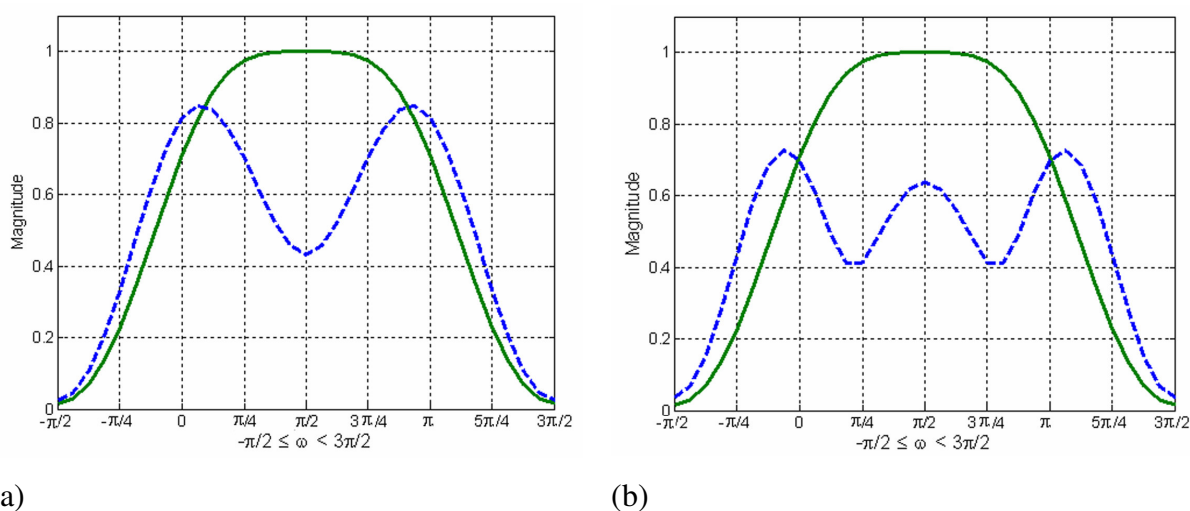
Figure 4.20. Whitening processing on a 32-point CEMFB subband signal of an impulse. (a) First-order LP (b) Second-order LP (Solid line depicts original signals; dashed line depicts whitened signals.)

### 4.7.3. Decimation-Whitening Filter

As shown above, the non-whiteness of the excitation noise components in analytic signals leads to the predictive bias. To remove the non-whiteness, the decimation by two should be included before applying the LP to the CEMFB subbands in SBR. The new approach has benefits in terms of the frequency resolution, NSR measure, analytic signal property maintaining, and computational complexity.

#### 4.7.3.1 The Decimation-Whitening Filter for SBR

The relation between the original analytic signal and the signal decimated by two is expressed in the frequency domain as

$$X_d(2\omega) = \tfrac{1}{2} X(\omega), \tag{83}$$

for either $0 < \omega < \pi$ or $-\pi < \omega < 0$, where $X$ and $X_d$ denote the Fourier transforms of the analytic and the decimated signals, respectively, and the range of $\omega$ depends on the absent side band of the analytic signal. Applying the second-order LP to the decimated signal can obtain two LP coefficients $a_1$ and $a_2$, and then the estimated PSD of the analytic signal is given as

$$P_X(\omega) = \frac{4\sigma_e^2}{\left|1 - a_1 e^{-j2\omega} - a_2 e^{-j4\omega}\right|^2}, \tag{84}$$

for either $0 < \omega < \pi$ or $-\pi < \omega < 0$, where $\sigma_e^2$ denotes the variance of the residuals. Consequently, for the analytic signal, the fourth-order LP filter derived from the second-order LP filter of the decimated signal can be given in the z-transform domain as

$$H(z) = 1 - a_1 z^{-2} - a_2 z^{-4}. \tag{85}$$

The design of the decimation LP filter is not new in AR modeling or maximum-entropy spectral estimation. In the literature, there have been researches of the advantages of the complex decimation LP filter over the real LP filter on the improvement of the sinusoidal

phase issues or neighboring frequency resolution. Especially, the expanding of the frequency scale by two can reduce the interference at one spectral peak caused by other neighboring frequency components, and hence a higher resolution of LP estimation can be achieved [58]. The decimation filter has been suggested [54]-[58]. However, these alternative complex filters require computational overhead when compared with the real ones in these scenarios. In SBR, the decimation-whitening filter not only has the advantages but also saves half the computational complexity to evaluate LP coefficients thanks to the data reduction from decimation.

### 4.7.3.2 Examples and Comparisons

According to the standard [5], the LP in SBR should be implemented via the second-order covariance method covering 32 samples for each CEMFB subband per audio frame. Figure 4.21 compares the original whitening method in SBR with the proposed method. In each subfigure, the 32-point DFT magnitude spectrums of the original CEMFB subband and the whitened ones by the original and the proposed methods are depicted in the decibel (dB) domain. As can be seen in Figure 4.21 (a) where the subband is generated from a real white noise, the proposed method slightly alters the original spectrum, while the original method not only alters the positive spectrum but also amplifies the negative spectrum. The evaluated NSR values in this case are 0.38 and 0.93, respectively, by the original and the proposed methods; the original method gives the poor NSR estimation. For the second instance illustrated in Figure 4.21 (b) where the subband contains a very strong sinusoid component, both methods have good whitening effect, but the proposed method results in a flatter whitened spectrum. In Figure 4.21 (c) where the original subband has three sinusoid components located in the frequency interval between 0 and $3\pi/2$, the original method slightly attenuates the largest one but amplifies the others. This phenomenon illustrates the interference among the components. In contrast, the proposed method destroys the largest one
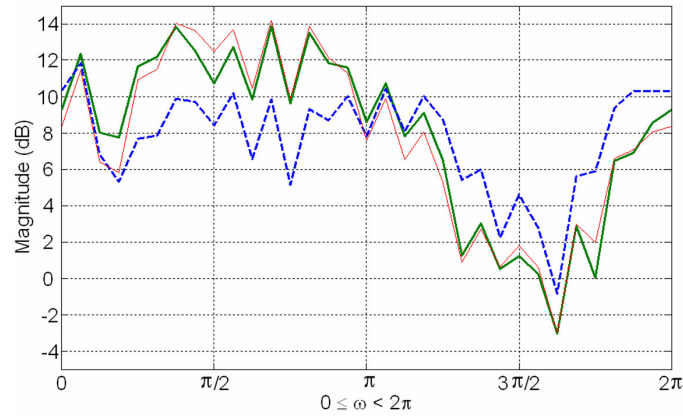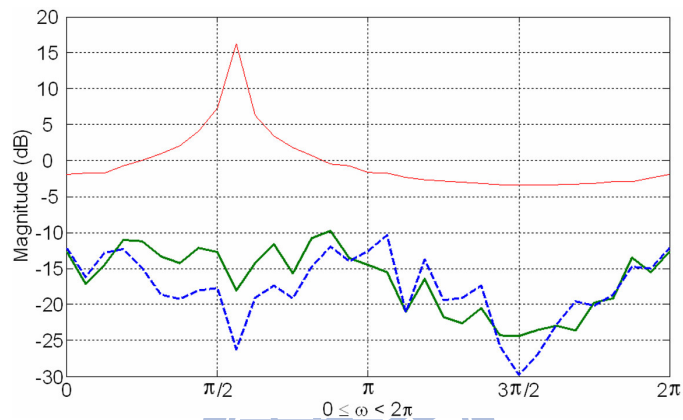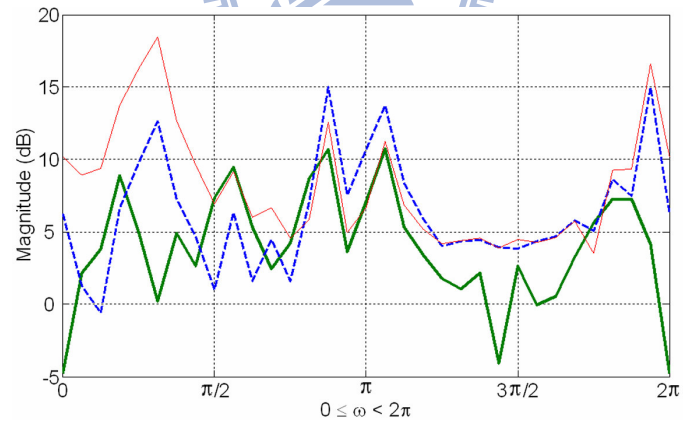
Figure 4.21. Whitening comparison for the original method and the proposed method. The magnitude spectra are evaluated through 32-point DFT; thin line depicts the original signals, thick line depicts the whitened signals by the proposed method, and dashed line depicts the whitened signals by the original method.
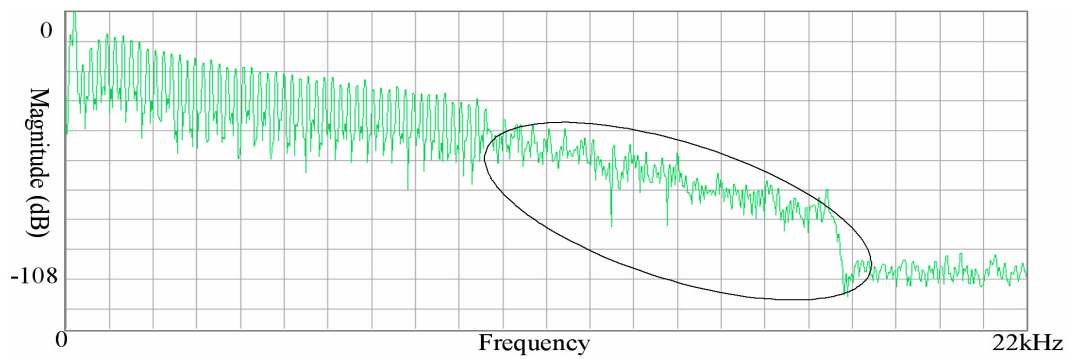
(a)
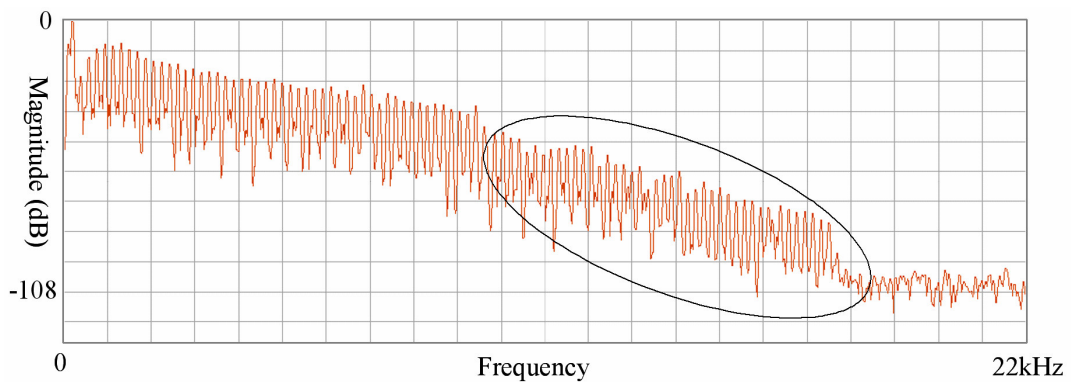
(b)
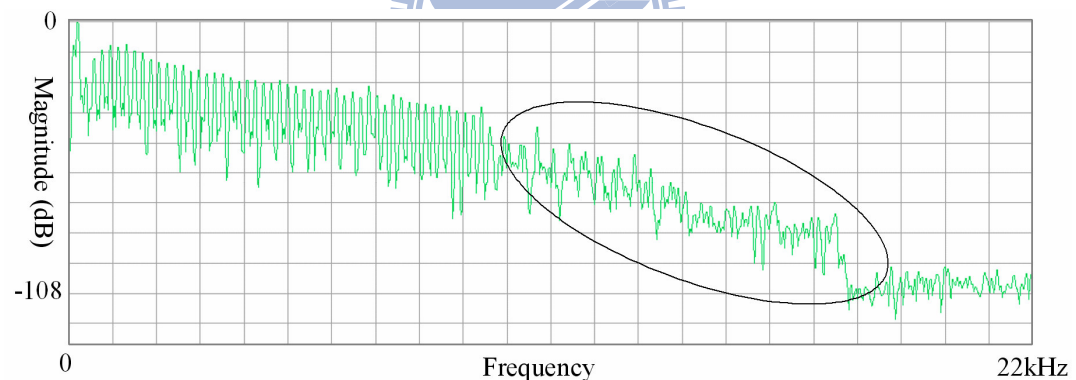
(c)

Figure 4.22. Whitening comparison for the original method and the proposed method. (a) The original DFT magnitude spectrum. (b) The decoded DFT magnitude spectrum with the original whitening filter. (c) The decoded DFT magnitude spectrum with the decimation-whitening filter. The spectra are depicted in dB domain. For both the filters, the chirp factor takes 1. Also, no additional noise is added, and the audio sampling rate is 44.1 kHz.

without amplifying the others thanks to the frequency scaling. Figure 4.22 illustrates another instance for the better whitening result of the proposed filter on the tonal-rich signal. In Figure 4.22 (b) and (c), the LF decoded AAC signal is filtered by the original filter and the proposed

filter respectively. Both chirp factor values for the filters are equal to 1, and no additional noise is added. From the HF spectra, we can see that the original filter cannot "whiten" the tonal structure, while the decimation-whitening filter does better.

Another noticeable feature is that the proposed method keeps better the energy than the original method. In the SBR encoder, the energy of HF is calculated and recorded based on the HF CEMFB subbands which have the good analytic-signal property. Subsequently, the SBR decoder adjusts the energy of the whitened LF subbands to fit the recorded HF energy. However, as noticed in the previous discussion, the original filter has more energy leakage due to the amplification in the negative side band. After filtered by the synthesis filterbank, these negative components will be filtered out and lead to an energy loss because these energies in the negative side bands have contributed to the energy estimation. The proposed filter has better control due to the less leakage from the negative frequency range. Figure 4.23 illustrates the better envelope by comparing the spectra of the two methods, where the chirp factors take 0.98 for all replicated subbands and no additional noise is added for HF. The original signal consists of the white noise and a single tone in LF.
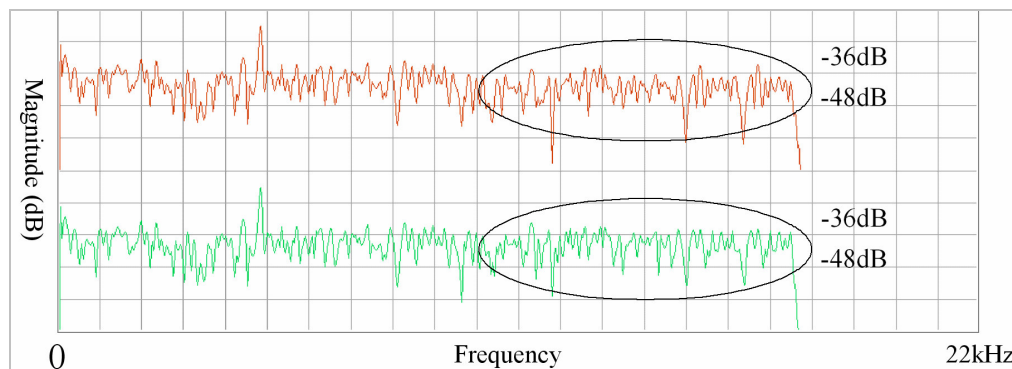


Figure 4.23. The energy loss effect of the original whitening method. The depicted spectra are the decoded spectra with the original method (the upper) and the proposed method (the below) respectively. For both the filters, the chirp factor takes 0.98. Also, no additional noise is added, and the audio sampling rate is 44.1 kHz. The HF envelope of the decoded spectrum with the proposed method fits −36dB, while that with the original method is under −36dB.

## 4.8. Concluding Remarks

In this chapter, we explored six new types of artifact in SBR which are very different from those in conventional frequency domain coders. The "tone trembling", "tone shift" and "beat" artifacts are mainly due to the duplication of spectral bands. Tonality control and interpolation mode are the main keys of handling the "noise overflow" and "tone spike" artifacts. The limited gain mechanism in SBR decode causes the "sawtooth" artifact. On the other hand, we also demonstrated the predictive bias of the second-order linear prediction in SBR. The predictive bias is due to the analytic property of the CEMFB in SBR. A decimation-whitening filter has been proposed to remove the bias.
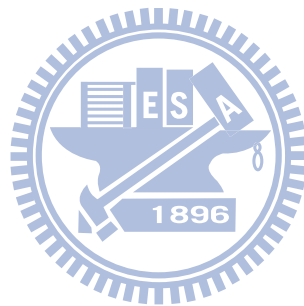
# CHAPTER 5
# ARTIFACTS IN
# PARAMETRIC STEREO CODING

The parametric stereo (PS) coding [10] has been unitized in the MPEG-4 audio parametric coding scheme for compressing high-quality stereo audio at the bit rates around 24–32 kbps. PS attempts to reconstruct a binaural signal from a monaural down-mix signal according to the parameters extracted by capturing the stereo sound image of an original binaural signal. In the down-mixing procedure, the loss of stereo sound images and the variability of mixing coefficients bring two obvious artifacts referred to as the "tone leakage" and the "tone modulation" artifacts.

## 5.1. Parametric Stereo Coding Overview

The PS coding utilizes four critical spatial cues, including inter-channel intensity difference (IID), intensity coherence (ICC), intensity phase difference (IPD) and overall phase differences (OPD) [16], to characterize lateralization and width of audio objects. As illustrated in Figure 5.1, through the auxiliary of these spatial cues, referred to as the stereo parameters, PS can merely encode a monaural signal down-mixed from an original binaural signal and reconstruct the space perception through the up-mixing processing. Consequently, most bits are saved thanks to the channel reduction. Figure 5.2 depicts the block diagram of PS in MPEG-4 HE-AAC V.2 encoder. Both the stereo parameter extraction and the down-mixing process in PS are performed on the complex-valued QMF bands that are analyzed by the 64-band analysis CEMFB and are further split through a hybrid analysis filterbank to increase the frequency resolution in the LF part. The LF and HF parts of the down-mix monaural signal are encoded by AAC and SBR, respectively.
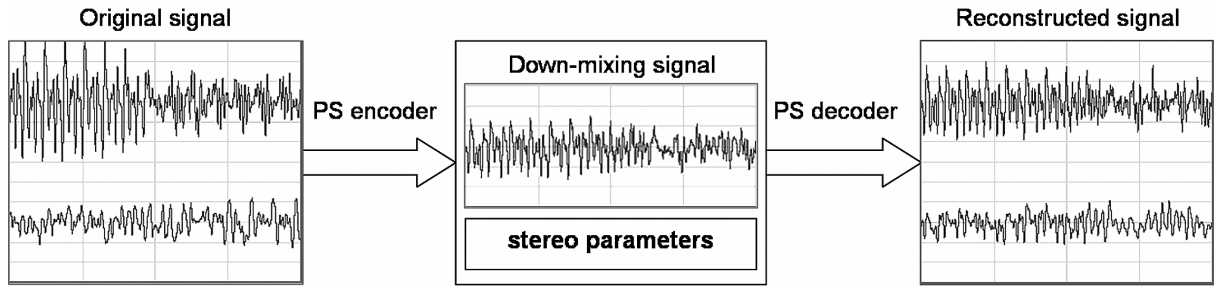
Figure 5.1. Illustration of the down-mixing monaural signal and the up-mixing binaural signal.
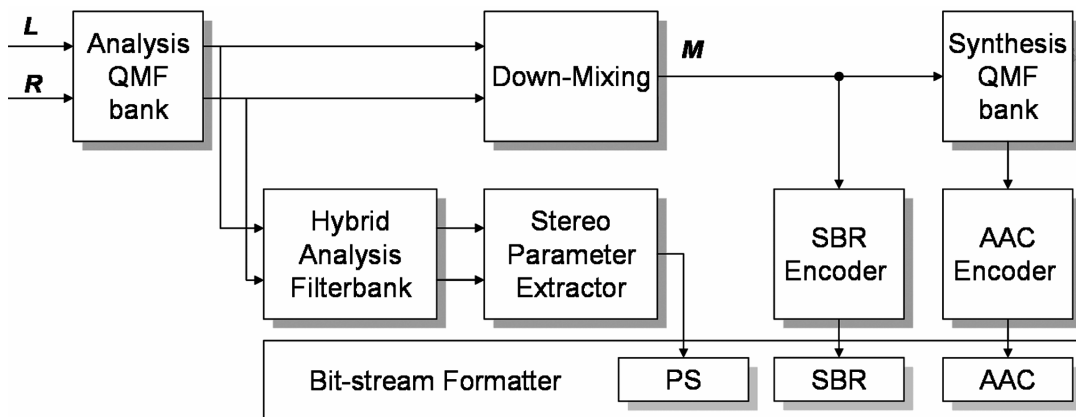


Figure 5.2. Diagram of PS in MPEG-4 HE-AAC version 2 encoder.
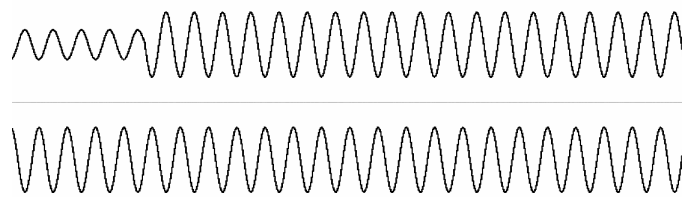


(a)
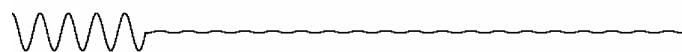


(b)

Figure 5.3. Signal vanishing effect of the average method: (a) original binaural signal; (b) extracted monaural signal by the average method.

(a)



(b)



(c)
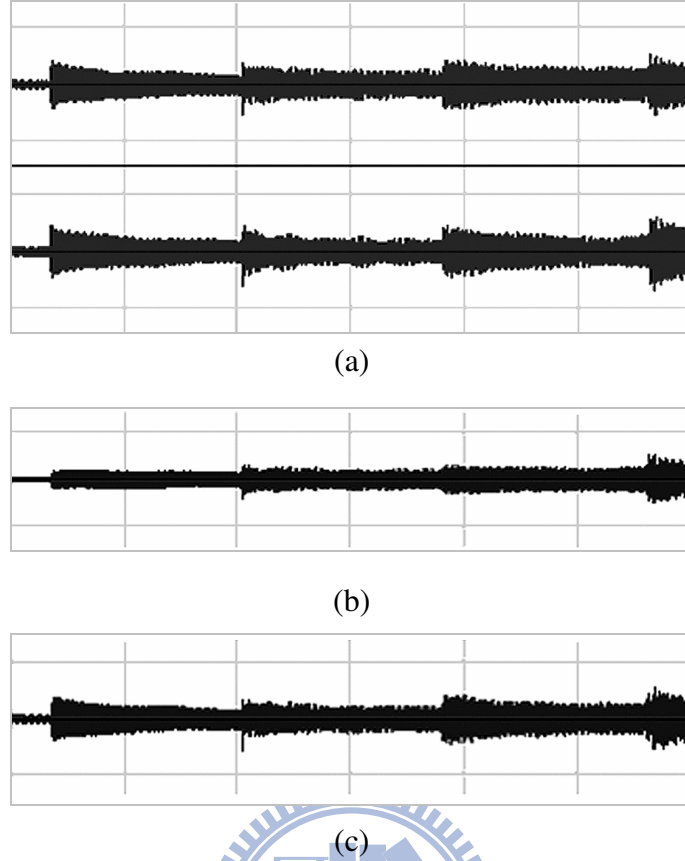
Figure 5.4. The advantage of energy conservation of the KLT method: (a) original binaural signal; (b) extracted monaural signal by the average method; (c) extracted monaural signal by the KLT method.

In the literature, the average and the KLT (Karhunen-Loève Transform) based methods are the most common down-mixing methods. Among the existing methods, the average method is the simplest down-mixing approach by averaging a binaural signal (i.e. $M = (L+R)/2$, for a stereo signal $L$ and $R$). As shown in Figure 5.3, the average method may result in serious signal vanishing due to phase cancellation. Even though the original left and right channels have similar temporal envelopes, their phase difference can cause waveform cancellation. Many recent researches have focused on other advanced methods, especially those based on the KLT, also known as the PCA (Principal Component Analysis) [17], [59]-[61]. In general, the down-mix $k$th subband signal $m_k(n)$ is expressed as

$$m_k(n) = \lambda_k^1 \cdot l_k(n) + \lambda_k^2 \cdot r_k(n),$$ (86)

where $\lambda_k^1$ and $\lambda_k^2$ are the (complex-valued) combination coefficients; $l_k(n)$ and $r_k(n)$ are the $k$th subbands of the left and right channels. The typical KLT-based method substitutes the combination coefficients by the orthonormal eigenvector corresponding to the largest eigenvalue of the cross-correlation matrix of the stereo subband [62]. Figure 5.4 compares the resultant envelopes of the down-mix signals by the two methods to the original envelopes and exhibits the advantage of energy conservation of the KLT-based method.

# 5.2. Artifacts in PS coding

The crosstalk of stereo images after the down-mixing process smears the space cues. Further, varying mixing coefficients leads to more artifacts. For instance, to achieve energy compactness, the KLT-based method bears more risks than the simple average method. Discarding weak signal components and varying combination coefficients are the major causes of artifacts under the KLT-based method.

## 5.2.1. Tone Leakage Artifact

The "tone leakage" artifact can be classified into two types. Type-I tone leakage artifact means that one tone in some channel leaks to another channel after the up-mixing process. Any down-mixing method has risks to suffer such a kind of artifact. Type-II tone leakage artifact means that some tone vanishes in a decoded signal. In PS, both the KLT-based and average down-mixing methods are susceptible to the two kinds of tone leakage artifact. However, the KLT-based method incurs type-II tone leakage artifact more easily than the average method due to discarding weak components.

Figure 5.5 illustrates the tone leakage artifacts under the average and KLT-based methods. In Figure 5.5 (a), the stereo signal has two tones in individual channels, which have slightly different frequencies and the magnitude difference of 12 dB. The down-mix signal

obtained by the average method retains the two tones that come from the distinct channels. In Figure 5.5 (b), the type-I tone leakage artifact occurs on the two tones. Although each channel maintains its own tone component, the additional tone is leaked to the other channel after the up-mixing process. On the other hand, to keep energy compactness, the KLT-based method trends to save the energy dominant channel. This implies that when two channels have a significant difference in energy, the weaker channel will be ignored and lose the spectral structure in the down-mix signal. As illustrated in Figure 5.5 (c), the decoded binaural signal keeps the stronger tone and suppresses the weaker one.



(a)

(b)

(c)
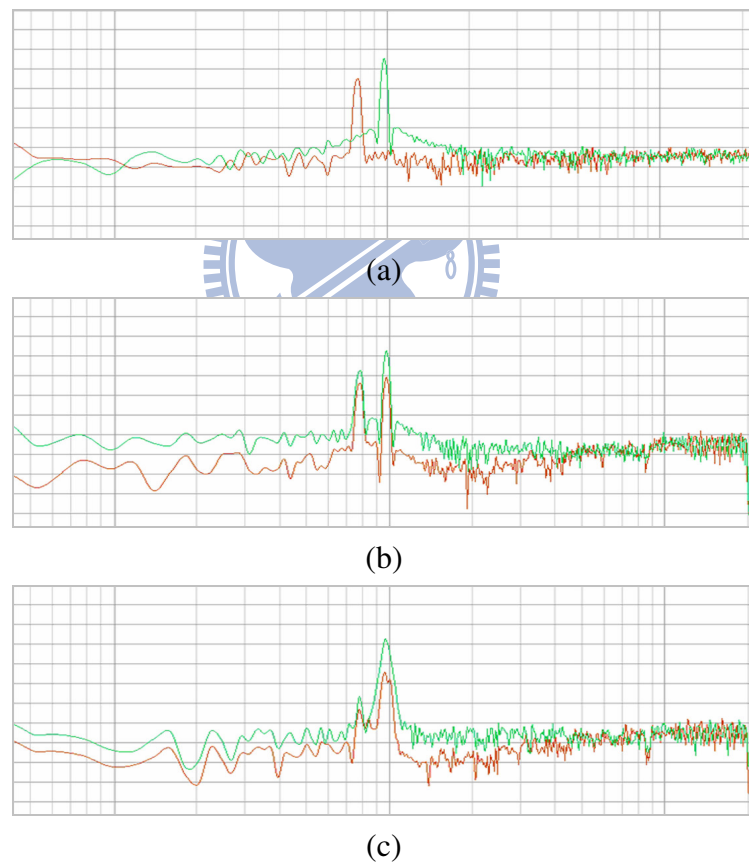
Figure 5.5. The illustration and the comparison of the tone leakage effect under the average method and the KLT method: (a) linear-scaled spectrum of the original stereo signal; (b) linear-scaled spectrum of the reconstructed stereo signal by the average method; (c) linear-scaled spectrum of the reconstructed stereo signal by the KLT method.

To summarize, both the average and KLT-based methods have risks to generate the type-I and type-II tone leakage artifacts. Due to the inherent property that the components in a down-mix signal are regenerated into the up-mix binaural signal, any down-mixing method suffers the type-I tone leakage artifact. On the other hand, although the KLT-based method can keep the dominant tones, the weaker channel is usually ignored due to the biased combination ratio. The tradeoff between the spectral component conservation and energy compactness is a major design issue for the down-mixing strategy.

## 5.2.2. Binaural Beat Artifact

Unlike the beat phenomenon where two tones with slightly different frequencies coexist in a channel, the "binaural beats" artifact [51] arises when two tones with slightly different frequencies occur in distinct channels. In this situation, listeners can hear a movement of sound image between their two ears, occurring at the rate that equals the frequency difference. In PS, the tone leakage artifact breaks down the binaural beats phenomenon. For instance, in Figure 5.6 (b), the type-I tone leakage artifact under the average down-mix method merges the tones in the distinct channels into the monaural signal, and hence the beat artifact is caused. This mergence makes the movement of sound image between ears disappear and generates an intensity fluctuation due to beats. The change from a binaural beat phenomenon to the beat artifact is called the "type-I binaural beat" artifact. In another case, as illustrated in Figure 5.6 (c), the type-II tone leakage artifact under the KLT-based method suppresses the weaker tone and makes the special space perception disappear. Such a phenomenon is called "type-II binaural beat" artifact. Figure 5.7 provides an example to show both type-I tone leakage and type-I binaural beat artifacts, where the original stereo signal has chirp sounds between 0 and 5 kHz increasingly and decreasingly in the left and right channels, respectively. In Figure 5.7 (b), the type-I tone leakage and the type-I binaural beat artifacts are introduced into the PS decoded signal; in Figure 5.7 (d), an obvious fluctuation occurs in the PS decoded

signal waveform due to the beat phenomenon.



(a)

(b)

(c)
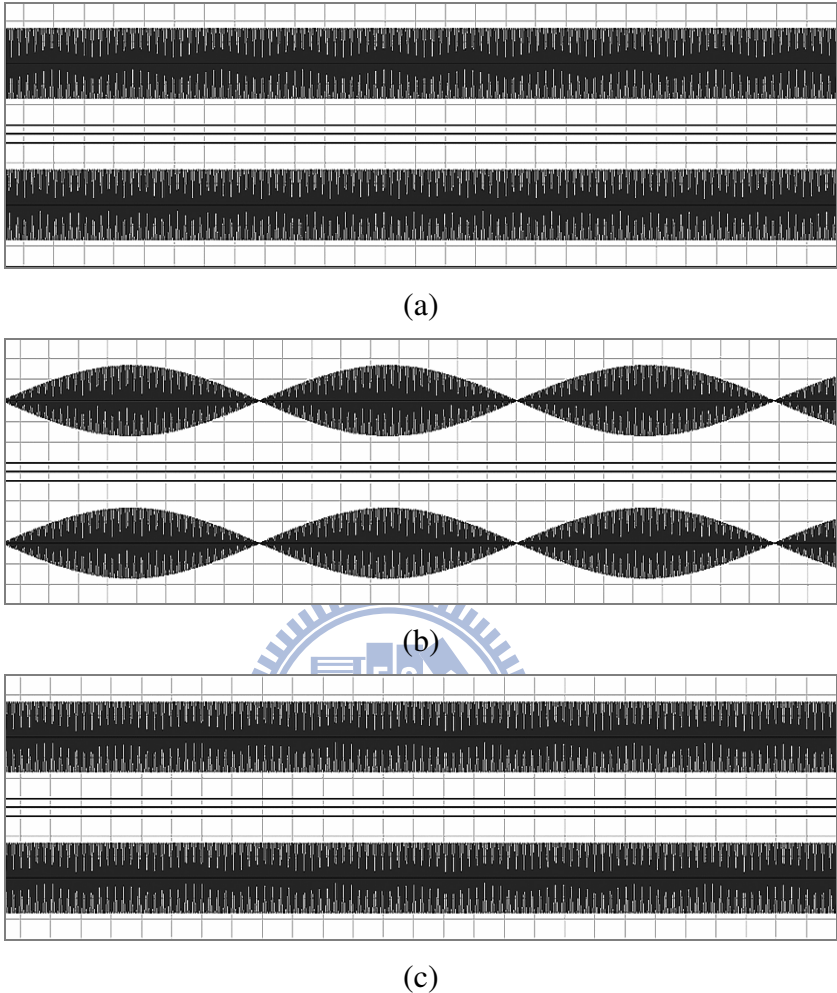
Figure 5.6. The degeneration of the binaural beat effect in PS coding: (a) original binaural signal with the binaural beat from the 200Hz and 201Hz tones; (b) binaural beat artifact in the decoded binaural signal by the average method; (c) elimination of the binaural beat in the decoded binaural signal by the KLT method.
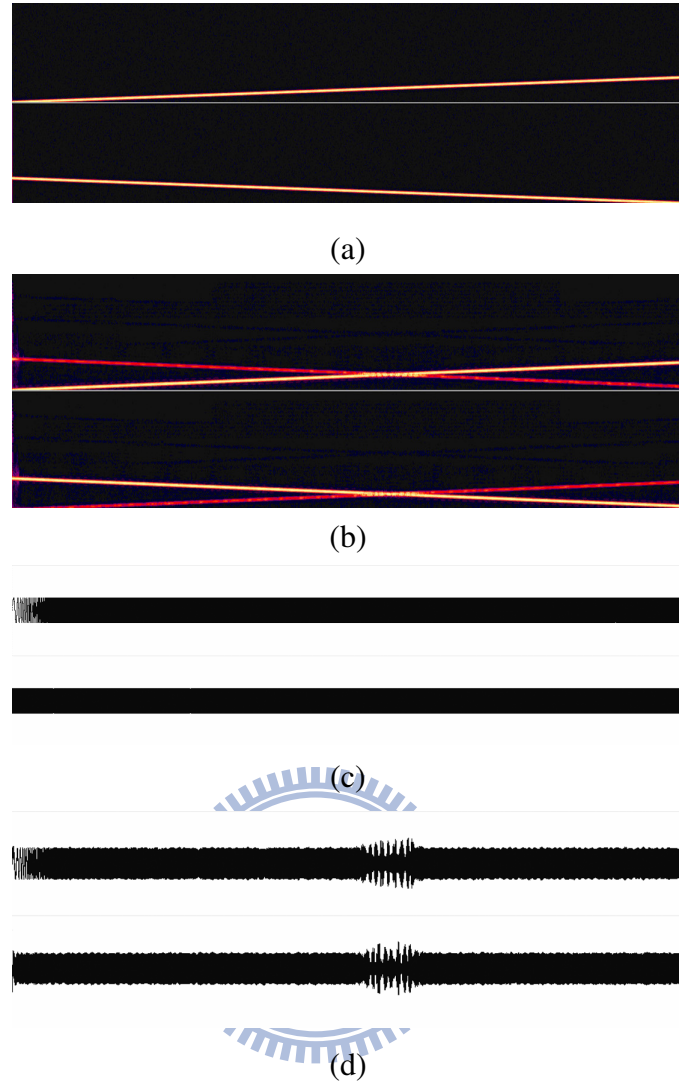
Figure 5.7. The type-I tone leakage and the type-I binaural beat artifacts in PS coding: (a) the original signal in spectrogram form; (b) the decoded signal with the two artifacts; (c) the waveform of (a); (d) the waveform of (b). In (a) and (b), the vertical coordination is the frequency range from 0 to 22 kHz and the horizontal coordination is the time with frames.

### 5.2.3. Tone Modulation Artifact

Although the KLT-based down-mixing method has the merit of optimal energy conservation, frame-by-frame varying coefficient vectors leads to connection discontinuities of down-mix spectra between adjacent frames and thus causes an artifact sounding like "click". Figure 5.8 exhibits a series of reconstructed spectra under the KLT-based method. The phenomenon that the spectral shape of tone expands and contracts is called the "tone

modulation" artifact. To analytically explain the artifact, we consider the effect of combination coefficients through the linear combination form of a down-mix subband signal:

$$d(n) = \lambda_1(n)\exp(i\theta_1(n)) \cdot l(n) + \lambda_2(n)\exp(i\theta_2(n))r(n), \qquad (87)$$

where $\lambda_k(n)\exp(i\theta_k(n))$ for $k = 1, 2$ means the polar form of the combination coefficients, and $l(n)$ and $r(n)$ are the left and right subband signals. The multiplier $\lambda_k(n)\exp(i\theta_k(n))$ in (87) is constant within a frame but may change abruptly at frame bounders. Let $s(n) = A\exp(i(\omega n + \Theta))$ be a sinusoid contained in the left channel and coupled into the down-mix subband signal. Then it is modulated in amplitude and phase as follows.

$$\hat{s}(n) = (A \cdot \lambda_1(n))\exp(i(\omega n + \Theta + \theta_1(n))). \qquad (88)$$

Therefore, a KLT-based down-mix signal can be regarded as a summation of two signals with mixed modulation in amplitude and phase and easily has the tone modulation artifact.

Like the PSOLA (Pitch Synchronous Overlap Add) method [63] for waveform synthesis in speech processing, a reduction method for the tone modulation artifact is to smooth combination coefficients to avoid spectral discontinuities in a down-mix signal. Let $\gamma_i$ and $\gamma_{i+1}$ denote the combination coefficients of one subband in the $i$th and $(i+1)$th frames. To smoothly connect two constant values, the coefficients from time index 1 to $k$ in the $(i+1)$th frame is interpolated as a cosine curve (see Figure 5.9):

$$\tfrac{1}{2}(\gamma_i - \gamma_{i+1}) \cdot \cos(\pi n/k) + \tfrac{1}{2}(\gamma_i + \gamma_{i+1}). \qquad (89)$$

The reduction method can reduce the "click" noise caused by the tone modulation artifact [61].
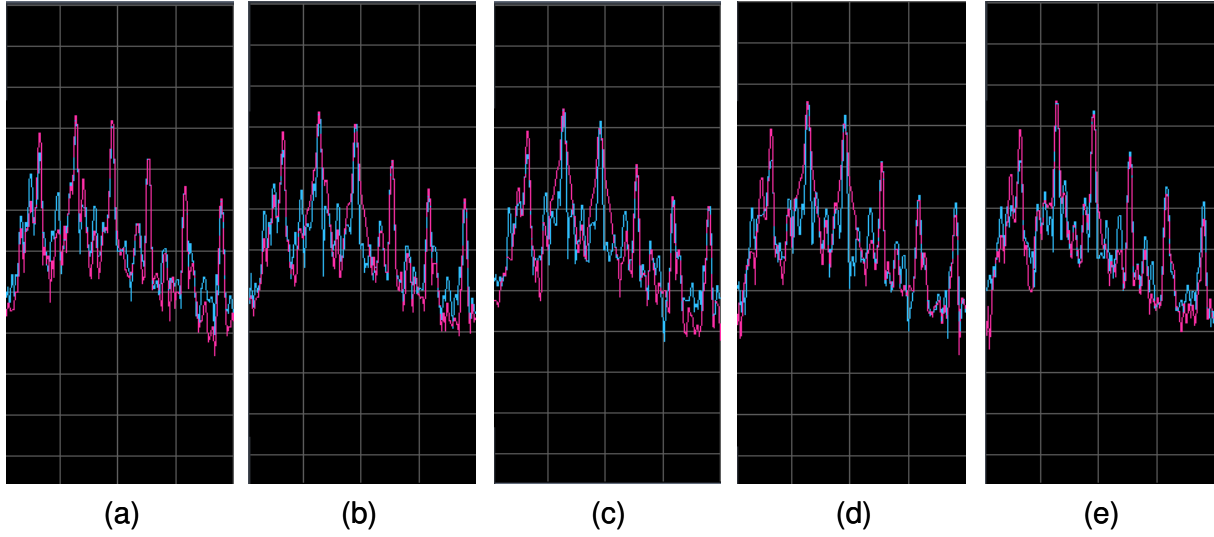
Figure 5.8. Example of tone modulation effect (the original spectrum has stable and fine tones).
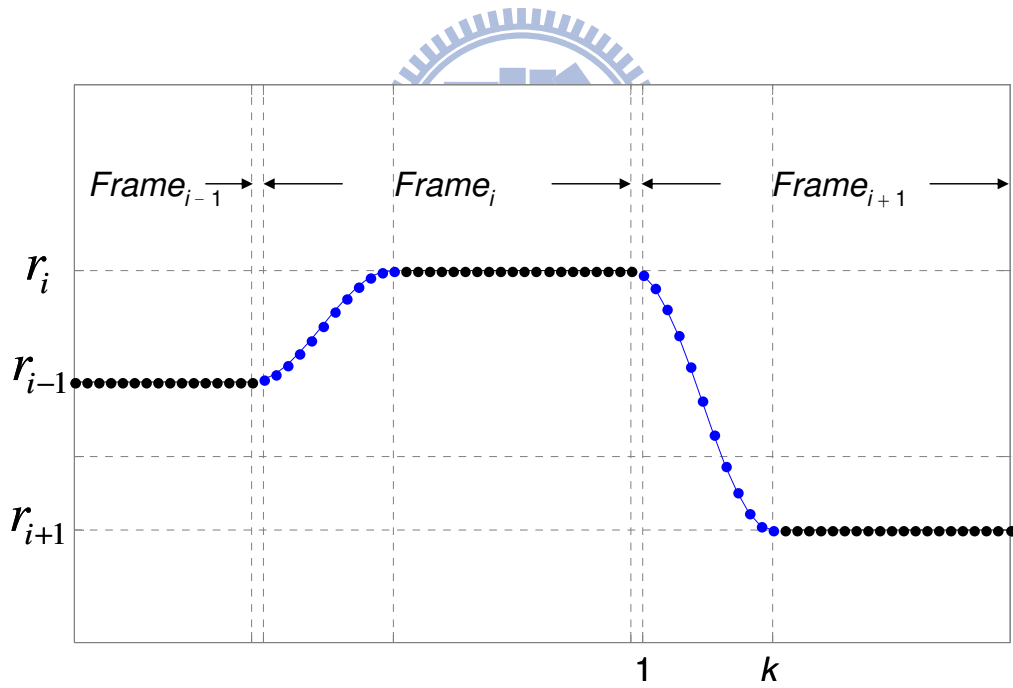


Figure 5.9. Cosine smooth connection of coefficients between frames.

## 5.3.Concluding Remarks

The cross-talk effect is an inherent artifact in the down-mix based audio coding. According to the average and KLT based approaches, we considered the "type-I tone leakage" and "type-II tone leakage" artifacts to indicate two different cross-talk phenomena. The two artifacts can break down the "binaural beat" effect into the "type-I binaural beat" and "type-II binaural beat" artifacts. We also concerned the spectral modulation effect due to varying down-mix coefficients and proposed a coefficient smooth scheme to reduce the "tone modulation" artifact.

# CHAPTER 6
# CONCLUSION

This dissertation has investigated the audible artifacts in the state-of-the-art perceptual audio codecs. We have modeled the audible artifacts through the time-frequency diagrams; considered the artifacts-susceptible music types; and analyzed the critical encoding technologies incurring these artifacts and summarized these artifacts in Table 6.1. We began from the two common artifacts in most perceptual audio codecs, the "band-limited" and "birdie" artifacts. The characteristic of the two artifacts shown up in spectra are the spectral clipping and spectral valley which lead to the "muffled" audio and "fishy" sound, respectively. On the other hand, for handling the tradeoff between the parallelism and the numerical distortion of cosine modulated filterbanks, a fast algorithm for computing DCT-IV of composite lengths has been proposed. We next considered the TNS in AAC. The compact forms for the TNS fundamental were established through the AR modeling theory in DTTs. Based on the developed compact forms, we have revisited the well-known "time-domain aliasing" noise through the relationship between MDCT and DCT-IV. A reduction method combining TNS and window switch was proposed to reduce the time-domain aliasing noise in AAC. Furthermore, both the temporal Hilbert-envelope method used in the standard and the power-envelope method were compared. Subsequently, six new artifacts in SBR have been introduced. The "tone trembling" artifact originating from constant changes in replicated sources generates a "billow-like" spectrogram. The "tone shift" artifact that is a common artifact for tone-rich signal indicates the obvious offsets between the recreated and original tones. The "noise overflow" and the "tonal spike" phenomena, which originate from inaccurate tonality matching, generate annoying "rasping" and "metallic" sounds, respectively. The "sawtooth" artifact due to the limitation of the upper bound of scaling gain is brought

about by the protection mechanism "limiter gain" in SBR. Furthermore, because of the inaccurate position of the patched or compensated tone, the risk of the "beat" artifact needs to be concerned. On the other hand, we have demonstrated the predictive bias from the whitening filter in SBR. The bias increases the interference of the noise component to the sinusoid component in LP and leads to the spectral hollows in noise-like subbands. A novel filter, named the decimation-whitening filter, has been proposed for removal of the bias. The new filter provides advantages in terms of NSR measure, frequency resolution, energy leakage, and computational complexity for SBR. Finally, the loss of stereo image due to down-mixing has been considered for the PS coding. The "type-I tone leakage" artifact means that one tone in some channel leaks to another channel after up-mixing process. In contrast, the "type-II tone leakage" artifact means that the tone vanishes in the decoded signals. An example of the loss of space perception in PS is the degeneration of the "binaural beat" to the beat artifact, named "type-I binaural beat" artifact, or the disappearance of the "binaural beat", named "type-II binaural beat" artifact. Table 6.1 lists these artifacts in terms of the perception, the generation source, the time/frequency feature, the music types, the typical tracks and the existing relief methods.

Table 6.1.

Summary of Compression Artifacts

| ARTIFACTS | PERCEPTION | GENERATION SOURCES | TIME/ FREQ. FEATURES | MUSIC TYPES | TYPICAL TRACKS | RELIEF METHODS |
|---|---|---|---|---|---|---|
| **Birdie** | Fishy | (1) Unsuitable bit allocation policies (2) Excessive masking energy estimation | Zero bands | Wideband signal with relative small spectral component | velvet in Figure 2.1 | Zero band dither [37][38] |
| **Band-Limited** | Muffled | (1) Sampling rate reduction (2) Bit rate constraint | HF range | HF-rich signal | sc03 in Figure 2.2 | High frequency reconstruction [37][38] |
| **Pre-echo** | Annoying | (1) Transient signal (2) Inappropriate size of coding block | Temporal precedence around attack | Transient signal | si02 | (1) Window switch (2) TNS (3) Gain control (4) Bit reservoir (5) Pre-echo control |
| **Time-domain Aliasing** | Annoying | (1) Time-domain aliasing of MDCT (2) Shaping of TNS filter | Before or after the attack | Transient signal | si02 in Figure 3.9 and Figure 3.10 | A joint method by TNS and window switch [33] |
| **Aliasing Noise by High-Order TNS** | Annoying | High-order prediction filter in TNS | Before or after the attack | Transient signal | si02 in Figure 3.11 | |
| **Tone Trembling** | Trembling | (1) Tone-rich signal in SBR (2) Adaptive frequency table and SBR range in SBR | Discontinuous spectrogram | Tonal signal | si03 in Figure 4.5 | Fixed table and Fixed SBR range |
| **Tone Shift** | Not Sensitive | (1) Harmonic signal in SBR (2) Band replication in SBR | Tones with frequency offset in SBR range | Harmonic signal | si03 in Figure 4.6 | |
| **Noise Overflow** | Dull | (1) Tone losing in T/F grid in SBR (2) Envelope adjustment at interpolation mode in SBR | Noise replacing for losing tones | Tonal signal | sm02 in Figure 4.7 and Figure 4.9 | Non-interpolation mode |
| **Tonal Spike** | Metallic | (1) False alarm of tone detection in SBR (2) Overestimation of tonal component in SBR | Tone replacing for noise | Tonal signal | sm02 in Figure 4.12 | |
| **Sawtooth** | Depend on energy | Limiter gain mechanism in SBR | Sawtooth spectral envelope in SBR range | Signal with slant spectral envelope | sc01 in Figure 4.13 | Limiter gain turns off |
| **Tone Leakage Type-1** | Blurred spatial position | Down-mixing procedure in PS | Any range | Tonal binaural signal | Artificial signal in Figure 5.5 | |
| **Tone Leakage Type-2** | Blurred spatial position | Down-mixing procedure by the KLT in PS | Any range | Tonal binaural signal | Artificial signal in Figure 5.5 | |
| **Tone Modulation** | Click | Down-mixing procedure by the KLT in PS | Any range | Tonal binaural signal | sc01 in Figure 5.5 | Coefficient smooth |
| **Beat** | Intensity fluctuation | Patch procedure in SBR | LF range in SBR | The two tones of slightly different frequencies in the same channel. | Artificial signal in Figure 4.14 | |
| **Binaural Beat Type-1** | Degeneration to beat effect | (1) Binaural beat effect in original stereo signal (2) Tone Leakage Type-1 | LF range | The two tones of slightly different frequencies in different channels. | Artificial signal in Figure 5.6(b) | |
| **Binaural Beat Type-1I** | Space perception elimination | (1) Binaural beat effect in original stereo signal (2) Tone Leakage Type-II | LF range | The two tones of slightly different frequencies in different channels. | Artificial signal in Figure 5.6 (c) | |

# APPENDIX A

# COMPUTATIONAL COMPLEXITY AND FINE

# TURNING FOR FAST RADIX-Q AND

# MIXED-RADIX ALGORITHMS

## A.1.    Computational Complexity of Fast Radix-$q$ Algorithm

For $k = 0, 1,…, N/q − 1$, the arithmetic costs for the radix-$q$ SDCT-IV computation are listed as follows:

(1) $q(q − 1)/2$ multiplications in (13) and (14).      (2) $q − 1$ multiplications in (15).

(3) $(q − 1)^2/2$ additions in (13) and (14).      (4) $q − 1$ additions in (15).

(5) $q − 1$ additions in (5) and (7).      (6) $q − 1$ additions in (17).

Totally, the numbers of multiplications and additions required by the radix-$q$ algorithm for SDCT-IV computation of length $N$ are

$$M_{S\text{-}IV}(N) = q \cdot M_{S\text{-}IV}(N/q) + (q − 1)(q + 2)/2 \cdot N/q, \tag{A.1}$$

$$A_{S\text{-}IV}(N) = q \cdot A_{S\text{-}IV}(N/q) + (q − 1)(q + 5)/2 \cdot N/q. \tag{A.2}$$

For DCT-IV computation, additional $N/q$ multiplications in (18) are required; hence, the numbers of multiplications and additions are respectively

$$M_{IV}(N) = M_{S\text{-}IV}(N) + N/q, \tag{A.3}$$

$$A_{IV}(N) = A_{S\text{-}IV}(N). \tag{A.4}$$

## A.2.    Radix-3 Algorithm

As $q = 3$ and $p = 1$, one multiplication is saved for a trivial factor $\cos(\pi/3) = 0.5$ in (13). Also, if $N$ is odd and $k^* = (N/3\text{-}1)/2$, it implies $\Theta_{0,k}^{N} = \pi/6$ and

$$Y_{k^*} = \left(A_{k^*} + \tfrac{1}{2} S^0_{k^*}\right) + \tfrac{\sqrt{3}}{2} C^0_{k^*}, \tag{A.5}$$

$$Y_{\frac{2N}{3}+k^*} = -\left(A_{k^*} + \tfrac{1}{2} S^0_{k^*}\right) + \tfrac{\sqrt{3}}{2} C^0_{k^*}, \tag{A.6}$$

$$Y_{\frac{2N}{3}-1-k^*} = S^0_{k^*} - A_{k^*}. \tag{A.7}$$

Equations (A.5)-(A.7) require one multiplication and four additions; thus, three multiplications and two additions are saved. Hence, from (A.1) and (A.2), the nontrivial arithmetic costs required for SDCT-IV computation are

$$M_{S\text{-}IV}(N) = 3 \cdot M_{S\text{-}IV}(N/3) + 4N/3\text{-}3,\ N > 1, \tag{A.8}$$

$$A_{S\text{-}IV}(N) = 3 \cdot A_{S\text{-}IV}(N/3) + 8N/3\text{-}2,\ N > 1, \tag{A.9}$$

where the initial values are $M_{S\text{-}IV}(1) = A_{S\text{-}IV}(1) = 0$. Hence, the corresponding DCT-IV multiplicative complexity is

$$M_{IV}(N) = M_{S\text{-}IV}(N) + N/3 + 1,\ N > 1, \tag{A.10}$$

where the number of scaling multiplications is two for (A.5) and (A.7) instead of one.

## A.3.　　Radix-5 Algorithm

As $q{=}5$, applying $\cos 4\pi/5 + 1/2 = -\cos 2\pi/5$ to (13) for $p = 1$ and 2 gives

$$U^1_k = -A_k + \tfrac{1}{2} B^0_k + (B^0_k - B^1_k)\cos\tfrac{2\pi}{5}, \tag{A.11}$$

$$U^2_k = A_k - \tfrac{1}{2} B^1_k + (B^0_k - B^1_k)\cos\tfrac{2\pi}{5}, \tag{A.12}$$

where $B^m_k = \left(C^m_k \cos\Theta^N_{m,k} + S^m_k \sin\Theta^N_{m,k}\right)$ for $m = 0, 1$. Equations (A.11) and (A.12) require one multiplication and five additions instead of four multiplications and four additions; thus, three multiplications are saved but one more addition is required. Hence, according to (A.1) and (A.2), the nontrivial arithmetic costs required for SDCT-IV are

$$M_{S\text{-}IV}(N) = 5 \cdot M_{S\text{-}IV}(N/5) + 11N/5,\ N > 1, \tag{A.13}$$

$$A_{S\text{-}IV}(N) = 5 \cdot A_{S\text{-}IV}(N/5) + 21N/5,\ N > 1. \tag{A.14}$$

Thus, the corresponding DCT-IV multiplicative complexity is

$$M_{IV}(N) = M_{S\text{-}IV}(N) + N/5, \ N > 1, \tag{A.15}$$

where the scaling factor $\delta$ can be absorbed into $B_k^m$ as

$$B_k'^m = \left(C_k^m \cdot \delta \cos \Theta_{m,k}^N + S_k^m \cdot \delta \sin \Theta_{m,k}^N\right). \tag{A.16}$$

For the initial case $N = 5$, using $\sin\pi/10 = \cos2\pi/5$ and $\cos\pi/10 = \sin2\pi/5$ in (14) gives

$$V_0^1 = (C_0^0 - S_0^0 \cot \tfrac{\pi}{5})\sin^2 \tfrac{\pi}{5} - (C_0^1 \cot \tfrac{2\pi}{5} - S_0^1)\sin^2 \tfrac{2\pi}{5}, \tag{A.17}$$

$$V_0^2 = [(C_0^0 - S_0^0 \cot \tfrac{\pi}{5}) - (C_0^1 \cot \tfrac{2\pi}{5} - S_0^1)]\sin \tfrac{\pi}{5} \sin \tfrac{2\pi}{5}. \tag{A.18}$$

# A.4.　　Radix-9 Algorithm

For $q = 9$, applying the relations $\cos\pi/9 = \cos4\pi/9 + \cos2\pi/9$ and $\sin\pi/9 = \sin4\pi/9$ - $\sin2\pi/9$ to (13) and (14) for each $p$ gives

$$U_k^0 = (A_k + B_k^1) + (B_k^0 + B_k^2 + B_k^3), \tag{A.19}$$

$$U_k^3 = -(A_k + B_k^1) + \tfrac{1}{2}(B_k^0 + B_k^2 + B_k^3), \tag{A.20}$$

$$U_k^2 = (A_k - \tfrac{1}{2}B_k^1) + (B_k^0 - B_k^2)\cos \tfrac{\pi}{9} - (B_k^0 - B_k^3)\cos \tfrac{4\pi}{9}, \tag{A.21}$$

$$U_k^4 = (A_k - \tfrac{1}{2}B_k^1) - (B_k^0 - B_k^2)\cos \tfrac{2\pi}{9} + (B_k^0 - B_k^3)\cos \tfrac{\pi}{9}, \tag{A.22}$$

$$U_k^1 = (-A_k + \tfrac{1}{2}B_k^1) + (B_k^0 - B_k^2)\cos \tfrac{4\pi}{9} + (B_k^0 - B_k^3)\cos \tfrac{2\pi}{9}, \tag{A.23}$$

$$V_k^1 = E_k^1 + (E_k^0 + E_k^2)\sin \tfrac{\pi}{9} + (E_k^2 + E_k^3)\sin \tfrac{2\pi}{9}, \tag{A.24}$$

$$V_k^2 = E_k^1 + (E_k^0 + E_k^2)\sin \tfrac{2\pi}{9} - (E_k^2 + E_k^3)\sin \tfrac{4\pi}{9}, \tag{A.25}$$

$$V_k^4 = -E_k^1 + (E_k^0 + E_k^2)\sin \tfrac{4\pi}{9} - (E_k^2 + E_k^3)\sin \tfrac{\pi}{9}, \tag{A.26}$$

$$V_k^3 = \tfrac{\sqrt{3}}{2}(E_k^0 - E_k^2 + E_k^3), \tag{A.27}$$

where we define

$$B_k^m = C_k^m \cos \Theta_{m,k}^N + S_k^m \sin \Theta_{m,k}^N, \ m = 0, 1, 2, 3, \tag{A.28}$$

$$E_k^m = C_k^m \sin \Theta_{m,k}^N - S_k^m \cos \Theta_{m,k}^N, \ m = 0, 2, 3, \tag{A.29}$$

$$E_k^1 = H_k^1 \cdot (\Lambda_k^1 \sin \tfrac{\pi}{3}), \ \text{for } k = 0, 1, \dots, N/9\text{-}1. \tag{A.30}$$

Equations (A.19) -(A.27) can be computed efficiently as follows. The last terms in (A.23) and (A.26) can be obtained from the sum of the last term in (A.21) and (A.22), and in (A.24) and (A.25), respectively. Also, using algebraic identities $ax+by = b(x+y) + (a-b)x$ and $bx+cy = b(x+y) + (c-b)y$, the pairs $ax+by$ and $bx+cy$ require three multiplications and three additions by sharing the common part $b(x+y)$. Hence, equations (A.19)-(A.30) require only 20 multiplications and 37 additions for each $k$. Furthermore, if $N$ is odd, it implies that $\Theta_{1,k}^{N} = \pi/6$ as $k^{*} = (N/9-1)/2$ and $m =1$, and thus (A.28) and (A.30) can be computed by

$$B_{k^*}^1 = \tfrac{\sqrt{3}}{2} C_{k^*}^1 + \tfrac{1}{2} S_{k^*}^1, \tag{A.31}$$

$$E_{k^*}^1 = \tfrac{1}{2} (\tfrac{\sqrt{3}}{2} C_{k^*}^1) - \tfrac{1}{4} (2 S_{k^*}^1 + S_{k^*}^1), \tag{A.32}$$

which require only one multiplication and three additions. Hence, three multiplications are saved, but one addition is wasted. On the other hand, 16 additions used in (5), (7) and (17) should be counted. For the scaling operations of DCT-IV, it requires one more multiplication in the following way.

$$\delta B_{k^*}^1 = \delta \tfrac{\sqrt{3}}{2} C_{k^*}^1 + \tfrac{1}{2} \delta S_{k^*}^1, \tag{A.33}$$

$$\delta E_{k^*}^1 = \tfrac{1}{2} (\delta \tfrac{\sqrt{3}}{2} C_{k^*}^1) - \tfrac{1}{4} (2 \delta S_{k^*}^1 + \delta S_{k^*}^1). \tag{A.34}$$

In summary, the nontrivial arithmetic costs required for the SDCT-IV are

$$M_{S\text{-}IV}(N) = 9 \cdot M_{S\text{-}IV}(N/9) + 20N/9 - 3, N > 9, \tag{A.35}$$

$$A_{S\text{-}IV}(N) = 9 \cdot A_{S\text{-}IV}(N/9) + 53N/9 + 1, N > 9. \tag{A.36}$$

The initial cases are $M_{S\text{-}IV}(9) = 12$ and $A_{S\text{-}IV}(9) = 40$ that are derived from the radix-3 algorithm. Thus, the corresponding DCT-IV multiplicative complexity is

$$M_{IV}(N) = M_{S\text{-}IV}(N) + N/9 + 1, N > 9, \tag{A.37}$$

with $M_{IV}(9) = 16$ that are derived from the radix-3 algorithm.

## A.5. Radix-2 DCT-II/DCT-IV Algorithm

Let the length $N$ be even. The radix-2 DCT-II/DCT-IV algorithm is represented as

$$\boldsymbol{C}_N^{II} = \boldsymbol{P}_N \begin{bmatrix} \boldsymbol{C}_{N/2}^{II} & \boldsymbol{0} \\ \boldsymbol{0} & \boldsymbol{J}_{N/2}\boldsymbol{C}_{N/2}^{IV}\boldsymbol{J}_{N/2} \end{bmatrix} \begin{bmatrix} \boldsymbol{I}_{N/2} & \boldsymbol{J}_{N/2} \\ \boldsymbol{J}_{N/2} & -\boldsymbol{I}_{N/2} \end{bmatrix}, \tag{A.38}$$

$$\boldsymbol{C}_N^{IV} = \boldsymbol{R}_N \begin{bmatrix} 1 & & & \\ & \boldsymbol{I}_{N/2-1} & & -\boldsymbol{J}_{N/2-1} \\ & & -1 & \\ & -\boldsymbol{J}_{N/2-1} & & -\boldsymbol{I}_{N/2-1} \end{bmatrix} \begin{bmatrix} \boldsymbol{C}_{N/2}^{II}\boldsymbol{J}_{N/2} & \boldsymbol{0} \\ \boldsymbol{0} & \boldsymbol{C}_{N/2}^{II}\boldsymbol{D}_{N/2} \end{bmatrix} \boldsymbol{G}_N \begin{bmatrix} \boldsymbol{J}_{N/2} & \boldsymbol{0} \\ \boldsymbol{0} & -\boldsymbol{J}_{N/2} \end{bmatrix}, \tag{A.39}$$

where matrices $\boldsymbol{I}_N$ and $\boldsymbol{J}_N$ denote the identity and anti-identity matrices respectively, and diagonal matrix $\boldsymbol{D}_N$ is defined by $diag\{(-1)^n \mid n = 0, 1,\ldots, N-1\}$. The Givens rotation matrix $\boldsymbol{G}_N$ is defined by $\boldsymbol{A}_N + \boldsymbol{B}_N$, where diagonal matrix $\boldsymbol{A}_N$ and anti-diagonal matrix $\boldsymbol{B}_N$ are defined by $a_{n,n} = \cos(\pi(N-1-2n)/4N)$ and $b_{n,N-1-n} = -\sin(\pi(N-1-2n)/4N)$, for $n = 0, 1,\ldots, N-1$. For a data vector $\boldsymbol{x} = [x_0, x_1,\ldots, x_{N-1}]^T$, the two permutation matrices $\boldsymbol{P}_N$ and $\boldsymbol{R}_N$ are defined by $\boldsymbol{P}_N\boldsymbol{x} = [x_0, x_{N-1}, x_2, x_{N-3}, x_4,\ldots, x_{N-4}, x_3, x_{N-2}, x_1]^T$ and $\boldsymbol{R}_N\boldsymbol{x} = [x_0, x_2, x_4,\ldots, x_{N-2}, -x_{N-1},\ldots, -x_5, -x_3, -x_1]^T$. The complexity functions for the radix-2 DCT-II/DCT-IV algorithm are given in the recursive form:

$$M_{II}(N) = M_{II}(N/2) + M_{IV}(N/2), \tag{A.40}$$

$$M_{IV}(N) = 2 \cdot M_{II}(N/2) + 3N/2, \tag{A.41}$$

$$A_{II}(N) = A_{II}(N/2) + A_{IV}(N/2) + N, \tag{A.42}$$

$$A_{IV}(N) = 2 \cdot A_{II}(N/2) + 5N/2 - 2. \tag{A.43}$$

## A.6. Computational Complexity Comparison for $N = q \times 2^\lambda$

Figure B.1 depicts the number of multiplications per input sample for the proposed mix-radix algorithm for computing DCT-IV of length $N = q \times 2^\lambda$ and shows the efficiency of sequence lengths other than a power of two. On the other hand, the fast computation of DCT-II of length $N = q \times 2^\lambda$ can be realized through the radix-2 [45] and radix-$q$ [47]

algorithms. The associated arithmetical costs are

$$M_{II}(N) = 2 \cdot M_{II}(N/2) + N/2, \quad N > q, \tag{A.44}$$

$$A_{II}(N) = 2 \cdot A_{II}(N/2) + 3N/2\text{-}1, \ N > q. \tag{A.45}$$

Table B.1 lists the arithmetic complexity reduction of DCT-II and DCT-IV when $q = 3$ and 9 by comparing the proposed mixed-radix method and the DCT-II-based method. The result shows the introduction of the proposed radix-$q$ algorithm for DCT-IV computation improves not only the computation of DCT-IV but also that of DCT-II for the two cases due to the more efficient computation of length-3 and length-9 DCTs-IV.
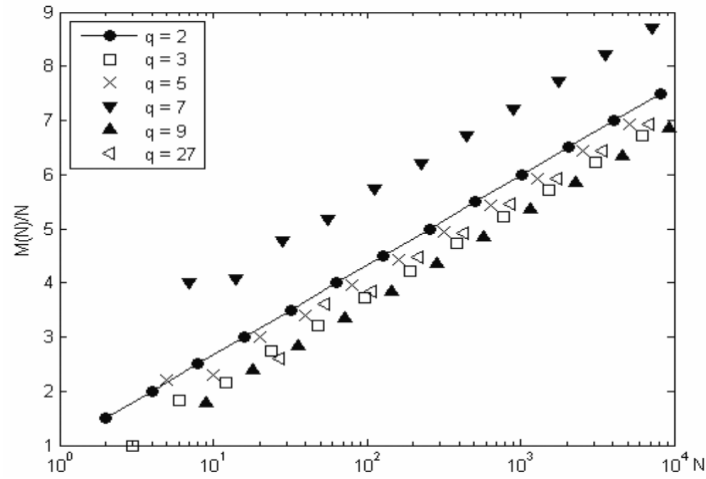


Figure A. 1. Multiplicative cost of DCT-IV by the proposed method for $N = q \times 2^{\lambda}$

Table A. 1. Arithmetic Complexity Reduction

| $q = 3$ | DCT-IV | | DCT-II | | $q = 9$ | DCT-IV | | DCT-II | |
|---|---|---|---|---|---|---|---|---|---|
| $N$ | × | + | × | + | $N$ | × | + | × | + |
| 12 | 2 | 0 | 1 | 0 | 18 | 0 | 0 | 1 | 2 |
| 24 | 2 | 0 | 3 | 0 | 36 | 2 | 4 | 1 | 2 |
| 48 | 6 | 0 | 5 | 0 | 72 | 2 | 4 | 3 | 6 |
| 96 | 10 | 0 | 11 | 0 | 144 | 6 | 12 | 5 | 10 |
| 192 | 22 | 0 | 21 | 0 | 288 | 10 | 20 | 11 | 22 |
| 384 | 42 | 0 | 43 | 0 | 576 | 22 | 44 | 21 | 42 |
| 768 | 86 | 0 | 85 | 0 | 1152 | 42 | 84 | 43 | 86 |
| 1536 | 170 | 0 | 171 | 0 | 2304 | 86 | 172 | 85 | 170 |

# APPENDIX B

# AUTOREGRESSIVE MODELING OF TEMPORAL/SPECTRAL ENVELOPES WITH FINITE-LENGTH DISCRETE TRIGONOMETRIC TRANSFORMS

Autoregressive (AR) modeling [53], [64], also known as linear prediction (LP), has received more and more applications in audio coding. For example, SBR uses a second-order linear predictor for inverse filtering. MPEG-4 Audio Lossless Coding (ALS) [65] generates residuals with a smaller dynamic range via linear prediction. Also, some audio coding approaches are based on linear prediction performed on a warped frequency scale [66], [67]. In additional to the applying of the AR modeling in the time domain, due to the duality between the squared Hilbert envelope and the power spectrum [27], the AR modeling can be also applied to spectral sequences for temporal envelope estimation. In MPEG-2/4 AAC, the Temporal Noise Shaping (TNS) [27]-[30] is utilized as one of effective mechanisms for reducing the pre-echo noise that is a typical and critical artifact in audio coding. The TNS applies an open-loop linear prediction [31] across frequency lines prior to quantization in encoder to achieve the temporal envelope shaping on the quantization noise in decoder.

Although the AR modeling is always preformed on windowed signals in practice, its theoretical derivation was given through the Fourier theory of infinite discrete-time sequences or continuous signals in the literatures, such as [53] and [64]. In [27]-[30], Herre and Johnston explained the concept of TNS through the duality between the squared Hilbert envelope and the power spectrum for continuous signals. Likewise, Kumaresan et al. [68]-[72] formulated the linear prediction in spectral domain equations for the AR modeling of temporal envelope

in the indirect ways. No exact derivation for finite sequences was developed until Athineos and Ellis [73] formulated via matrix operations the solution of the problem that finding an AR model of a discrete spectrum and relating it to the temporal envelope of the finite time-domain sequence. However, the derivation in [73] was limited in the scenario when the discrete spectrum is the odd type-I discrete cosine transform (DCT-I) coefficients.

In Appendix B, we concern the temporal and spectral AR modeling of a finite sequence when one of the 16 members of the discrete trigonometric transform (DTT) is used in the temporal and spectral domains. Different from DCT-I, other DTTs have a 1/2-sample delay in the time domain and/or a 1/2-sample advance in the frequency domain. When considering a finite-length sequence as a discrete periodic signal obtained by sampling a continuous signal, we need to consider the aliasing effect in the dual domain. We systematically establish the AR modeling fundamentals for the DTTs by exploiting the relationship of the DTTs and the generalized discrete Fourier transforms (GDFTs) [76]. We address the AR problem with GDFTs by extending the well-known relationship between the autocorrelation and the power spectrum to the GDFT/Inverse GDFT domains. Then we define new finite-length analytical transformations based on GDFTs. Through the analytical transformations, we establish the AR modeling fundamentals for DTTs by relating the DTT spectra to the corresponding GDFT spectra with appropriate symmetric extension or zero padding operations. In addition to the temporal Hilbert envelope, we also concern the power envelope estimation for a real-valued sequence without introducing the Hilbert signal. The dual results can be derived with the consistent representation in the temporal and spectral domains, i.e., both are periodic and finite. Our formulation is expressed entirely in the discrete finite domain in matrix form. The compact expressions not only disclose that the AR modeling concept can hold in each DTT domain, not limited in DCT-I domain, but also can be used for more clearly examining the related methods based on AR modeling in DTTs.

# B.1.  Preliminaries

To derive the AR modeling with the sixteen DTTs, we summarize the common terms and the existing theorems on the convolution-multiplication and periodicity properties for the GDFTs. The convolution-multiplication property sets the fundamental for modeling the temporal/spectral envelopes. The periodicity property is fundamental to discuss the effect of finite-length transforms when applying to periodic sequences. Then, the terms, transform formula, periodicity, and the relation with GDFTs are summarized for the sixteen DTTs.

## B.1.1.  Notations

Throughout Appendix B, we use calligraphic capital letters to denote matrices (e.g., $A$, $G$, $T$) and calligraphic lower case letters to denote column vectors (e.g., $a$, $x$, $y$). For vectors and matrices, both row and column indices used are zero based. To refer to the $k$th entry of $x$, the notations $x_k$ and $(x)_k$ are used. Some operation notations are described as follows. Superscripts $(T)$, $(H)$, and $(*)$ denote the transpose, Hermitian transpose, and conjugate operations, respectively. The notation ( ∘ ) denotes the Hadamard product (i.e., the entry-wise product of two vectors or matrices); ($\| \cdot \|$) denotes 2-norm. In terms of linear algebra, we consider and represent a finite sequence $x(n)$, for $n_0 \leq n \leq n_1$, as a column vector $x$ of length $(n_1 - n_0 + 1)$:

$$x = [x(n_0), x(n_0 + 1), x(n_0 + 2),..., x(n_1)]^T .$$

## B.1.2.  Generalized Discrete Fourier Transform

The generalized DFT (GDFT) [77] of a finite sequence $x(n)$, $n = 0, 1, \ldots, N - 1$, is defined as

$$y(k) = \sum_{n=0}^{N-1} x(n) \exp\{-j2\pi(k + a)(n + b)/N\}, \text{ for } k = 0, 1, \ldots, N - 1. \tag{B.1}$$

Four special forms of the GDFT arise when $a$ and $b$ take on the values 0 or 1/2. They are

classified and named as follows [76]: (i) DFT (Discrete Fourier transform): $a = 0$ and $b = 0$; (ii) OTDFT (Odd-Time DFT): $a = 0$ and $b = 1/2$; (iii) OFDFT (Odd-Frequency DFT): $a = 1/2$ and $b = 0$; (iv) O$^2$DFT (Odd-Time Odd-Frequency DFT): $a = 1/2$ and $b = 1/2$. The last three transforms can be regarded as the modified version of the DFT with a 1/2-sample delay in the time domain and/or a 1/2-sample advance in the frequency domain. The GDFT matrix is defined by $[G_{a,b}]_{k,n} = \exp\{-j2\pi(k + a)(n + b)/N\}$, where the row and column indexes are $k, n = 0, 1,\ldots, N - 1$. Since the inverse GDFT (IGDFT) matrix is the scaled Hermitian transpose of the forward GDFT matrix, the IGDFT matrix is related to the forward matrix as

$$G_{a,b}^{-1} = \tfrac{1}{N} G_{a,b}^{H} = \tfrac{1}{N} G_{b,a}^{*}.$$
(B.2)

### B.1.3. Generalized-Periodic Sequence, Periodic Convolution, and GDFT

Considering the generalized-periodic sequence (GPS) by extending a finite sequence into an infinite sequence in either strictly periodic or anti-periodic way, Martucci summarized the four different periodic relationships for the four special GDFTs/IGDFTs in Table B.1. A sequence is said to be anti-periodic with period $N$ if $x(n) = -x(n + N)$ for all $n$. For a period-$N$ GPS, we refer to the samples in the base period (for index $n = 0, 1,\ldots, N - 1$) as the representative samples or vector.

The periodic convolution of two period-$N$ GPSs, $\tilde{x}(n)$ and $\tilde{y}(n)$, of the same type (i.e., both of them are either strictly periodic or anti-periodic) is defined as

$$\tilde{x}(n) \otimes \tilde{y}(n) = \sum_{k=0}^{N-1} \tilde{x}(k)\tilde{y}(n-k) = \sum_{k=0}^{N-1} \tilde{x}(n-k)\tilde{y}(k).$$
(B.3)

The periodic convolution is also a GPS with the same periodic type and period. On the other hand, the circular and skew-circular convolutions of two vectors $x$ and $y$ are defined by (B.4) and (B.5), respectively.

$$(\boldsymbol{x} \;\textcircled{c}\; \boldsymbol{y})_n = \sum_{k=0}^{n} \boldsymbol{x}_k \boldsymbol{y}_{n-k} + \sum_{k=n+1}^{N-1} \boldsymbol{x}_k \boldsymbol{y}_{n-k+N} \text{ , for } n = 0, 1,\dots, N-1. \tag{B.4}$$

$$(\boldsymbol{x} \;\textcircled{s}\; \boldsymbol{y})_n = \sum_{k=0}^{n} \boldsymbol{x}_k \boldsymbol{y}_{n-k} - \sum_{k=n+1}^{N-1} \boldsymbol{x}_k \boldsymbol{y}_{n-k+N} \text{ , for } n = 0, 1,\dots, N-1. \tag{B.5}$$

The circular and skew-circular convolutions of two length-$N$ sequences are, respectively, equivalent to the representative vectors of the periodic convolutions of the period-$N$ strictly periodic and anti-periodic sequences extended from the finite sequences.

Table B.1. Periodicity Properties of GDFTs and IGDFTs

| Periodicity Property before-after Transform | GDFT with the relation | IGDFT with the relation |
|---|---|---|
| (Strictly Periodic, Strictly Periodic) | $\boldsymbol{G}_{0,0}$ (DFT) | $\boldsymbol{G}_{0,0}^{-1}$ (IDFT) |
| (Strictly Periodic, Anti-Periodic) | $\boldsymbol{G}_{0,\frac{1}{2}}$ (OTDFT) | $\boldsymbol{G}_{\frac{1}{2},0}^{-1}$ (IOFDFT) |
| (Ant-Periodic, Strictly Periodic) | $\boldsymbol{G}_{\frac{1}{2},0}$ (OFDFT) | $\boldsymbol{G}_{0,\frac{1}{2}}^{-1}$ (IOTDFT) |
| (Anti-Periodic, Anti-Periodic) | $\boldsymbol{G}_{\frac{1}{2},\frac{1}{2}}$ (O$^2$DFT) | $\boldsymbol{G}_{\frac{1}{2},\frac{1}{2}}^{-1}$ (IO$^2$DFT) |

## B.1.4. Convolution-Multiplication Property of GDFT

The DFT has the convolution-multiplication property that the inverse transformation after entry-wise multiplication gives the same result as the circular convolution of the original sequences. Martucci [76] derived such properties for other GDFTs. We summarize the results in matrix/vector form as follows. Let $\boldsymbol{u} = \boldsymbol{x} \;\textcircled{c}\; \boldsymbol{y}$ and $\boldsymbol{w} = \boldsymbol{x} \;\textcircled{s}\; \boldsymbol{y}$, then the following properties hold:

$$\boldsymbol{u} = \boldsymbol{G}_{0,0}^{-1}[(\boldsymbol{G}_{0,0}\boldsymbol{x}) \circ (\boldsymbol{G}_{0,0}\boldsymbol{y})]. \tag{B.6}$$

$$\boldsymbol{u} = \boldsymbol{G}_{0,\frac{1}{2}}^{-1}[(\boldsymbol{G}_{0,\frac{1}{2}}\boldsymbol{x}) \circ (\boldsymbol{G}_{0,0}\boldsymbol{y})]. \tag{B.7}$$

$$\boldsymbol{w} = \boldsymbol{G}_{\frac{1}{2},0}^{-1}[(\boldsymbol{G}_{\frac{1}{2},0}\boldsymbol{x}) \circ (\boldsymbol{G}_{\frac{1}{2},0}\boldsymbol{y})]. \tag{B.8}$$

$$\boldsymbol{w} = \boldsymbol{G}_{\frac{1}{2},\frac{1}{2}}^{-1}[(\boldsymbol{G}_{\frac{1}{2},\frac{1}{2}}\boldsymbol{x}) \circ (\boldsymbol{G}_{\frac{1}{2},0}\boldsymbol{y})]. \tag{B.9}$$

Notice that the implied periodicity of $\boldsymbol{u}_n$ is strictly periodic and that of $\boldsymbol{w}_n$ is anti-periodic due

to the periodicity inherence of the periodic convolution of the original sequences represented by $\boldsymbol{x}$ and $\boldsymbol{y}$.

### B.1.5. Discrete Trigonometric Transform

The family of DTTs comprises eight versions of the discrete cosine transform (DCT) and eight versions of the discrete sine transform (DST). Martucci formulated the DTTs through the convolution forms as defined in [76, Appendix]. The orthogonal-like relations between the inverse and forward DTTs are

$$T_I^{-1} = \tfrac{1}{M}T_I \,, \;\; T_{II}^{-1} = \tfrac{1}{M}T_{III} \,, \;\; T_{III}^{-1} = \tfrac{1}{M}T_{II} \,, \text{and} \;\; T_{IV}^{-1} = \tfrac{1}{M}T_{IV} \;\;, \tag{B.10}$$

where the DTTs in both sides of each equality must be the same in the categories of cosine or sine and even or odd; and $M$ is $2N$ and $2N-1$ for the even and odd cases, respectively.

### B.1.6. DTT and GDFT

#### B.1.6.1. Symmetric-Extension Operator

Just as the special forms of the GDFT provide representations for GPSs, the symmetry and periodicity of the basis functions of the DTTs establish a one-to-one correspondence between the DTTs and the 16 symmetric-periodic sequences (SPSs) that are summarized in [76, Fig. 2]. Since these SPSs are also generalized-periodic, the SPS extended from a DTT of a finite sequence can be produced from the corresponding GDFT of that sequence after having been symmetrically extended to a base period. Therefore, each DTT can be directly constructed in terms of its corresponding GDFT by cascading an appropriate symmetric-extension operator as defined in Table B.2, where the subscripts are in terms of Martucci's naming rules, including whole-sample symmetry (WS), whole-sample anti-symmetry (WA), half-sample symmetry (HS), and half-sample anti-symmetry (HA). The

notations $\boldsymbol{I}_N$ and $\boldsymbol{J}_N$ mean the identity matrix and reversal matrix of order $N$. For instance, we have

$$\boldsymbol{y} = \boldsymbol{G}_{0,\frac{1}{2}} \boldsymbol{E}_{HSHS} \boldsymbol{x} = \boldsymbol{C}_{II}^e \boldsymbol{x}, \tag{B.11}$$

where $\boldsymbol{y}$ is $P \times 1$, $\boldsymbol{G}_{0,\frac{1}{2}}$ is $P \times 2N$, $\boldsymbol{E}_{HSHS}$ is $2N \times N$, $\boldsymbol{C}_{II}^e$ is $P \times N$, $\boldsymbol{x}$ is $N \times 1$, and positive integer $P$ determines how long the output SPS is captured.

Table B.2. Matrix Forms for Symmetric Extension Operators

| | $M = 2N$ | | $M = 2N - 1$ |
|---|---|---|---|
| $\boldsymbol{E}_{WSWS}$ | $\begin{bmatrix} \boldsymbol{I}_{N+1} \\ \hdashline \boldsymbol{0}_{N-1\times 1} & \boldsymbol{J}_{N-1} & \boldsymbol{0}_{N-1\times 1} \end{bmatrix}$ | $\boldsymbol{E}_{WSHS}$ | $\begin{bmatrix} \boldsymbol{I}_N \\ \hdashline \boldsymbol{0}_{N-1\times 1} & \boldsymbol{J}_{N-1} \end{bmatrix}$ |
| $\boldsymbol{E}_{WAWA}$ | $\begin{bmatrix} \boldsymbol{0}_{1\times N-1} \\ \hdashline \boldsymbol{I}_{N-1} \\ \hdashline \boldsymbol{0}_{1\times N-1} \\ \hdashline -\boldsymbol{J}_{N-1} \end{bmatrix}$ | $\boldsymbol{E}_{WAHA}$ | $\begin{bmatrix} \boldsymbol{0}_{1\times N-1} \\ \hdashline \boldsymbol{I}_{N-1} \\ \hdashline -\boldsymbol{J}_{N-1} \end{bmatrix}$ |
| $\boldsymbol{E}_{HSHS}$ $\boldsymbol{E}_{HAHS}$ | $\begin{bmatrix} \boldsymbol{I}_N \\ \hdashline \boldsymbol{J}_N \end{bmatrix}$ | $\boldsymbol{E}_{HSWS}$ $\boldsymbol{E}_{HAWS}$ | $\begin{bmatrix} \boldsymbol{I}_N \\ \hdashline \boldsymbol{J}_{N-1} & \boldsymbol{0}_{N-1\times 1} \end{bmatrix}$ |
| $\boldsymbol{E}_{HAHA}$ $\boldsymbol{E}_{HSHA}$ | $\begin{bmatrix} \boldsymbol{I}_N \\ \hdashline -\boldsymbol{J}_N \end{bmatrix}$ | $\boldsymbol{E}_{HAWA}$ $\boldsymbol{E}_{HSWA}$ | $\begin{bmatrix} \boldsymbol{I}_{N-1} \\ \hdashline \boldsymbol{0}_{1\times N-1} \\ \hdashline -\boldsymbol{J}_{N-1} \end{bmatrix}$ |
| $\boldsymbol{E}_{WSWA}$ | $\begin{bmatrix} \boldsymbol{I}_N \\ \hdashline \boldsymbol{0}_{1\times N} \\ \hdashline \boldsymbol{0}_{N-1\times 1} & -\boldsymbol{J}_{N-1} \end{bmatrix}$ | $\boldsymbol{E}_{WSHA}$ | $\begin{bmatrix} \boldsymbol{I}_N \\ \hdashline \boldsymbol{0}_{N-1\times 1} & -\boldsymbol{J}_{N-1} \end{bmatrix}$ |
| $\boldsymbol{E}_{WAWS}$ | $\begin{bmatrix} \boldsymbol{0}_{1\times N} \\ \hdashline \boldsymbol{I}_N \\ \hdashline \boldsymbol{J}_{N-1} & \boldsymbol{0}_{N-1\times 1} \end{bmatrix}$ | $\boldsymbol{E}_{WAHS}$ | $\begin{bmatrix} \boldsymbol{0}_{1\times N-1} \\ \hdashline \boldsymbol{I}_{N-1} \\ \hdashline \boldsymbol{J}_{N-1} \end{bmatrix}$ |

### B.1.6.2. Zero-Padding and Selective Matrices

For capturing the standard index range of the DTT output, the transposed zero-padding matrix is introduced. The $(r + p + q) \times p$ zero-padding matrix $\boldsymbol{Z}_{r,p,q}$ is defined as $[\boldsymbol{0}_{p\times r} \ \boldsymbol{I}_p \ \boldsymbol{0}_{p\times q}]^T$. The name "zero-padding" comes from the fact that left-multiplying a length-$p$

column vector $x$ by $Z_{r,p,q}$ is equivalent to padding $x$ to the up and down by $r$ and $q$ zeros, respectively. On the contrary, left-multiplying a length-$(r + p + q)$ column vector $x$ by $Z_{r,p,q}^T$ is equivalent to selecting $x_n$ for $r \leqq n \leqq p + r - 1$. For instance, $Z_{3,4,2}^T \cdot [x_0, x_1, ..., x_8]^T = [x_3, x_4, x_5, x_6]^T$. Hence, we name the transposed zero-padding matrix as the "selective" matrix.

### B.1.6.3. Relationship of DTT and GDFT

By using the selective matrix and symmetric-extension operator defined above, we can express the relation between a DTT matrix and its corresponding GDFT matrix as

$$T_q = Z_q^T \cdot F_q \cdot E_q, \tag{B.12}$$

where $T_q$ denotes the DTT matrix, $F_q$ denotes the GDFT matrix, $Z_q^T$ denotes the selective matrix, $E_q$ denotes the symmetric-extension operator; and subscript $q$ indicates the type of DTT, which takes on I, II, III, and IV. Alternatively, by left-multiplying the DTT matrix by a symmetric-extension operator to obtain another half of samples in the base period of the corresponding GDFT, we can define the correspondent symmetric-extension operator $E'_q$ through the following relation.

$$E'_q \cdot T_q = F_q \cdot E_q. \tag{B.13}$$

### B.1.6.4. Relationship of IDTT and IGDFT

The dual formula related to (B.13) is derived as follows:

$$E_q T_q^{-1} = F_q^{-1}(F_q E_q)T_q^{-1} = F_q^{-1}(E'_q T_q)T_q^{-1} = F_q^{-1}E'_q. \tag{B.14}$$

Note that $E_q$ and $E'_q$ are interchanged in (B.13) and (B.14). Taking conjugate of (B.14) and using the properties (B.2) and (B.10) lead to $E_q T_{\Phi(q)} = F_{\Phi(q)} E'_q$, and hence $E_q = E'_{\Phi(q)}$, where

Table B.3. Definitions of Related Matrices for DTT.

| | $q$ | $T_q$ | Input Index Range | $Z_q$ | $F_q$ | $E_q$ | $E'_q$ | $A_q^+$ | $W'^+_q$ | $K_q$ | $r_{Freq.}$ |
|---|---|---|---|---|---|---|---|---|---|---|---|
| $M = 2N$ | I | $C_I^e$ | $0 \to N$ | $Z_{0,N+1,N-1}$ | $G_{0,0}$ | $E_{WSWS}$ | $E_{WSWS}$ | $A_I^{e+}$ | $W_{N+1}^{II}$ | $G_{0,0}$ | c |
| | II | $C_{II}^e$ | $0 \to N-1$ | $Z_{0,N,N}$ | $G_{0,\frac{1}{2}}$ | $E_{HSHS}$ | $E_{WSWA}$ | $A_{II}^{e+}$ | $W_N^I$ | $G_{0,\frac{1}{2}}$ | s |
| | III | $C_{III}^e$ | $0 \to N-1$ | $Z_{0,N,N}$ | $G_{\frac{1}{2},0}$ | $E_{WSWA}$ | $E_{HSHS}$ | $A_{III}^{e+}$ | $2I_N$ | $G_{0,0}$ | c |
| | IV | $C_{IV}^e$ | $0 \to N-1$ | $Z_{0,N,N}$ | $G_{\frac{1}{2},\frac{1}{2}}$ | $E_{HSHA}$ | $E_{HSHA}$ | $A_{IV}^{e+}$ | $2I_N$ | $G_{0,\frac{1}{2}}$ | s |
| | I | $S_I^e$ | $1 \to N-1$ | $Z_{1,N-1,N}$ | $jG_{0,0}$ | $E_{WAWA}$ | $E_{WAWA}$ | $A_I^{e+}$ | $2I_{N-1}$ | $G_{0,0}$ | c |
| | II | $S_{II}^e$ | $1 \to N$ | $Z_{0,N,N}$ | $jG_{0,\frac{1}{2}}$ | $E_{HAHA}$ | $E_{WAWS}$ | $A_{II}^{e+}$ | $W_N^I$ | $G_{0,\frac{1}{2}}$ | s |
| | III | $S_{III}^e$ | $0 \to N-1$ | $Z_{1,N,N-1}$ | $jG_{\frac{1}{2},0}$ | $E_{WAWS}$ | $E_{HAHA}$ | $A_{III}^{e+}$ | $2I_N$ | $G_{0,0}$ | c |
| | IV | $S_{IV}^e$ | $0 \to N-1$ | $Z_{0,N,N}$ | $jG_{\frac{1}{2},\frac{1}{2}}$ | $E_{HAHS}$ | $E_{HAHS}$ | $A_{IV}^{e+}$ | $2I_N$ | $G_{0,\frac{1}{2}}$ | s |
| $M = 2N-1$ | I | $C_I^o$ | $0 \to N-1$ | $Z_{0,N,N-1}$ | $G_{0,0}$ | $E_{WSHS}$ | $E_{WSHS}$ | $A_I^{o+}$ | $W_N^I$ | $G_{0,0}$ | c |
| | II | $C_{II}^o$ | $0 \to N-1$ | $Z_{0,N,N-1}$ | $G_{0,\frac{1}{2}}$ | $E_{HSWS}$ | $E_{WSHA}$ | $A_{II}^{o+}$ | $W_N^I$ | $G_{0,\frac{1}{2}}$ | s |
| | III | $C_{III}^o$ | $0 \to N-1$ | $Z_{0,N,N-1}$ | $G_{\frac{1}{2},0}$ | $E_{WSHA}$ | $E_{HSWS}$ | $A_{III}^{o+}$ | $W_N^{III}$ | $G_{0,0}$ | c |
| | IV | $C_{IV}^o$ | $0 \to N-2$ | $Z_{0,N-1,N}$ | $G_{\frac{1}{2},\frac{1}{2}}$ | $E_{HSWA}$ | $E_{HSWA}$ | $A_{IV}^{o+}$ | $2I_{N-1}$ | $G_{0,\frac{1}{2}}$ | s |
| | I | $S_I^o$ | $1 \to N-1$ | $Z_{1,N-1,N-1}$ | $jG_{0,0}$ | $E_{WAHA}$ | $E_{WAHA}$ | $A_I^{o+}$ | $2I_{N-1}$ | $G_{0,0}$ | c |
| | II | $S_{II}^o$ | $1 \to N-1$ | $Z_{0,N-1,N}$ | $jG_{0,\frac{1}{2}}$ | $E_{HAWA}$ | $E_{WAHS}$ | $A_{II}^{o+}$ | $W_{N-1}^I$ | $G_{0,\frac{1}{2}}$ | s |
| | III | $S_{III}^o$ | $0 \to N-2$ | $Z_{1,N-1,N-1}$ | $jG_{\frac{1}{2},0}$ | $E_{WAHS}$ | $E_{HAWA}$ | $A_{III}^{o+}$ | $W_{N-1}^{III}$ | $G_{0,0}$ | c |
| | IV | $S_{IV}^o$ | $0 \to N-1$ | $Z_{0,N,N-1}$ | $jG_{\frac{1}{2},\frac{1}{2}}$ | $E_{HAWS}$ | $E_{HAWS}$ | $A_{IV}^{o+}$ | $W_N^{III}$ | $G_{0,\frac{1}{2}}$ | s |

subscript $\Phi(q)$ indicates the pair type according to (B.10) (i.e., $\Phi(I) = I$, $\Phi(II) = III$, $\Phi(III) = II$, and $\Phi(IV) = IV$). On the other hand, by (B.2) and (B.10), the dual formula related to (B.12) is derived as follows:

$$T_q^{-1} = \tfrac{1}{M} T_{\Phi(q)} = \tfrac{1}{M} Z_{\Phi(q)}^T F_{\Phi(q)}^* E_{\Phi(q)} = Z_{\Phi(q)}^T F_q^{-1} E_{\Phi(q)} = Z_{\Phi(q)}^T F_q^{-1} E'_q. \tag{B.15}$$

Since $T_{\Phi(q)}$ is real-valued, the conjugate operation can be applied in the second equality.

The relationships of DTT/IDTT and GDFT/IGDFT as illustrated in (B.12)-(B.15) are depicted in pictorially in Figures B.1 and B.2. In the above generic formulas, the specific definitions of the related matrices are given in the first six columns of Tables B.3 and B.4. As

an example, according to (B.12) and Table B.3, the relation between the odd DST-II of length $N-1$ and the OTDFT of length $M$ that equals $2N-1$ is given by

$$S_{II}^o x = Z_{0,N-1,N}^T \cdot jG_{0,\frac{1}{2}} \cdot E_{HAWA}x = y,$$  (B.16)

where $x = [x(1), x(2),..., x(N-1)]^T$ and $y = [y(0), y(1),..., y(N-2)]^T$. According to (B.13) and Table B.4, another relation is expressed by

$$E_{WAHS} S_{II}^o x = jG_{0,\frac{1}{2}} E_{HAWA}x.$$  (B.17)

Table B.4. Definitions of Related Matrices for IDTT.

| | $q$ | $T_q^{-1}$ | Input Index Range | $Z_{\Phi(q)}$ | $F_q^{-1}$ | $E_q$ | $E_q'$ | $A_q^-$ | $W_q'^-$ | $\Gamma_q^{-1}$ | $r_{Time}$ |
|---|---|---|---|---|---|---|---|---|---|---|---|
| $M=2N$ | I | $C_I^{e-1}$ | $0 \to N$ | $Z_{0,N+1,N-1}$ | $G_{0,0}^{-1}$ | $E_{WSWS}$ | $E_{WSWS}$ | $A_I^{e-}$ | $W_{N+1}^{II}$ | $G_{0,0}^{-1}$ | c |
| | II | $C_{II}^{e-1}$ | $0 \to N-1$ | $Z_{0,N,N}$ | $G_{0,\frac{1}{2}}^{-1}$ | $E_{HSHS}$ | $E_{WSWA}$ | $A_{II}^{e-}$ | $2I_N$ | $G_{0,0}^{-1}$ | c |
| | III | $C_{III}^{e-1}$ | $0 \to N-1$ | $Z_{0,N,N}$ | $G_{\frac{1}{2},0}^{-1}$ | $E_{WSWA}$ | $E_{HSHS}$ | $A_{III}^{e-}$ | $W_N^I$ | $G_{\frac{1}{2},0}^{-1}$ | s |
| | IV | $C_{IV}^{e-1}$ | $0 \to N-1$ | $Z_{0,N,N}$ | $G_{\frac{1}{2},\frac{1}{2}}^{-1}$ | $E_{HSHA}$ | $E_{HSHA}$ | $A_{IV}^{e-}$ | $2I_N$ | $G_{\frac{1}{2},0}^{-1}$ | s |
| | I | $S_I^{e-1}$ | $1 \to N-1$ | $Z_{1,N-1,N}$ | $-jG_{0,0}^{-1}$ | $E_{WAWA}$ | $E_{WAWA}$ | $A_I^{e-}$ | $2I_{N-1}$ | $G_{0,0}^{-1}$ | c |
| | II | $S_{II}^{e-1}$ | $0 \to N-1$ | $Z_{1,N,N-1}$ | $-jG_{0,\frac{1}{2}}^{-1}$ | $E_{HAHA}$ | $E_{WAWS}$ | $A_{II}^{e-}$ | $2I_N$ | $G_{0,0}^{-1}$ | c |
| | III | $S_{III}^{e-1}$ | $1 \to N$ | $Z_{0,N,N}$ | $-jG_{\frac{1}{2},0}^{-1}$ | $E_{WAWS}$ | $E_{HAHA}$ | $A_{III}^{e-}$ | $W_N^I$ | $G_{\frac{1}{2},0}^{-1}$ | s |
| | IV | $S_{IV}^{e-1}$ | $0 \to N-1$ | $Z_{0,N,N}$ | $-jG_{\frac{1}{2},\frac{1}{2}}^{-1}$ | $E_{HAHS}$ | $E_{HAHS}$ | $A_{IV}^{e-}$ | $2I_N$ | $G_{\frac{1}{2},0}^{-1}$ | s |
| $M=2N-1$ | I | $C_I^{o-1}$ | $0 \to N-1$ | $Z_{0,N,N-1}$ | $G_{0,0}^{-1}$ | $E_{WSHS}$ | $E_{WSHS}$ | $A_I^{o-}$ | $W_N^I$ | $G_{0,0}^{-1}$ | c |
| | II | $C_{II}^{o-1}$ | $0 \to N-1$ | $Z_{0,N,N-1}$ | $G_{0,\frac{1}{2}}^{-1}$ | $E_{HSWS}$ | $E_{WSHA}$ | $A_{II}^{o-}$ | $W_N^{III}$ | $G_{0,0}^{-1}$ | c |
| | III | $C_{III}^{o-1}$ | $0 \to N-1$ | $Z_{0,N,N-1}$ | $G_{\frac{1}{2},0}^{-1}$ | $E_{WSHA}$ | $E_{HSWS}$ | $A_{III}^{o-}$ | $W_N^I$ | $G_{\frac{1}{2},0}^{-1}$ | s |
| | IV | $C_{IV}^{o-1}$ | $0 \to N-2$ | $Z_{0,N-1,N}$ | $G_{\frac{1}{2},\frac{1}{2}}^{-1}$ | $E_{HSWA}$ | $E_{HSWA}$ | $A_{IV}^{o-}$ | $2I_{N-1}$ | $G_{\frac{1}{2},0}^{-1}$ | s |
| | I | $S_I^{o-1}$ | $1 \to N-1$ | $Z_{1,N-1,N-1}$ | $-jG_{0,0}^{-1}$ | $E_{WAHA}$ | $E_{WAHA}$ | $A_I^{o-}$ | $2I_{N-1}$ | $G_{0,0}^{-1}$ | c |
| | II | $S_{II}^{o-1}$ | $0 \to N-2$ | $Z_{1,N-1,N-1}$ | $-jG_{0,\frac{1}{2}}^{-1}$ | $E_{HAWA}$ | $E_{WAHS}$ | $A_{II}^{o-}$ | $W_{N-1}^{III}$ | $G_{0,0}^{-1}$ | c |
| | III | $S_{III}^{o-1}$ | $1 \to N-1$ | $Z_{0,N-1,N}$ | $-jG_{\frac{1}{2},0}^{-1}$ | $E_{WAHS}$ | $E_{HAWA}$ | $A_{III}^{o-}$ | $W_{N-1}^I$ | $G_{\frac{1}{2},0}^{-1}$ | s |
| | IV | $S_{IV}^{o-1}$ | $0 \to N-1$ | $Z_{0,N,N-1}$ | $-jG_{\frac{1}{2},\frac{1}{2}}^{-1}$ | $E_{HAWS}$ | $E_{HAWS}$ | $A_{IV}^{o-}$ | $W_N^{III}$ | $G_{\frac{1}{2},0}^{-1}$ | s |
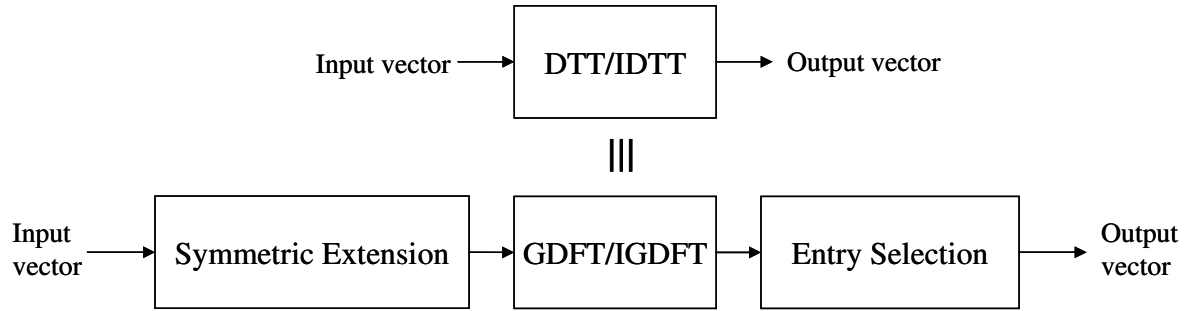
Figure B.1. Relationship of DTT/IDTT and GDFT/IGDFT. A pictorial representation of (B.12) and (B.15).
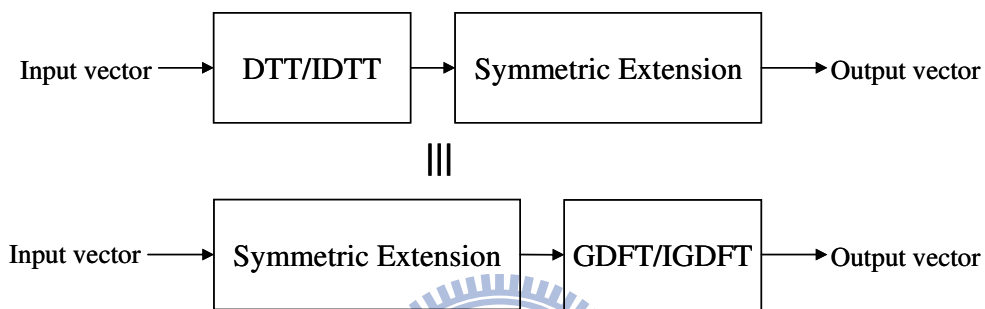


Figure B.2. Relationship of DTT/IDTT and GDFT/IGDFT. A pictorial representation of (B.13) and (B.14).

## B.2. Autoregressive Modeling and GDFT

In this section, we first establish the time-frequency relation between the periodic autocorrelation and power spectrum in the GDFT frequency domain. Then we show that, like the traditional approach, the Yule-Walker equations consisting of periodic autocorrelations is derived in the least square error sense for evaluating the AR parameters in the finite length problems with GDFTs.

Before proceeding, we show a general property of two GPSs with period $N$, which will be heavily used in later derivation.

**Lemma 1** Given two GPSs, $\tilde{x}(n)$ and $\tilde{y}(n)$, which are either strictly periodic or anti-periodic with period $N$. Then any summation over successive $N$ terms of their product is equal to the summation over the base period from 0 to $N - 1$. That is,

$$\sum_{n=i}^{i+N-1} \tilde{x}(n)\tilde{y}(n) = \sum_{n=0}^{N-1} \tilde{x}(n)\tilde{y}(n) \text{, for any integer } i.$$ (B.18)

*Proof:* Since $\tilde{x}(n+N)\tilde{y}(n+N) = \tilde{x}(n)\tilde{y}(n)$, the product $\tilde{x}(n)\tilde{y}(n)$ is a strictly periodic sequence with period $N$. Thus, any summation over successive $N$ terms of their product has the same result. ∎

### B.2.1. Autocorrelation and Power Spectrum in GDFT

The periodic correlation of two period-$N$ GPSs $\tilde{x}(n)$ and $\tilde{y}(n)$ of the same type is defined as

$$\tilde{x}(n) * \tilde{y}(n) = \frac{1}{N}\sum_{m=0}^{N-1} \tilde{x}^*(m)\tilde{y}(n+m)$$ (B.19)

Note that the periodic correlation is also a period-$N$ GPS that has the same periodic type as the input GPSs have. Similarly, to distinguish the strictly periodic and anti-periodic cases, the circular and skew-circular correlations of two length-$N$ vectors $\boldsymbol{x}$ and $\boldsymbol{y}$ are defined as

$$(\boldsymbol{x} *_C \boldsymbol{y})_n = \frac{1}{N}\left[ \sum_{k=0}^{N-n-1} \boldsymbol{x}_k^* \cdot \boldsymbol{y}_{n+k} + \sum_{k=N-n}^{N-1} \boldsymbol{x}_k^* \cdot \boldsymbol{y}_{n+k-N} \right], \text{ for } n = 0, 1, \ldots, N-1.$$ (B.20)

$$(\boldsymbol{x} *_S \boldsymbol{y})_n = \frac{1}{N}\left[ \sum_{k=0}^{N-n-1} \boldsymbol{x}_k^* \cdot \boldsymbol{y}_{n+k} - \sum_{k=N-n}^{N-1} \boldsymbol{x}_k^* \cdot \boldsymbol{y}_{n+k-N} \right], \text{ for } n = 0, 1, \ldots, N-1.$$ (B.21)

The circular and skew-circular correlations of two length-$N$ vectors are, respectively, equivalent to the representative vectors of the periodic correlations of the period-$N$ strictly periodic and anti-periodic sequences extended from the finite vectors.

To express a periodic correlation in terms of a periodic convolution, the flip operation on a GPS is introduced and defined as

$$FLIP\{\tilde{x}(n)\} = \tilde{x}(-n).$$ (B.22)

The flip operation can also preserve the periodicity of the input GPS. For finite sequences of length $N$, the strict-flip and anti-flip operations are defined in matrix form as

$$S_{FLIP} = \begin{bmatrix} 1 & \mathbf{0}_{1\times(N-1)} \\ \hline \mathbf{0}_{(N-1)\times1} & \mathbf{J}_{N-1} \end{bmatrix} \quad \text{and} \quad A_{FLIP} = \begin{bmatrix} 1 & \mathbf{0}_{1\times(N-1)} \\ \hline \mathbf{0}_{(N-1)\times1} & -\mathbf{J}_{N-1} \end{bmatrix}. \tag{B.23}$$

The strict-flip and anti-flip operations of a length-$N$ vector are equivalent to the representative vectors of the flip operations of the period-$N$ strictly periodic and anti-periodic sequences extended from the finite vector. For instance, let $x = [1,2,3,4]^T$, then $S_{FLIP}x = [1,4,3,2]^T$ and $A_{FLIP}x = [1, -4, -3, -2]^T$.

**<u>Theorem 1</u>** Given two period-$N$ GPSs, $\tilde{x}(n)$ and $\tilde{y}(n)$, of the same periodic type. Then,

$$\tilde{x}(n) * \tilde{y}(n) = \tfrac{1}{N} FLIP\{\tilde{x}^*(n)\} \otimes \tilde{y}(n). \tag{B.24}$$

*Proof:* Since both $\tilde{x}^*(m)$ and $\tilde{y}(n+m)$ for any fixed $n$ are either strictly periodic or anti-periodic with period $N$, by Lemma 1, we have

$$\sum_{m=0}^{N-1} \tilde{x}^*(m)\tilde{y}(n+m) = \sum_{m=0}^{N-1} \tilde{x}^*(-m)\tilde{y}(n-m). \qquad \blacksquare$$

**<u>Corollary 1</u>** For two column vectors $x$ and $y$ of length $N$, the following properties hold.

$$x *_C y = \tfrac{1}{N}(S_{FLIP}x^*) \, \text{Ⓒ} \, y, \quad \text{and} \quad x *_S y = \tfrac{1}{N}(A_{FLIP}x^*) \, \text{Ⓢ} \, y. \tag{B.25}$$

$$\blacksquare$$

Like the conjugate relation between the DFTs of a vector and its strict-flipped conjugate [52], we extend without proof such properties for other GDFTs in the next lemma.

**<u>Lemma 2</u>** Consider a column vectors $x$ of length $N$.

(i)  The DFT and OTDFT of the strict-flipped conjugated $x$ can be evaluated by

$$(G_{0,b}S_{FLIP}x^*)_k = \exp(-j4\pi kb/N) \cdot (G_{0,b}x)_k^*,$$
$$\text{for } b = 0 \text{ or } 1/2, \text{ and } k = 0, 1,\ldots, N-1. \tag{B.26}$$

(ii) The OFDFT and $O^2$DFT of the anti-flipped conjugated $x$ can be evaluated by

$$(G_{\frac{1}{2},b}A_{FLIP}x^*)_k = \exp(-j4\pi(k+\tfrac{1}{2})b/N) \cdot (G_{\frac{1}{2},b}x)_k^*,$$
$$\text{for } b = 0 \text{ or } 1/2, \text{ and } k = 0, 1,\ldots, N-1. \tag{B.27}$$

$$\blacksquare$$

The periodic autocorrelation of a GPS $\tilde{x}(n)$ with period $N$ is defined as

$$r_{\tilde{x}}(n) = \tilde{x}(n) * \tilde{x}(n) = \frac{1}{N}\sum_{m=0}^{N-1}\tilde{x}^*(m)\tilde{x}(n+m).$$  (B.28)

For a vector $\boldsymbol{x}$ of length $N$, the circular and skew-circular autocorrelations are defined as

$$r_x^C = \boldsymbol{x} *_C \boldsymbol{x} \quad \text{and} \quad r_x^S = \boldsymbol{x} *_S \boldsymbol{x}.$$  (B.29)

It is well known that the DFT of the circular autocorrelation of a vector equals the DFT power spectrum of the vector. We extend such important relations for other GDFTs and GPSs.

**Theorem 2** Consider a column vector $\boldsymbol{x}$ of length $N$.

(i) The relation between the circular autocorrelation and DFT/OTDFT power spectra is given by

$$r_x^C = \frac{1}{N}\boldsymbol{G}_{0,0}^{-1}[(\boldsymbol{G}_{0,0}\boldsymbol{x})\circ(\boldsymbol{G}_{0,0}\boldsymbol{x})^*] = \frac{1}{N}\boldsymbol{G}_{0,0}^{-1}[(\boldsymbol{G}_{0,\frac{1}{2}}\boldsymbol{x})\circ(\boldsymbol{G}_{0,\frac{1}{2}}\boldsymbol{x})^*].$$  (B.30)

(ii) The relation between the skew-circular autocorrelation and OFDFT/O$^2$DFT power spectra is given by

$$r_x^S = \frac{1}{N}\boldsymbol{G}_{\frac{1}{2},0}^{-1}[(\boldsymbol{G}_{\frac{1}{2},0}\boldsymbol{x})\circ(\boldsymbol{G}_{\frac{1}{2},0}\boldsymbol{x})^*] = \frac{1}{N}\boldsymbol{G}_{\frac{1}{2},0}^{-1}[(\boldsymbol{G}_{\frac{1}{2},\frac{1}{2}}\boldsymbol{x})\circ(\boldsymbol{G}_{\frac{1}{2},\frac{1}{2}}\boldsymbol{x})^*].$$  (B.31)

*Proof:* We first consider the case of skew-circular autocorrelation and OFDFT in part (ii). By Corollary 1, we have

$$r_x^S = (\frac{1}{N}\boldsymbol{A}_{FLIP}\boldsymbol{x}^*)\,\text{Ⓢ}\,\boldsymbol{x}.$$

Thus, using (B.7) yields

$$r_x^S = \frac{1}{N}\boldsymbol{G}_{\frac{1}{2},0}^{-1}[(\boldsymbol{G}_{\frac{1}{2},0}\boldsymbol{A}_{FLIP}\boldsymbol{x}^*)\circ(\boldsymbol{G}_{\frac{1}{2},0}\boldsymbol{x})].$$

Then, by Lemma 2 (ii), we obtain

$$r_x^S = \frac{1}{N}\boldsymbol{G}_{\frac{1}{2},0}^{-1}[(\boldsymbol{G}_{\frac{1}{2},0}\boldsymbol{x})^*\circ(\boldsymbol{G}_{\frac{1}{2},0}\boldsymbol{x})].$$

Due to $\left|(\boldsymbol{G}_{\frac{1}{2},0}\boldsymbol{x})_k\right| = \left|(\boldsymbol{G}_{\frac{1}{2},\frac{1}{2}}\boldsymbol{x})_k\right|$, part (ii) is proved completely. Similarly, part (i) can be proved by the same technique and using (B.6). ∎

**Corollary 2** Consider a column vector $\boldsymbol{y}$ of length $N$.

(iii) The relation between the skew-circular autocorrelation and IOTDFT/IO$^2$DFT power spectra is given by

$$\boldsymbol{r}_y^S = \boldsymbol{G}_{0,\frac{1}{2}}[(\boldsymbol{G}_{0,\frac{1}{2}}^{-1}\boldsymbol{y}) \circ (\boldsymbol{G}_{0,\frac{1}{2}}^{-1}\boldsymbol{y})^*] = \boldsymbol{G}_{0,\frac{1}{2}}[(\boldsymbol{G}_{\frac{1}{2},\frac{1}{2}}^{-1}\boldsymbol{y}) \circ (\boldsymbol{G}_{\frac{1}{2},\frac{1}{2}}^{-1}\boldsymbol{y})^*]. \tag{B.32}$$

(iv) The relation between the circular autocorrelation and IDFT/IOFDFT power spectra is given by

$$\boldsymbol{r}_y^C = \boldsymbol{G}_{0,0}[(\boldsymbol{G}_{0,0}^{-1}\boldsymbol{y}) \circ (\boldsymbol{G}_{0,0}^{-1}\boldsymbol{y})^*] = \boldsymbol{G}_{0,0}[(\boldsymbol{G}_{\frac{1}{2},0}^{-1}\boldsymbol{y}) \circ (\boldsymbol{G}_{\frac{1}{2},0}^{-1}\boldsymbol{y})^*]. \tag{B.33}$$

*Proof:* We first represent (B.30) and (B.31) in Theorem 2 in generic form as

$$\boldsymbol{r}_x = \tfrac{1}{N}\boldsymbol{G}_{a,0}^{-1}[(\boldsymbol{G}_{a,b}\boldsymbol{x}) \circ (\boldsymbol{G}_{a,b}\boldsymbol{x})^*]. \tag{B.34}$$

By taking conjugate of both sides of (B.34) and using the property (B.2), we have

$$\boldsymbol{r}_x^* = \tfrac{1}{N^2}\boldsymbol{G}_{0,a}[(N\boldsymbol{G}_{b,a}^{-1}\boldsymbol{x}^*) \circ (N\boldsymbol{G}_{b,a}^{-1}\boldsymbol{x}^*)^*] = \boldsymbol{G}_{0,a}[(\boldsymbol{G}_{b,a}^{-1}\boldsymbol{x}^*) \circ (\boldsymbol{G}_{b,a}^{-1}\boldsymbol{x}^*)^*]. \tag{B.35}$$

Letting $\boldsymbol{x}$ be $\boldsymbol{y}^*$ in (B.35) yields

$$\boldsymbol{r}_{y^*}^* = \boldsymbol{G}_{0,a}[(\boldsymbol{G}_{b,a}^{-1}\boldsymbol{y}) \circ (\boldsymbol{G}_{b,a}^{-1}\boldsymbol{y})^*]. \tag{B.36}$$

Since $\boldsymbol{r}_{y^*}^* = \boldsymbol{r}_y$ in both circular and skew-circular autocorrelations, the proof is accomplished.

∎

Thus far, the relation between the periodic autocorrelation and GDFT power spectra has been connected in Theorem 2 and Corollary 2. These results are the theoretical fundamental of AR modeling of GDFT spectra in later derivation.

## B.2.2. AR Modeling with GDFT

An order-$P$ AR model for a period-$N$ GPS $\tilde{x}(n)$ with parameters $\alpha(1)$, $\alpha(2)$,…, $\alpha(P)$ is defined as

$$\tilde{x}(n) = -\sum_{k=1}^{P}\alpha(k)\tilde{x}(n-k) + \tilde{e}(n), \tag{B.37}$$

where $\tilde{e}(n)$ is a generalized-periodic excitation sequence, which is regarded as residuals in linear prediction sense. The residual term can be written as

$$\tilde{e}(n) = \sum_{k=0}^{N-1} \alpha(k)\tilde{x}(n-k) = \tilde{x}(n) \otimes \tilde{\alpha}(n),$$ (B.38)

where $\alpha(0) = 1$ and $\alpha(n) = 0$ for $n = P + 1, P + 2, \ldots, N - 1$. The periodic type of $\tilde{\alpha}(n)$ that is the GPS extended from $\alpha(n)$, $n = 0, 1, \ldots, N - 1$, must be the same as that of $\tilde{x}(n)$ to make the periodic convolution computable. Let $x, \alpha, e$ denote the representative vectors for $\tilde{x}(n)$, $\tilde{\alpha}(n)$, and $\tilde{e}(n)$, respectively. Then, by the convolution-multiplication properties (B.6)-(B.9), $e$ can be transformed into the GDFT frequency domain as

$$G_{a,b}e = (G_{a,b}x) \circ (G_{a,0}\alpha),$$ (B.39)

where $a$ and $b$ take on the values 0 or 1/2 depending on the periodicity type of $\tilde{x}(n)$ and the GDFT type used. Hence, by viewing $\tilde{e}(n)$ as a white noise, the power spectrum of the order-$P$ AR model is given by

$$\left|(G_{a,b}x)_k\right|^2 = \left|(G_{a,b}e)_k\right|^2 \left|(G_{a,0}\alpha)_k\right|^{-2} \approx \sigma_e^2 \cdot \left|(G_{a,0}\alpha)_k\right|^{-2}, \text{ for } k = 0, 1, \ldots, N - 1.$$ (B.40)

To evaluate the AR parameters, the Yule-Walker equations can be derived through the least square error (LSE) approach for the GDFT family. We present the result without proof.

**Theorem 3** For a GPS $\tilde{x}(n)$ with period $N$, the parameters for the order-$P$ AR modeling in the LSE criterion (i.e., minimize $\sum_{n=0}^{N-1}\left|\tilde{e}(n)\right|^2$) can be obtained by solving the Yule-Walker equations consisting of the periodic autocorrelations:

$$r_{\tilde{x}}(i) = -\sum_{n=1}^{P} r_{\tilde{x}}(i-n)\alpha(n), \text{ for } i = 1, 2, \ldots, P.$$ (B.41)

Furthermore, the LSE is given by

$$\sum_{n=0}^{N-1}\left|\tilde{e}(n)\right|^2 = N \cdot \sum_{n=0}^{P} r_{\tilde{x}}(-n)\alpha(n).$$ (B.42)

*Proof:* We first rewrite (B.41) in vector/matrix form as $e = x - X\alpha$ expressed as follows:

$$\begin{bmatrix} \tilde{e}(0) \\ \tilde{e}(1) \\ \tilde{e}(2) \\ \vdots \\ \tilde{e}(N-1) \end{bmatrix} = \begin{bmatrix} \tilde{x}(0) \\ \tilde{x}(1) \\ \tilde{x}(2) \\ \vdots \\ \tilde{x}(N-1) \end{bmatrix} + \begin{bmatrix} \tilde{x}(-1) & \tilde{x}(-2) & \tilde{x}(-3) & \cdots & \tilde{x}(-P) \\ \tilde{x}(0) & \tilde{x}(-1) & \tilde{x}(-2) & \cdots & \tilde{x}(1-P) \\ \tilde{x}(1) & \tilde{x}(0) & \tilde{x}(-1) & \cdots & \tilde{x}(2-P) \\ \vdots & \vdots & \vdots & \ddots & \vdots \\ \tilde{x}(N-2) & \tilde{x}(N-3) & \tilde{x}(N-4) & \cdots & \tilde{x}(N-P-1) \end{bmatrix} \begin{bmatrix} \alpha(1) \\ \alpha(2) \\ \alpha(3) \\ \vdots \\ \alpha(P) \end{bmatrix} \cdot \quad (B.43)$$

The parameter vector $\alpha$ corresponding to the LSE can be found through the normal equation:

$$- X^H X \alpha = X^H x . \quad (B.44)$$

The $(i, j)$ entry of $X^H X$ can be derived as follows:

$$[X^H X]_{i,j} = \sum_{k=1}^{N} [X^H]_{i,k} X_{k,j} = \sum_{k=1}^{N} \tilde{x}^*(k-i-1) \cdot \tilde{x}(k-j-1) = \sum_{m=-i}^{N-i-1} \tilde{x}^*(m) \cdot \tilde{x}(m+i-j) . \quad (B.45)$$

Since both $\tilde{x}^*(m)$ and $\tilde{x}(m+i-j)$ are either strictly periodic or anti-periodic with period $N$ when $i - j$ is fixed, by using Lemma 1, we have

$$[X^H X]_{i,j} = \sum_{m=0}^{N-1} \tilde{x}^*(m)\tilde{x}(m+i-j) = N \cdot r_{\tilde{x}}(i-j) , \text{ for } 1 \le i, j \le N. \quad (B.46)$$

Similarly, we have $(X^H x)_i = N \cdot r_{\tilde{x}}(i)$ for $1 \le i \le N$. Thus, (B.44) can be rewritten as (B.41).

Equation (B.42) can be derived by using (B.44). We ignore the details. ∎

Remarkable, in both strictly periodic and anti-periodic cases, the Yule-Walker equations can be expressed in terms of a Toeplitz matrix, and hence the Levinson-Durbin algorithm [53] can be used for efficiently computing AR parameters. Also, according to the next theorem, only $P + 1$ periodic autocorrelation entries, $r_{\tilde{x}}(i)$, $i = 0, 1, \ldots, P$, are required to comprise the Yule-Walker equations.

**Theorem 4** Let $\tilde{x}(n)$ be a GPS with period $N$. Then its periodic autocorrelation has the conjugate-symmetric property as

$$r_{\tilde{x}}(-n) = r_{\tilde{x}}^*(n) . \quad (B.47)$$

*Proof:* Applying Lemma 1 to $\tilde{x}^*(m)$ and $\tilde{x}(-n+m)$ leads to

$$N \cdot r_{\tilde{x}}(-n) = \sum_{m=0}^{N-1} \tilde{x}^*(m)\tilde{x}(-n+m) = \sum_{m=n}^{N+n-1} \tilde{x}^*(m)\tilde{x}(-n+m)$$
$$= \sum_{m=0}^{N-1} \tilde{x}^*(m+n)\tilde{x}(m) = N \cdot r_{\tilde{x}}^*(n). \tag{B.48}$$

∎

The next theorem describes the well-known Parseval's Theorem [52] for GDFTs.

**Theorem 5** Let $x$ be a column vector of length $N$. Then

$$\|x\|^2 = \tfrac{1}{N}\|G_{a,b}x\|^2 = N\|G_{a,b}^{-1}x\|^2 \quad \text{for } a, b = 0, 1/2. \tag{B.49}$$

∎

To summarize, like the traditional AR modeling method, the Yule-Walker equations in Theorem 3 can be solved to yield AR parameters in finite length problems. Then $|(G_{a,b}x)_k|^2$ can be estimated by $\sigma_e^2 |(G_{a,0}\alpha)_k|^{-2}$. By Theorem 5, we have $\sigma_e^2 \approx \tfrac{1}{N}\|G_{a,b}e\|^2 = \|e\|^2$. Also, $|(G_{a,0}x)_k| = |(G_{a,\frac{1}{2}}x)_k|$. Thus, when viewing $x$ in the strictly periodic sense, we can approximate its DFT and OTDFT power spectra by

$$|(G_{0,0}x)_k|^2 = |(G_{0,\frac{1}{2}}x)_k|^2 \approx \sigma_e^2 |(G_{0,0}\alpha)_k|^{-2} = \sigma_e^2 |(G_{0,\frac{1}{2}}\alpha)_k|^{-2}. \tag{B.50}$$

Oppositely, when viewing $x$ in the anti-periodic sense, we can approximate its OFDFT and O²DFT power spectra by

$$|(G_{\frac{1}{2},0}x)_k|^2 = |(G_{\frac{1}{2},\frac{1}{2}}x)_k|^2 \approx \sigma_e^2 |(G_{\frac{1}{2},0}\alpha)_k|^{-2} = \sigma_e^2 |(G_{\frac{1}{2},\frac{1}{2}}\alpha)_k|^{-2}. \tag{B.51}$$

Likewise, for the frequency-domain AR modeling, we can estimate the squared temporal envelope by

$$|(G_{0,b}^{-1}y)_n|^2 = |(G_{\frac{1}{2},b}^{-1}y)_n|^2 \approx N^{-2}\sigma_e^2 |(G_{0,b}^{-1}\alpha)_n|^{-2} = N^{-2}\sigma_e^2 |(G_{\frac{1}{2},b}^{-1}\alpha)_n|^{-2}. \tag{B.52}$$

where $b = 0$ or $1/2$ depending on the forward GDFT used, and $\sigma_e^2 \approx \tfrac{1}{N}\|G_{a,b}^{-1}e\|^2 = \tfrac{1}{N^2}\|e\|^2$. As an instance, Figure B.3 illustrates the spectral power envelopes of a speech segment of 2048

samples at 44.1 kHz. The power spectra obtained from its DFT and OFDFT are shown in Figure B.3 (b) and (c), where the spectral power envelopes of order-24 AR modeling are obtained by solving the Yule-Walker equations consisting of the circular and skew-circular autocorrelations, respectively. The two spectral power envelopes are depicted together in Figure B.3 (d) to compare their difference. In the low frequency part, the two envelopes are almost identical, whereas the major deviation occurs in the high frequency part and reveals the difference of the circular and skew-circular autocorrelations.
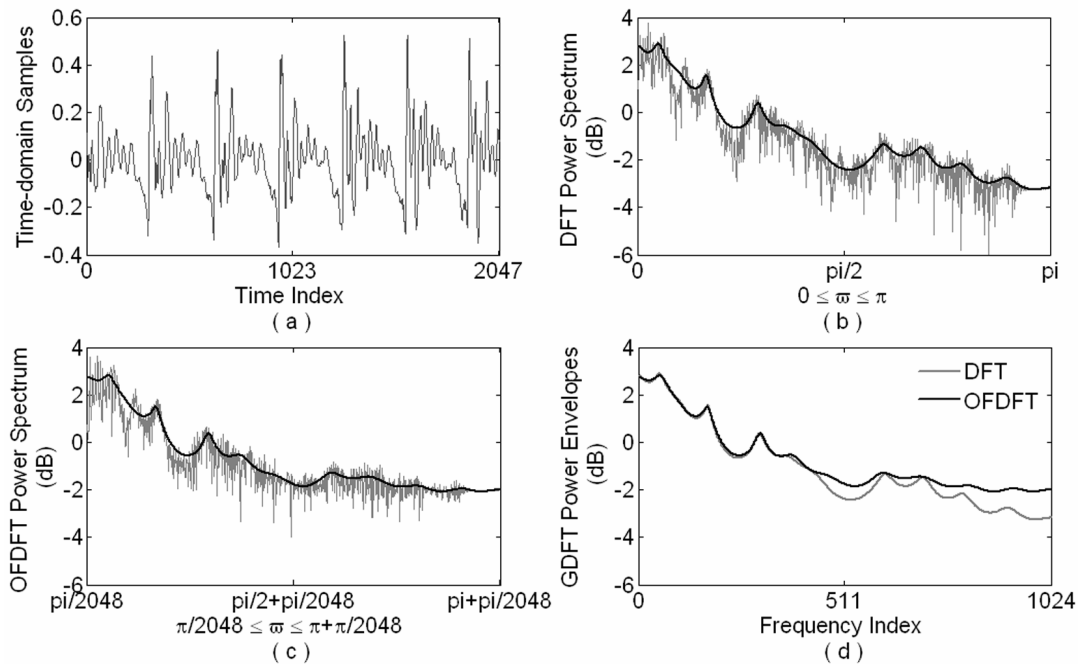


Figure B.3. Comparison of spectral power envelopes (i.e., squared envelope). (a) The time-domain speech segments of 2048 points at 44.1 kHz. (b) The DFT power spectrum and the spectral power envelope. (c) The OFDFT power spectrum and the spectral power envelope. Both the power envelopes are obtained by order-24 AR modeling, for which the Yule-Walker equations are comprised by the circular and skew-circular autocorrelations in (b) and in (c), respectively. (d) The comparison of the two power envelopes.

# B.3.   Autoregressive Modeling and DTT

In this section, we derive the theorems for the AR modeling in DTTs. First, associated with GDFTs, we derive the analytic transform matrices which convert real-valued vectors into analytic vectors. Then, based on the analytic vectors in DTT/IDTT, we derive the close form between DTT/IDTT with the GDFT/IGDFT. Combing the AR modeling in last section with the close form, we derive the AR modeling formulation with the DTTs in both temporal and spectral domains.

## B.3.1.   Analytic Transform based on GDFT and IGDFT

Marple has proposed a DFT-based method for computing the analytic signal corresponding to a finite real-valued sequence of an even length [79]. The $N \times N$ analytic transform matrix $A$ converting a real-valued vector $x$ into a complex-valued analytic vector $a$ is decomposed in matrix product form:

$$A = F^{-1}ZWZ^{T}F, \tag{B.53}$$

where $F$ denotes the DFT matrix, $Z$ denotes the zero-padding matrix $Z_{0,\,N/2+1,\,N/2-1}$, and $W$ is the weighting matrix $diag\{1,2,2,\ldots,2,1\}$ of order $N/2 + 1$. As can be seen, the analytic transformation proposed by Marple discards the negative DFT frequencies. With the appropriate weighting by $W$, the analytic vector can have two desired properties. First, the real part of $a$ exactly equals the original vector:

$$\mathrm{Re}(a_{n}) = x_{n}, \text{ for } n = 0, 1, \ldots, N - 1. \tag{B.54}$$

Second, the real and imaginary parts of $a$ are orthogonal:

$$\sum_{n=0}^{N-1}\mathrm{Re}(a_{n}) \cdot \mathrm{Im}(a_{n}) = 0. \tag{B.55}$$

As the fundamental for establishing the analytic transformation via the GDFT, we show

without proof the generalized symmetry of the GDFT of a real-valued input

**<u>Lemma 3</u>** Given a column vector $\boldsymbol{x}$ of length $M$, and $\boldsymbol{y} = \boldsymbol{G}_{a,b}\boldsymbol{x}$. Then $\boldsymbol{x}$ is real-valued if and

only if the following conjugate symmetric/anti-symmetric property of $\boldsymbol{y}$ holds.

(i) For DFT and OTDFT, i.e., $a = 0$,

$$\boldsymbol{y}_{\lceil M/2 \rceil + k} = s \cdot \boldsymbol{y}^{*}_{\lfloor M/2 \rfloor - k}, \text{ for } 0 \le k \le \lfloor M/2 \rfloor. \tag{B.56}$$

(ii) For OFDFT and O$^2$DFT, i.e., $a = 1/2$,

$$\boldsymbol{y}_{\lceil M/2 \rceil + k - 1} = s \cdot \boldsymbol{y}^{*}_{\lfloor M/2 \rfloor - k}, \text{ for } 0 \le k \le \lfloor M/2 \rfloor. \tag{B.57}$$

Here $s$ is 1 when $b = 0$ and $-1$ when $b = 1/2$.

*Proof:* Using the rule $M = \lceil M/2 \rceil + \lfloor M/2 \rfloor$, we can derive the generalized symmetric

properties of the basis functions of the GDFTs in (i) and (ii) in the frequency direction as

follows.

$$\exp\left(\frac{-j2\pi}{M}(\lceil M/2 \rceil + k)(n+b)\right) = \exp\left(\frac{-j2\pi}{M}(M - (\lfloor M/2 \rfloor - k))(n+b)\right)$$
$$= s \cdot \exp^{*}\left(\frac{-j2\pi}{M}(\lfloor M/2 \rfloor - k)(n+b)\right). \tag{B.58}$$

$$\exp\left(\frac{-j2\pi}{M}(\lceil M/2 \rceil + k - 1 + \tfrac{1}{2})(n+b)\right) = \exp\left(\frac{-j2\pi}{M}(M - (\lfloor M/2 \rfloor - k + \tfrac{1}{2})(n+b)\right)$$
$$= s \cdot \exp^{*}\left(\frac{-j2\pi}{M}(\lfloor M/2 \rfloor - k + \tfrac{1}{2})(n+b)\right). \tag{B.59}$$

Since a GDFT output is the linear combination of the basis functions of the GDFT by taking

the input vector as the combination coefficients, it has the same generalized symmetric

property as the basis functions have if the input vector is real-valued.

Conversely, we only consider the case of $a = 1/2$, and the case of $a = 0$ can be proved in

the same way. Let $\boldsymbol{x} = \boldsymbol{x}^{\text{Re}} + j\boldsymbol{x}^{\text{Im}}$, where $\boldsymbol{x}^{\text{Re}}$ and $\boldsymbol{x}^{\text{Im}}$ denote the real and imaginary parts of $\boldsymbol{x}$.

Let $\boldsymbol{z}^{\text{Re}} = \boldsymbol{G}_{\frac{1}{2},b}\boldsymbol{x}^{\text{Re}}$ and $\boldsymbol{z}^{\text{Im}} = \boldsymbol{G}_{\frac{1}{2},b}\boldsymbol{x}^{\text{Im}}$. Suppose $\boldsymbol{y}$ satisfies the condition (B.57). Of course,

$\boldsymbol{z}^{\text{Re}}$ has the same property as shown in the forward part. Thus, $j\boldsymbol{z}^{\text{Im}} = \boldsymbol{z} - \boldsymbol{z}^{\text{Re}}$ still satisfies

the condition (B.57), implying that $jz^{\text{Im}}_{\lceil M/2 \rceil + k - 1} = -s \cdot j(z^{\text{Im}}_{\lfloor M/2 \rfloor - k})^*$. However, since $\boldsymbol{x}^{\text{Im}}$ is

real-valued, we have $jz^{\text{Im}}_{\lceil M/2 \rceil + k - 1} = s \cdot j(z^{\text{Im}}_{\lfloor M/2 \rfloor - k})^*$. Thus, for $0 \le k \le \lfloor M/2 \rfloor$, $z^{\text{Im}}_{\lceil M/2 \rceil + k - 1} = 0$,

and then $z^{\text{Im}}_{\lfloor M/2 \rfloor - k} = 0$. This implies $x^{\text{Im}}_n = 0$ for all $n$, and hence $\boldsymbol{x}$ is real-valued. ∎

Based on the generalized symmetry of GDFTs, we can construct other analytic transform

matrices as shown in the next theorem.

**Theorem 6** Via each GDFT, we can define the analytic transform matrix, which satisfies both

the properties (B.54) and (B.55), in the generic form:

$$A^+_q = F^{-1}_q Z^+_q W^+_q (Z^+_q)^T F_q, \tag{B.60}$$

where $A^+_q$ is the $M \times M$ analytic transform matrix, $F_q$ is the GDFT matrix, $Z^+_q$ is the

zero-padding matrix, and $W^+_q$ is the weighting matrix. The specific matrices are tabulated in

Table IV, where $W^+_q$ belongs to one of the following diagonal matrices of order $N$ or $N + 1$

denoted as subscripts: $2\boldsymbol{I}_N = diag\{2, 2,..., 2\}$, $W^I_N = diag\{1, 2, 2,...,2\}$, $W^{II}_{N+1} = diag\{1, 2,$

$2,...,2, 1\}$, and $W^{III}_N = diag\{2, 2,...,2, 1\}$.

*Proof:* In the same approach in [79], we can construct the analytic vector by defining the

conjugate symmetric and anti-symmetric functions. For example, we consider the

construction of odd $A^+_{III}$. Let $\boldsymbol{y} = \boldsymbol{G}_{\frac{1}{2},0}\boldsymbol{x}$ and $\boldsymbol{a} = \boldsymbol{a}^{\text{Re}} + j\boldsymbol{a}^{\text{Im}} = A^{o+}_{III}\boldsymbol{x}$ for a real-valued vector

$\boldsymbol{x}$ of length $M$, where $\boldsymbol{a}^{\text{Re}}$ and $\boldsymbol{a}^{\text{Im}}$ denote the real and imaginary parts of $\boldsymbol{a}$. Let $\boldsymbol{z}^{\text{Re}}$ and $\boldsymbol{z}^{\text{Im}}$

denote the OFDFTs of $\boldsymbol{a}^{\text{Re}}$ and $\boldsymbol{a}^{\text{Im}}$, respectively. For the condition (B.54), we must define

$\boldsymbol{z}^{\text{Re}} = \boldsymbol{y}$ to have $\boldsymbol{a}^{\text{Re}} = \boldsymbol{x}$. On the other hand, we define

$$(\boldsymbol{z}^{\text{Im}})_k = \begin{cases} -j \cdot \boldsymbol{y}_k & 0 \le k \le (M-1)/2 \\ 0 & k = (M+1)/2 \\ j \cdot \boldsymbol{y}_k & (M+3)/2 \le k \le M-1 \end{cases}. \tag{B.61}$$

Note that adding $z^{\text{Re}}$ to $jz^{\text{Im}}$ not only eliminates the negative spectrum but also leads to the definition of $W_{III}^{o+}$ as $diag\{2, 2,\ldots,2, 1\}$ of order $(M+1)/2$. The definition (B.61) indeed implies that $a^{\text{Im}} = G_{\frac{1}{2},0}^{-1}z^{\text{Im}}$ is purely real-valued since the conjugate symmetric property (B.57) holds; thus, the condition (B.54) is satisfied. The orthogonal property (B.55) can be confirmed as follows:

$$(a^{\text{Re}})^T a^{\text{Im}} = \tfrac{1}{M}(G_{\frac{1}{2},0}a^{\text{Re}})^H (G_{\frac{1}{2},0}a^{\text{Im}}) = \tfrac{1}{M}(z^{\text{Re}})^H z^{\text{Im}} = 0. \tag{B.62}$$

In the last step, the conjugate symmetric property of $y$ is used. Other analytic transform matrices can be constructed in the same way. ∎

In the next corollary, we show the dual formula of (B.60).

**<u>Corollary 3</u>** Let $A_q^- = (A_{\Phi(q)}^+)^*$, $Z_q^- = Z_{\Phi(q)}^+$, and $W_q^- = W_{\Phi(q)}^+$. We can define the analytic transform matrix which converts a real-valued spectral vector into a spectral analytic vector as

$$A_q^- = F_q Z_q^- W_q^- (Z_q^-)^T F_q^{-1}. \tag{B.63}$$

*Proof:* We take conjugate of (B.60) and use the property (B.2) to have

$$(A_q^+)^* = F_{\Phi(q)} Z_q^+ W_q^+ (Z_q^+)^T F_{\Phi(q)}^{-1}. \tag{B.64}$$

Then replacing $q$ by $\Phi(q)$ yields

$$(A_{\Phi(q)}^+)^* = F_q Z_{\Phi(q)}^+ W_{\Phi(q)}^+ (Z_{\Phi(q)}^+)^T F_q^{-1}. \tag{B. 65}$$

∎

Take for example, let $x = [1, -2, -3, 7, 11]^T$, we have

$$A_{II}^{o+}x = [1+ j6.5489, -2 + j1.8809, -3 - j4.0867, 7 - j8.1816, 11 + j3.8385]^T,$$

$$A_{III}^{o+}x = [1- j6.1211, -2 - j0.1534, -3 - j6.9929, 7 - j8.7628, 11 + j4.1978]^T,$$

and $A_{II}^{o-}x = (A_{III}^{o+}x)^*$. Figure B.4 depicts pictorially the reconstruction of analytic transforms defined in Theorem 6 and Corollary 3.

Table B.5.Definitions of Related Matrices for Analytic Transform

| | $A_q^+$ | $F_q$ | $Z_q^+$ | $W_q^+$ | $A_q^-$ | $F_q^{-1}$ | $Z_q^-$ | $W_q^-$ |
|---|---|---|---|---|---|---|---|---|
| **M = 2N** | $A_I^{e+}$ | $G_{0,0}$ | $Z_{0,N+1,N-1}$ | $W_{N+1}^{II}$ | $A_I^{e-}$ | $G_{0,0}^{-1}$ | $Z_{0,N+1,N-1}$ | $W_{N+1}^{II}$ |
| | $A_{II}^{e+}$ | $G_{0,\frac{1}{2}}$ | | $W_{N+1}^{II}$ | $A_{II}^{e-}$ | $G_{0,\frac{1}{2}}^{-1}$ | $Z_{0,N,N}$ | $2I_N$ |
| | $A_{III}^{e+}$ | $G_{\frac{1}{2},0}$ | $Z_{0,N,N}$ | $2I_N$ | $A_{III}^{e-}$ | $G_{\frac{1}{2},0}^{-1}$ | $Z_{0,N+1,N-1}$ | $W_{N+1}^{II}$ |
| | $A_{IV}^{e+}$ | $G_{\frac{1}{2},\frac{1}{2}}$ | | $2I_N$ | $A_{IV}^{e-}$ | $G_{\frac{1}{2},\frac{1}{2}}^{-1}$ | $Z_{0,N,N}$ | $2I_N$ |
| **M = 2N − 1** | $A_I^{o+}$ | $G_{0,0}$ | $Z_{0,N,N-1}$ | $W_N^I$ | $A_I^{o-}$ | $G_{0,0}^{-1}$ | $Z_{0,N,N-1}$ | $W_N^I$ |
| | $A_{II}^{o+}$ | $G_{0,\frac{1}{2}}$ | | $W_N^I$ | $A_{II}^{o-}$ | $G_{0,\frac{1}{2}}^{-1}$ | | $W_N^{III}$ |
| | $A_{III}^{o+}$ | $G_{\frac{1}{2},0}$ | | $W_N^{III}$ | $A_{III}^{o-}$ | $G_{\frac{1}{2},0}^{-1}$ | | $W_N^I$ |
| | $A_{IV}^{o+}$ | $G_{\frac{1}{2},\frac{1}{2}}$ | | $W_N^{III}$ | $A_{IV}^{o-}$ | $G_{\frac{1}{2},\frac{1}{2}}^{-1}$ | | $W_N^{III}$ |
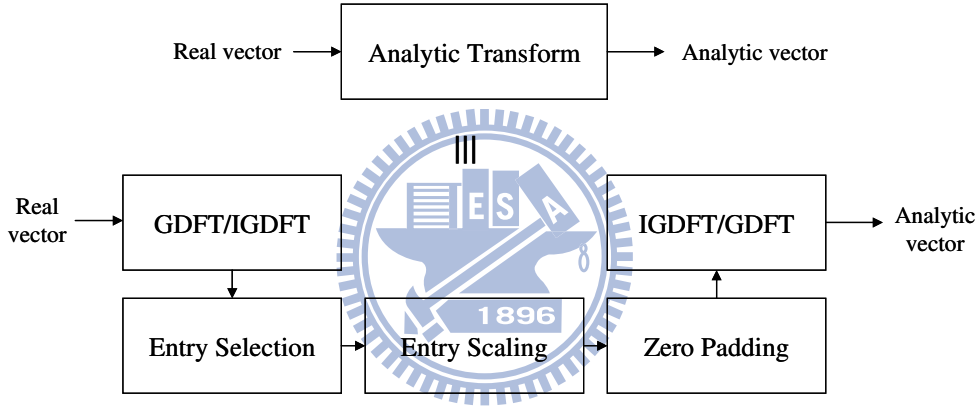


Figure B.4. Reconstruction of analytic transform.

## B.3.2. DTT and Analytic Transform

The next theorem illustrates the interpretation of DTT spectra as the GDFT spectra of analytic vectors.

**Theorem 7** Given a temporal column vector $x$ and $y = T_q x$. Then the IGDFT of the zero-padded and scaled DTT equals the analytic transformation of the symmetrized temporal vector, that is,

$$A_q^+ (E_q x) = F_q^{-1} (Z_q W_q'^+ y),$$

(B.66)

where the related matrices are defined in Table II.

*Proof:* To relate the DTT and the analytic transform, we combine the generic formulas (B.12) and (B.60) into the form:

$$A_q^+(E_q x) = F_q^{-1} Z_q^+ W_q^+ (Z_q^+)^T F_q E_q x = F_q^{-1} Z_q^+ W_q^+ (Z_q' T_q x) = F_q^{-1}(Z_q W_q'^+ y). \tag{B.67}$$

In the second step, the purpose of zero-padding matrix $Z_q'$ is to gather the inherent zero output at the boundary indices of $T_q$ to make up the total output length of $N$ or $N + 1$. The matrix product $Z_q^+ W_q^+ Z_q'$ can be rewritten as $Z_q^+ Z_q' W_q'^+$, where $W_q'^+$ is obtained from $W_q^+$ by removing the boundary diagonal terms and reducing the order if necessary. Also, $Z_q^+ Z_q'$ can pad the DTT output to fill the lengths $2N$ and $2N - 1$ for the even and odd cases, respectively; hence, $Z_q^+ Z_q'$ equals $Z_q$, and the last step is arrived. ∎

Remarkably, when combined with DST, the $F_q$ and $F_q^{-1}$ associated with $A_q^+$ should be scaled by $j$ and $-j$, and the derivation above has no affection. In the dual manner, the next corollary illustrates the interpretation of temporal vectors as the IGDFT of DTT-domain analytic vectors.

**<u>Corollary 4</u>** Given a spectral column vector $y$ and $x = T_q^{-1} y$. Then the GDFT of the zero-padded and scaled temporal vector equals the analytic transformation of the symmetrized DTT vector. That is,

$$A_q^-(E_q' y) = F_q(Z_{\Phi(q)} W_q'^- x), \tag{B.68}$$

where the related matrices are defined in Table III.

*Proof:* By Theorem 7 and the properties $(A_q^-)^* = A_{\Phi(q)}^+$ and $E_{\Phi(q)} = E_q'$, we have

$$[A_q^-(E_q' y)]^* = A_{\Phi(q)}^+(E_{\Phi(q)} y) = F_{\Phi(q)}^{-1}(Z_{\Phi(q)} W_{\Phi(q)}'^+ T_{\Phi(q)} y). \tag{B.69}$$

Then, by taking conjugate again and using the property $W_q'^- = W_{\Phi(q)}'^+$ due to $W_q^- = W_{\Phi(q)}^+$,

the dual formula for IDTT is derived as

$$A_q^-(E_q'y) = F_q(Z_{\Phi(q)}W_{\Phi(q)}'^+T_q^{-1}y) = F_q(Z_{\Phi(q)}W_q'^-x).$$ (B.70)

∎

The dual formulas (B.66) and (B.68) describe how a vector is related to its DTT and IDTT in the sense of analytic transformation through appropriate symmetrization, zero-padding and weighting operations.
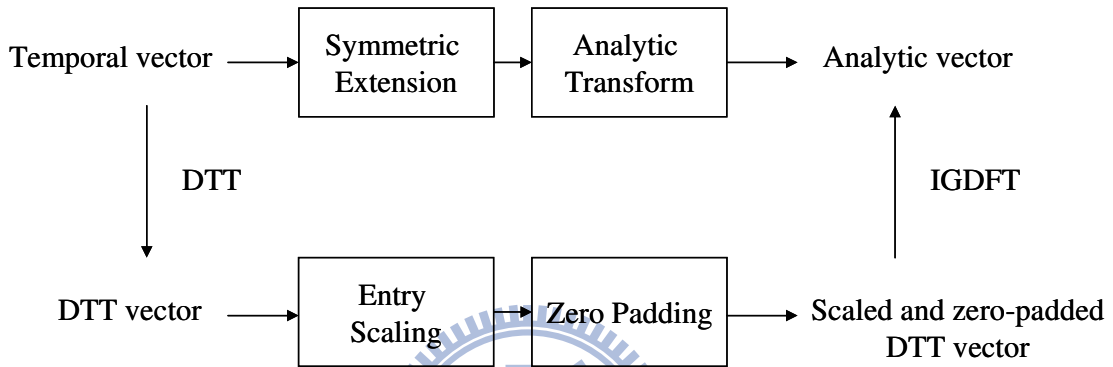


Figure B.5. A pictorial representation of (B.66).
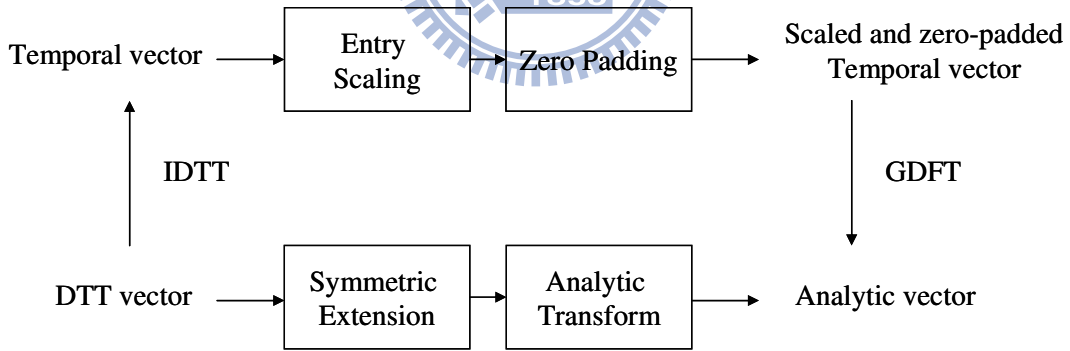


Figure B.6. A pictorial representation of (B.66).

## B.3.3.   Autocorrelation and Squared Hilbert Envelope

Thanks to Corollary 2, we have linked the GDFT-domain periodic autocorrelation with the IGDFT-domain (temporal) envelope. Combining the corollary with Theorem 7, we can immediately obtain the time-frequency relation between the DTT-domain periodic

autocorrelation and the Hilbert envelope (i.e., the magnitude envelope of the analytic signal) for a time-domain finite sequence.

**<u>Theorem 8</u>** Given a temporal real-valued vector $x$ and $y = T_q x$. Let $\hat{y} = Z_q W_q^{\prime+} y$, then

$$r_{\hat{y}} = K_q[(A_q^+ E_q x) \circ (A_q^+ E_q x)^*],$$ (B.71)

where $r_{\hat{y}}$ is the circular or skew-circular autocorrelation of $\hat{y}$ depending on the type of $K_q$ that is a DFT or OTDFT matrix. (The specific types of transform and autocorrelation are defined in Table II, where notations (c) and (s) denote the circular and skew-circular autocorrelations, respectively.)

*Proof:* From Theorem 7, we have $F_q^{-1} \hat{y} = A_q^+ E_q x$ ; by Corollary 2, the proof is accomplished.

■

The next theorem gives the dual formulation for estimating the spectral Hilbert envelope.

**<u>Theorem 9</u>** Given a spectral real-valued vector $y$ and $x = T_q^{-1} y$. Let $\hat{x} = Z_{\Phi(q)} W_{\Phi(q)}^{\prime+} x$, then

$$r_{\hat{x}} = \tfrac{1}{M} \Gamma_q^{-1}[(A_q^- E_q' y) \circ (A_q^- E_q' y)^*],$$ (B.72)

where $r_{\hat{x}}$ is the circular or skew-circular autocorrelation of $\hat{x}$ depending on the type of $\Gamma_q^{-1}$ that is a IDFT or IOFDFT matrix; and the scale factor $M$ is the length of $\hat{x}$. (The specific types of transform and autocorrelation are defined in Table III.)

*Proof:* From Corollary 4, we have $F_q \hat{x} = A_q^- E_q' y$ ; by Theorem 2, the proof is accomplished.

■

Theorems 8 and 9 permit to model the squared temporal or spectral Hilbert envelope of the symmetrized time-domain or DTT-domain vector by fitting an AR model to the zero-padded and weighted vector in the dual domain. The AR parameters obtained by the Yule-Walker equations should be zero-padded to length $M$ and transformed by $F_q$ and $F_q^{-1}$ , respectively, for the spectral and temporal envelope estimation.

## B.3.4.   Autocorrelation and DTT Power Envelope

Rather than the squared Hilbert envelope, we may be interested in modeling the squared DTT spectrum (i.e., evaluating the DTT power envelope). This can be achieved by applying the periodic autocorrelation analysis to the symmetrized data vector, instead of the zero-padded and scaled data vector.

**Theorem 10** Given a spectral real-valued vector $y$ and $x = T_q^{-1} y$. Let $\ddot{x} = E_q x$, then

$$r_{\ddot{x}} = \tfrac{1}{M} \boldsymbol{\Gamma}_q^{-1} [(E_q' y) \circ (E_q' y)], \tag{B.73}$$

where $r_{\ddot{x}}$ is the circular or skew-circular autocorrelation of $\ddot{x}$ depending on the type of $\boldsymbol{\Gamma}_q^{-1}$; and $M$ is the length of $\ddot{x}$. (The specific types of transform and autocorrelation are defined in Table III.)

*Proof:* From (B.13), it implies $F_q E_q x = E_q' T_q x = E_q' y$; by Theorem 2, the proof is accomplished. ∎

Oppositely, the next theorem provides the fundamental for estimating the temporal power envelope.

**Theorem 11** Given a temporal real-valued vector $x$ and $y = T_q x$. Let $\ddot{y} = E_q' y$, then

$$r_{\ddot{y}} = K_q [(E_q x) \circ (E_q x)], \tag{B. 74}$$

where $r_{\ddot{y}}$ is the circular or skew-circular autocorrelation of $\ddot{y}$ depending on the type of $K_q$. (The specific types of transform and autocorrelation are defined in Table II.)

*Proof:* From (B.14), it implies $F_q^{-1} E_q' y = E_q T_q^{-1} y = E_q x$; by Corollary 2, the proof is accomplished. ∎

The dual formulas in Theorems 10 and 11 permit to estimate the temporal or spectral power envelope of the symmetrized time-domain or DTT-domain vector by fitting an AR

model to the symmetrized vector in the dual domain.

## B.3.5.   Remarks and Examples

We notice that the periodic autocorrelation of the zero-padded samples is equivalent to the linear correlation used in the autocorrelation method [64] for linear prediction. Therefore, the traditional autocorrelation method with scaling can be interpreted as the Hilbert envelope estimation of the DTT/IDTT spectrum as illustrated in Theorems 8 and 9. However, looking at the time-domain AR modeling in Theorems 9 and 10, the squared spectral Hilbert envelope and the spectral power envelope will be close when the time-domain input signal is steady and the order of AR modeling is much smaller than the length of the input segment. The phenomenon can be interpreted by the approximate results of periodic autocorrelation $r_{\ddot{x}}$ and $r_{\hat{x}}$ in that condition. Likewise, when a windowing operation, such as sine windowing, is applied to the input samples, the aliasing part of periodic autocorrelation becomes small; hence, the resultant spectral Hilbert or power envelopes of all the DTTs do not have significant difference. On the other hand, the difference of the two kinds of envelopes are easier to be observed in the frequency-domain AR modeling because the frequency coefficients in the DTT domain are usually unsteady and have large energy variation in low-frequency part. In AR modeling, we can expect the temporal Hilbert envelop should be more smooth due to the imagery part added by the analytic transform, while the power envelope can fit the temporal samples better in the LSE sense.

In the following, we provide some examples to illustrate the remarks. Figure B.7 compares two approaches on a time-domain audio segment of 1024 samples at 44.1 kHz for evaluating spectral envelopes. In Figure B.7 (b) the skew-circular autocorrelations of the zero-padded and scaled time-domain samples are used to evaluate the spectral Hilbert envelope of the symmetrized odd DST-IV spectrum, while in Figure B.7 (c) the skew-circular autocorrelations of the symmetrized time-domain samples are used to evaluate the spectral

power envelope fitting the squared of the symmetrized odd DST-IV spectrum. The order of AR modeling in the two cases is 24. Note that the squared envelopes corresponding to AR models in Figure B.7 (b) and (c) are computed by squaring the length-2048 O$^2$DFT (or OFDFT) of AR parameters. In Figure B.7 (d), the two squared envelopes are depicted together with the squared odd DST-IV spectrum for comparison. Since $\left\|\ddot{\boldsymbol{x}}\right\|^2 \approx \frac{1}{2}\left\|\hat{\boldsymbol{x}}\right\|^2$, the estimated envelope from the zero-padded and scaled samples should have energy alignment by 1/2 when compared with the squared DTT spectrum. As can be seen, the envelopes associated with (b) and (c) are highly close. The observation can be interpreted from the approximation of the two skew-circular autocorrelations, especially when the predictive order is much smaller than the sample number.

As an instance of the frequency-domain AR modeling of order 24 on the length-1024 even DCT-IV spectrum, Figure B.8 (b) and (c) show the squared temporal Hilbert envelope and the temporal power envelope, respectively. In Figure B.9, in addition to the two envelopes in Figure B.8, the two kinds of temporal envelope evaluated from the odd DCT-I spectrum of the same time-domain segment are also depicted. Here the Hilbert envelopes through AR modeling have energy alignment by 1/2. The temporal envelopes are evaluated from the length-2048 IO$^2$DFT (or IOTDFT) of AR parameters for even DCT-IV and from the length-2048 IDFT (or IOFDFT) of AR parameters for odd DCT-I, respectively. As can be seen, the two Hilbert envelopes have minor deviation since the corresponding analytic signals are similar but different in magnitude, while the other two envelopes are too close to distinguish because they are corresponding to the squared time-domain samples which are symmetrized by $\boldsymbol{E}_{HSHA}$ and $\boldsymbol{E}_{HAWS}$, respectively, and only differ by one zero sample. We note that the temporal envelope evaluated from the symmetrized frequency data can fit well the time-domain audio segment in LSE sense and fit the valley better than the Hilbert envelope does. Figure B.10 illustrates another instance, where an even DCT-IV spectrum of length

119

2048, which has strong low-frequency sinusoid component, is analyzed by the AR modeling of order 50. In Figure B.10 (d), the Hilbert envelope without energy alignment fits the peaks of the magnitude of the sinusoid component in the segment, while the square-root power envelop leads to a saw-tooth response. Since $\lim_{T \to \infty} \frac{1}{T} \int_0^T a^2 \cos^2(\omega t) dt = \frac{a^2}{2}$, the ratio of the energy and the squared amplitude of a sinusoid is 1/2; hence, the Hilbert envelope without energy alignment in this example can well fit the peaks of the sinusoid component.
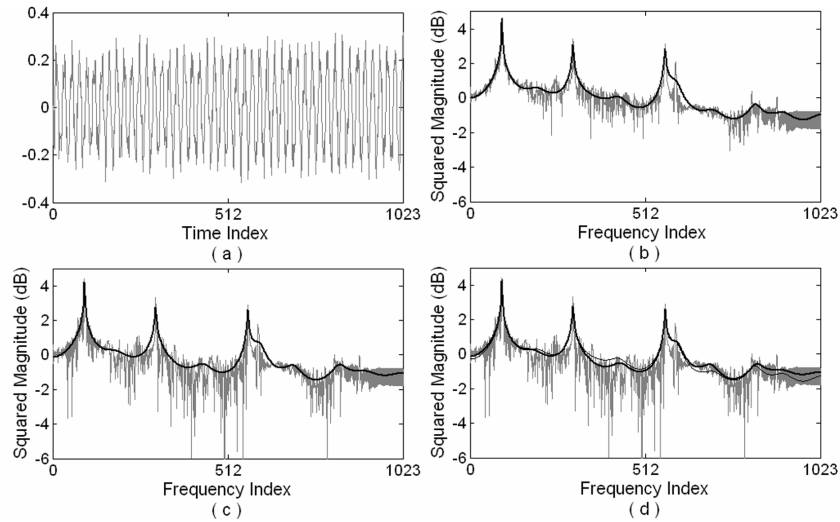


Figure B.7. Comparison of squared spectral envelopes. (a) The time-domain audio segment of 1024 samples at 44.1 kHz. (b) The squared analytic transform of the odd DST-IV spectrum and the squared Hilbert envelope through AR modeling. (c) The squared odd DST-IV spectrum and the power envelope. (d) The power envelope (thick line), the squared Hilbert envelope with energy alignment (thin line), and the squared odd DST-IV spectrum. Both the squared spectral envelopes are obtained by order-24 AR modeling. Only positive spectra are depicted in (b)-(d) due to symmetry.
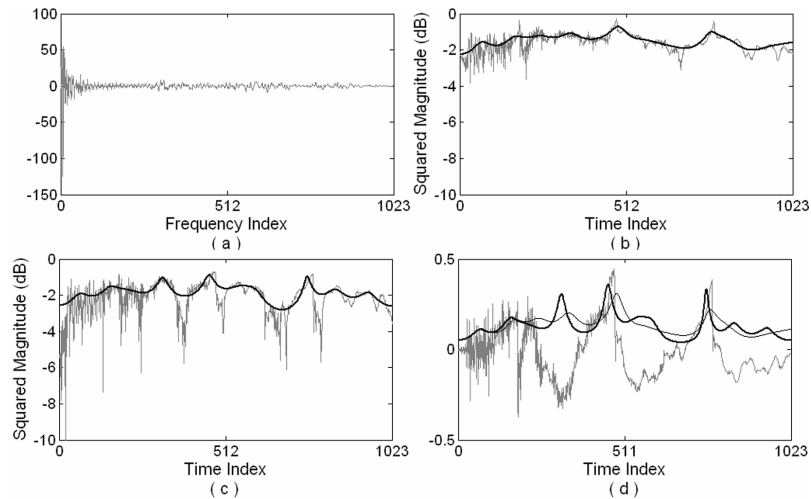
Figure B.8. Comparison of squared temporal envelopes. (a) The even DCT-IV coefficients of an audio segment of 1024 samples at 44.1 kHz. (b) The squared analytic transform of the symmetrized time-domain samples and the squared temporal Hilbert envelope through AR modeling. (c) The squared symmetrized time-domain samples and the temporal power envelope. (d) The time-domain samples and the two (non-squared) envelopes depicted in linear scale. The two squared temporal envelopes are obtained by order-24 AR modeling. The symmetrized parts are not depicted in (b)-(d).
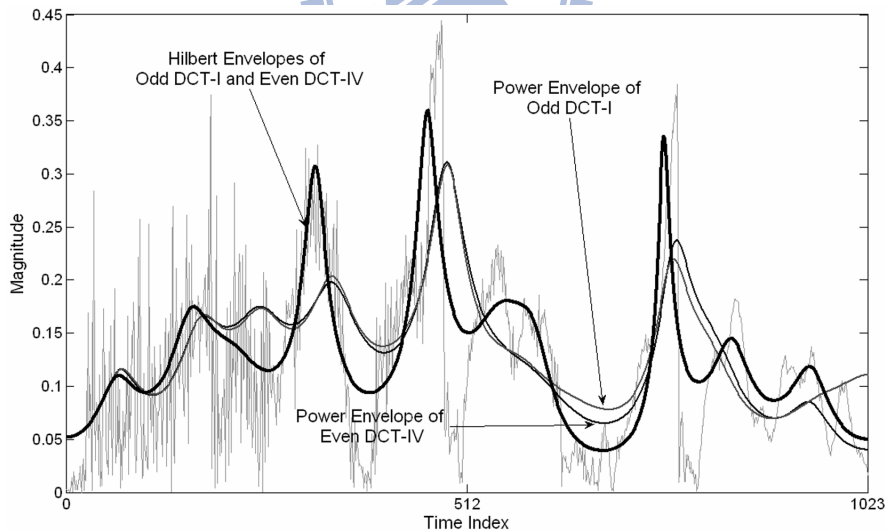


Figure B.9. Comparison of temporal envelopes evaluated from even DCT-IV and odd DCT-I coefficients, where the two (non-squared) envelopes and the magnitude of the time-domain samples in Figure B.8 are depicted in linear scale. Furthermore, the two envelopes evaluated from odd DCT-I coefficients are shown for comparison. Note that the two envelopes corresponding to the squared symmetrized time-domain samples are too close to distinguish.

121
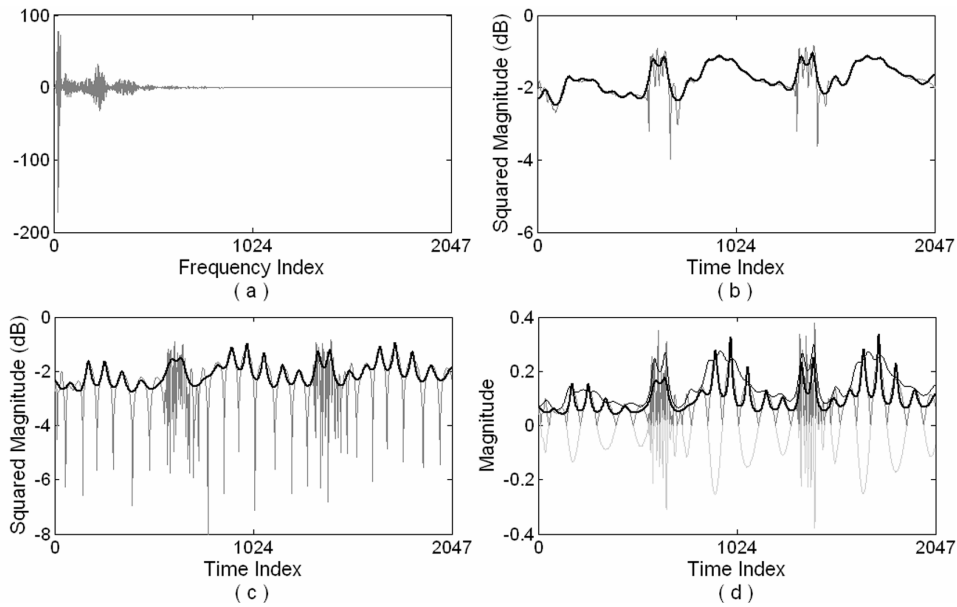
Figure B.10. Comparison of squared temporal envelopes. (a) The even DCT-IV coefficients of an audio segment of 2048 samples at 44.1 kHz. (b) The squared analytic transform of the symmetrized time-domain samples and the squared temporal Hilbert envelope through AR modeling. (c) The squared symmetrized time-domain samples and the temporal power envelope. (d) The time-domain samples, its magnitude, the square-root power envelopes (thick line), and the Hilbert envelope without energy alignment are depicted in linear scale. The two temporal envelopes are obtained by order-50 AR modeling.

# APPENDIX C

# EVALUATION FOR ZEROS OF

# FIRST/SECOND-ORDER LP FILTERS ON

# ANALYTIC SIGNALS

## C.1. Proof of Three Integrations

By using the trigonometric properties $\sin(\alpha - \beta) = \sin(\alpha)\cos(\beta) - \cos(\alpha)\sin(\beta)$ and $\cos(\alpha - \beta) = \cos(\alpha)\cos(\beta) + \sin(\alpha)\sin(\beta)$, (71) and (72) can be rewritten as

$$A(\tilde{\theta}) = \cos(\tilde{\theta} - \theta_0)S - \sin(\tilde{\theta} - \theta_0)C = 0, \tag{C.1}$$

$$B(\tilde{r}, \tilde{\theta}) = \cos(\tilde{\theta} - \theta_0)C + \sin(\tilde{\theta} - \theta_0)S - \tilde{r}K = 0, \tag{C.2}$$

where three integrations $S$, $C$, and $K$ are defined as

$$S = \int_0^\pi \frac{\sin(\omega - \theta_0)}{1 - 2r_0 \cos(\omega - \theta_0) + r_0^2} d\omega, \tag{C.3}$$

$$C = \int_0^\pi \frac{\cos(\omega - \theta_0)}{1 - 2r_0 \cos(\omega - \theta_0) + r_0^2} d\omega, \tag{C.4}$$

$$K = \int_0^\pi \frac{1}{1 - 2r_0 \cos(\omega - \theta_0) + r_0^2} d\omega. \tag{C.5}$$

First consider the evaluation of integration $K$:

$$K = \int_0^\pi \frac{1}{1 - 2r_0 \cos(\omega - \theta_0) + r_0^2} d\omega = \int_{-\theta_0}^{\pi - \theta_0} \frac{1}{1 - 2r_0 \cos(\omega) + r_0^2} d\omega. \tag{C.6}$$

Note that we assume $0 < r_0 < 1$ and $0 \le \theta_0 \le \pi$. We might write

$$K = \int_\Omega \frac{1}{1 - 2r_0 \cdot \frac{1}{2}\left(z + \frac{1}{z}\right) + r_0^2} \frac{dz}{jz} = \frac{j}{r_0^2 - 1}\left(\int_\Omega \frac{1}{z - r_0} dz - \int_\Omega \frac{1}{z - r_0^{-1}} dz\right), \tag{C.7}$$

where path $\Omega$ is the upper arc of the unit circle which is from $e^{-j\theta_0}$ to $e^{j(\pi-\theta_0)}$. Since $K$ is real, (C.7) can be rewritten as

$$K = \frac{1}{1-r_0^2}\left[ \mathrm{Im}\left( \int_\Omega \frac{1}{z-r_0}\,dz \right) - \mathrm{Im}\left( \int_\Omega \frac{1}{z-r_0^{-1}}\,dz \right) \right]. \tag{C.8}$$

Using the formula $\log(z-r_0) = \log|z-r_0| + j\arg(z-r_0)$, the first integration can be evaluated as

$$\mathrm{Im}\int_\Omega \frac{1}{z-r_0}\,dz = \arg[\cos(\pi-\theta_0) - r_0 + j\sin(\pi-\theta_0)] - \arg[\cos(-\theta_0) - r_0 + j\sin(-\theta_0)]. \tag{C.9}$$

In (C.9), we can choose the branch with $-\pi < \arg(z-r_0) < \pi$ such that $\log(z-r_0)$ is analytic in the domain $\{z \in \mathbf{C} - \{r_0\} \mid -\pi < \arg(z-r_0) < \pi\}$ containing $\Omega$. Then, in terms of the arc tangent function *arctan* that is with range of $(-\pi/2, \pi/2)$, the integration in (C.9) can be rewritten as $T$ defined in (78). Similarly, we can choose the branch with $0 < \arg(z-r_0^{-1}) < 2\pi$ such that $\log(z-r_0^{-1})$ is analytic in the domain $\{z \in \mathbf{C} - \{r_0^{-1}\} \mid 0 < \arg(z-r_0^{-1}) < 2\pi\}$ containing $\Omega$. Subsequently, we have

$$\mathrm{Im}\int_\Omega \frac{1}{z-r_0^{-1}}\,dz = -\arctan\left( \frac{\sin(\theta_0)}{\cos(\theta_0)+r_0^{-1}} \right) + \arctan\left( \frac{\sin(\theta_0)}{\cos(\theta_0)-r_0^{-1}} \right). \tag{C.10}$$

Substituting the two close forms of (C.9) and (C.10) into (C.8) yields (77). On the other hand, from the integral identity $\int_0^\pi \dfrac{1-2r_0\cos(\omega-\theta_0)+r_0^2}{1-2r_0\cos(\omega-\theta_0)+r_0^2}\,d\omega = \pi$, we can evaluate $C$ as (76).

Equation (75) can be derived by the technique of changing valuables. Thus, from (C.1), the angle of the zero of the MMSE predictive filter is given as (73). By substituting (73) into (C.2), the radius of the zero of the MMSE predictive filter is derived as (74).

## C.2.    Proof of Zeros

To find the MMSE solution of (80), from the geometric symmetry of the solution, we might assume that $\tilde{r}_1 = \tilde{r}_2 = r$, $\tilde{\theta}_1 = \theta$, $\tilde{\theta}_2 = \pi - \theta$ and $\theta \in [0, \pi/2]$. Then we can evaluate the integration in (80) as

$$(1 + 2r^2 - 2r^2 \cos(2\theta) + r^4)\pi - 8(r + r^3)\sin(\theta). \qquad (C.11)$$

Deriving $\partial F/\partial\theta = 0$ and $\partial F/\partial r = 0$ yields, respectively,

$$r[1 + r^2 - \cos(2\theta)]\pi - 2(1 + 3r^2)\sin(\theta) = 0, \qquad (C.12)$$

$$1 + r^2 = r\pi \sin(\theta). \qquad (C.13)$$

Repeatedly substituting (C.13) into (C.12) to reduce the power of term $r$ from 2 to 1 and using the trigonometric property $2\sin^2(\theta) + \cos(2\theta) = 1$ can give

$$r = \frac{\pi}{(\pi^2 - 4)\sin(\theta)}. \qquad (C.14)$$

We can obtain $\theta$ by substituting (C.14) into (C.13) as

$$\sin(\theta) = \frac{\pi}{2\sqrt{\pi^2 - 4}}; \qquad (C.15)$$

then substituting (C.15) into (C.14) yields (81). Similarly, by repeatedly substituting (C.12) and using the trigonometric property $2\sin^2(\theta) + \cos(2\theta) = 1$, we can derive (C.11) as

$$F(r,\theta) = r^2\pi[\pi^2 \sin^2(\theta) - 2\cos(2\theta)] - 8[r^2\pi \sin^2(\theta)]. \qquad (C.16)$$

By substituting (C.15) and (81) into (C.16), we can obtain the MMSE as $\pi(\pi^2 - 8)/(\pi^2 - 4)$.

# BIBLIOGRAPHY

[1] *Information Technology—Coding of Moving Pictures and Associated Audio for Digital Storage Media at Up to 1.5 mps- CD11172 (Part 3, Audio)*, ISO/IEC JTCI/SC29/WG1/N71, ISO/IEC, 1992.

[2] *Coding of Moving Pictures and Audio—IS 13818-7 (MPEG-2 Advanced Audio Coding, AAC)*, ISO/IEC JTC1/SC29/WG11/N1650, ISO/IEC, 1997.

[3] *Information Technology—Coding of Audiovisual Objects*, ISO/IEC CD 14496 (Part 3, Audio), ISO/IEC, 1999.

[4] ATSC A/52, *Digital Audio Compression (AC-3) Standard*, United States Advanced Television Systems Committee.

[5] *Bandwidth Extension*, ISO/IEC JTC1/SC29/WG11/N5570, ISO/IEC, 14496-3:2001/FDAM1, Pattaya, Thailand, Mar. 2003.

[6] M. Dietz, L. Liljeryd, K. Kjörling, and O. Kunz, "Spectral band replication, a novel approach in audio coding," in *Proc. AES 112nd Conv.*, Munich, Germany, May 2002, preprint 5553.

[7] M. Wolters, K. Kjörling, D. Homm, and H. Purnhagen, "A closer look into MPEG-4 high efficiency AAC," in *Proc. AES 115th Conv.*, New York, USA, Oct. 2003, preprint 5871.

[8] P. Ekstrand, "Bandwidth extension of audio signals by spectral band replication," in *Proc. 1st IEEE Benelux Workshop on Model Based Process. Coding Audio*, Leuven, Belgium, Nov. 2002, pp. 53-58.

[9] *"3GPP TS 26.404, Enhanced aacPlus encoder SBR part,"* June 2007.

[10] *"Coding of moving pictures and audio, subpart 8: Technical description of parametric coding for high quality audio,"* Draft ISO/IEC 14496-3 (Audio 3rd Edition).

[11] H. Purnhagen, "Low complexity parametric stereo coding in MPEG-4,"in *Proc. 7th Int. Conf. on Audio Effects (DAFX-04)*, Naples, Italy, Oct. 2004.

[12] E. Schuijers, J. Breebaart, H. Purnhagen, and J. Engdegård, "Low complexity parametric stereo coding," in *Proc. AES 116th conv.*, Berlin, Germany, May 2004, preprint 6073.

[13] C. Faller and F. Baumgarte, "Efficient representation of spatial audio using perceptual parametrization," in *Proc. IEEE Workshop on Applicat. Signal Process. Audio Acoust.*, New Paltz, NY, USA, 2001, pp. 199-202.

[14] F. Baumgarte and C. Faller, "Binaural cue coding - part i: psychoacoustic fundamentals and design principles," *IEEE Trans. Speech Audio Process.*, vol. 11, pp. 509-519, no. 6, Nov. 2003.

[15] C. Faller and F. Baumgarte, "Binaural cue coding - part ii: schemes and applications," *IEEE Trans. Speech Audio Process.*, vol. 11, no. 6, pp. 520-531, Nov. 2003.

[16] C. Faller, "Parametric coding of spatial audio," in *Proc. 7th Int. Conf. on Audio Effects (DAFX-04)*, Naples, Italy, Oct. 2004.

[17] A. Seefeldt, M. S. Vinton, and C. Q. Robinson, "New techniques in spatial audio coding," in *Proc. AES 119th conv.*, New York, USA, Oct. 2005, preprint 6587.

[18] "AES technical committee of coding of audio signals: Perceptual audio coders: What to listen for", Audio Engineering Society Publications, 2001, CD-ROM with tutorial information and audio examples.

[19] T. Painter and A. Spanias, "Perceptual coding of digital audio," *Proc. IEEE*, vol. 88, no. 4, pp. 451-515, Apr. 2000.

[20] J. D. Johnston, "Perceptual audio coding—A history and timeline," in *Proc. 41st Asilomar Conf.on Signals, Systems, and Computers*, Pacific Grove, CA, USA, Nov. 4-7, 2007, pp. 2085-2087.

[21] K. Brandenburg, "Low bitrate audio coding—state-of-the-art, challenges and future directions," in *Proc. IEEE Int. Conf. Commun. Technol. (ICCT'00)*, vol. 1, Beijing, China, Aug. 21-25, 2000, pp. 594-597.

[22] P. Noll, "High quality audio for multimedia: key technologies and MPEG standards," in *Proc. IEEE Global Telecommun. Conf. (GLOBECOM)*, vol. 4, Rio de Janeiro, Brazil, Nov. 1999, pp. 2045-2050.

[23] P. Noll, "MPEG digital audio coding," *IEEE Signal Process. Mag.*, vol. 14, pp. 59–81, Sep. 1997.

[24] A. C. den Brinker, J. Breebaart, P. Ekstrand, J. Engdegård, F. Henn, K. Kjörling, W. Oomen, and H. Purnhagen, "An overview of the coding standard MPEG-4 audio amendments 1 and 2: HE-AAC, SSC, and HE-AAC v2," *EURASIP J. Audio, Speech, Music Process.*, vol. 2009, article ID 468971.

[25] "Plus V specification," [online] http://www.mp3-tech.org/programmer/docs/plusv.pdf.

[26] M. H. Cheng and Y. H. Hsu, "Fast IMDCT and MDCT Algorithms—A Matrix Approach," *IEEE Trans. Signal Process.*, vol. 51, pp. 221-229, Jan. 2003.

[27] J. Herre and J. D. Johnston, "Enhancing the performance of perceptual audio coders by using Temporal Noise Shaping (TNS)," in *Proc. AES 101st Conv.*, Los Angeles, CA, Nov. 1996, preprint 4384.

[28] J. Herre and J. D. Johnston, "Continuously signal-adaptive filterbank for high-quality perceptual audio coding," in *Proc. IEEE ASSP Workshop*, Oct. 1997.

[29] J. Herre and J. D. Johnston, "Exploiting both time and frequency structure in a system that uses an analysis/synthesis filterbank with high frequency resolution," in *Proc. AES 103rd Conv.*, New York, Sep. 1997, preprint 5419.

[30] J. Herre, "Temporal noise shaping, quantization and coding methods in perceptual audio coding: A tutorial introduction," in *Proc.17th AES Int. Conf.: High-Quality Audio Coding*, Sep. 1999, pp. 17–31.

[31] N. S. Jayant and P. Noll, *Digital Coding of Waveforms*. Englewood Cliffs, NJ: Prentice–Hall, 1984.

[32] P. J. Davis, *Circulant Matrices*, New York: John Willey and Sons, 1979.

[33] C.M. Liu, W.C. Lee, C.H. Yang, K.Y. Peng, T. Chiou, T.W. Chang, Y.H. Hsiao, H.W. Hsu, and C.T. Chien, "Design of AAC encoders," in *Proc. AES 117th Conv.*, San Francisco, USA, Oct. 2004, preprint 6201.

[34] E. Allamanche, R. Geiger, J. Herre, and T. Sporer, "MPEG-4 low delay audio coding based on the aac codec," in *Proc. AES 106th Conv.*, Munich, Germany, May 1999, preprint 4929.

[35] P. Marins, F. Rumsey, and S. Zielinski, "The relationship between selected artifacts and basic audio quality in perceptual audio codecs," in *Proc. AES 120th conv.* Paris, France, May 2006, preprint 6745.

[36] C.M. Liu, W.C. Lee, and H.W. Hsu, "High frequency reconstruction by linear extrapolation," in *Proc. AES 115th Conv.*, New York, USA, Oct. 2003, preprint 5968.

[37] H.W. Hsu, C.M. Liu, and W.C. Lee, "Audio Patch method in audio decoders—MP3 and AAC," in *Proc. AES 116th Conv.*, Berlin, Germany, May 2004, preprint 6014.

[38] H.W. Hsu, C.M. Liu, W.C. Lee, and Z.W. Li, "Audio patch method in MPEG-4 HE AAC decoder," in *Proc. AES117th Convention*, San Francisco, USA, Oct. 2004, preprint 6221.

[39] E. Larsen, M. Danessis, and R. Aarts, "Efficient high-frequency bandwidth extension of music and speech," in *Proc. AES 112nd Conv.*, Munich, Germany, May 2002, preprint 5627.

[40] R. M. Aarts, E. Larsen, and O. Ouweltjes, "A unified approach to low- and high-frequency bandwidth extension," in *Proc. AES 115th Conv.*, New York, USA, Oct. 2003, preprint 5921.

[41] A. J. S. Ferreira and D. Sinha, "Accurate spectral replacement," in *Proc. AES 118th conv.*, Barcelona, Spain, May 2005, preprint 6383.

[42] D. Sinha, A. J. S. Ferreira, and D. Sen, "A fractal self-similarity model for the spectral representation of audio signals," in *Proc. AES 118th conv.*, Barcelona, Spain, May 2005, preprint 6467.

[43] D. Sinha, A. Ferreira and E.V. Harinaryanan, "A novel integrated audio bandwidth extension toolkit (ABET)," in *Proc. AES 120th conv.*, Paris, France, May 2006, preprint 6788.

[44] S. H. Oh, W. J. Yoon, Y. H. Cho, K. S. Park, and K. M. Kim, "A new spectral enhancement algorithm in MP3 audio," *IEEE Trans. Consumer Electron.*, vol. 52, no. 1, pp. 196-199, Feb. 2006.

[45] C. W. Kok, "Fast algorithm for computing discrete cosine transform," *IEEE Trans. Signal Process.*, vol. 45, no. 3, pp. 757-760, Mar. 1997.

[46] B. G. Lee, "A new algorithm to compute the discrete cosine transform," *IEEE Trans. Acoust., Speech, Signal Process.*, vol. 32, no. 6, pp. 1243 -1245, Dec. 1986.

[47] G. Bi and Lee W. Yu, "DCT algorithms for composite sequence lengths," *IEEE Trans. Signal Process.*, vol. 46, no. 3, pp. 554-562, Mar. 1998.

[48] G. Bi, "Fast algorithms for type-III DCT of composite sequence lengths," *IEEE Trans. Signal Process.*, vol. 47, no. 7, pp. 2053-2059, July 1990.

[49] Z. WANG, "Fast algorithms for the discrete W transform and for the discrete Fourier transform," *IEEE Trans. Acoust., Speech, Signal Process.*, vol. 32, no. 4, pp. 803-816, Aug. 1984.

[50] V. Britanak, "The fast DCT-IV/DST-IV computation via the MDCT," *Signal Process.*, vol. 83, no. 8, pp. 1803-1813, Aug. 2003.

[51] B. C. J. Moore, *An Introduction to the Psychology of Hearing*, 2nd ed., New York: Academic, 1982.

[52] A.V. Oppenheim, R.W. Schafer, and J.R. Buck, *Discrete-Time Signal Processing*, 2nd ed. Upper Saddle River, NJ: Prentice-Hall, 1999.

[53] S. M. Kay and S. L. Marple, Jr., "Spectrum analysis—a modern perspective," *Proc. IEEE*, vol. 69, no. 11, pp. 1380–1419, Nov. 1981.

[54] S. M. Kay, "Maximum entropy spectral estimation using the analytic signal," *IEEE Trans. Acoust., Speech, Signal Process.*, vol. ASSP-26, pp. 467-469, Oct. 1978.

[55] L. B. Jackson, D. W. Tufts, F. K. Soong and R. M. Rao, "Frequency estimation by linear prediction," in *Proc. IEEE ICASSP*, pp.332-356, 1978.

[56] S. M. Kay, "Fourier-autoregressive spectral estimation," in *Proc. IEEE ICASSP*, pp.162-165, 1979.

[57] M. P. Quirk and B. Liu, "Improving resolution for autoregressive spectral estimation by decimation," *IEEE Trans. Acoust., Speech, Signal Process.*, vol. ASSP-31, pp.630-637, Jun. 1983.

[58] T. Shimamura, N. Sakaguchi, and S. Takahashi, "Frequency estimation using the analytic signals by decimation," in *Proc. 1989 IEEE Pacific Rim Conf. on Commun., Computers, Signal Process. (PACRIM 1989),* Victoria, B.C., Canada, 1-2 Jun. 1989, pp.540-543.

[59] M. Briand, D. Virette, and N. Martin, "Parametric coding of stereo audio based on principal component analysis," in *Proc. 9th Int. Conf. on Audio Effects (DAFX-06)*, Montreal, Canada, Sep. 2006.

[60] M. Briand, D. Virette, and N. Martin, "Parametric representation of multichannel audio coding based on principal component analysis," in *Proc. AES 120th conv.*, Paris, France, May 2006, preprint 6813.

[61] C. H. Yang, C. M. Liu, H. W. Hsu, K. C. Lee, S. H. Tang, Y. C. Yang, C. M. Chang, and W. C. Lee, "Design of MPEG-4 HEAAC version 2 encoder," in *Proc. AES 121st Conv.*, San Francisco, USA, Oct. 2006, preprint 6873.

[62] A. Rezayee and S. Gazor, "An adaptive KLT approach for speech enhancement," *IEEE Trans. Speech Audio Process.*, vol. 9, no. 2, pp. 87-95, Feb. 2001.

[63] Charpentier F. and Stella M., "Diaphone synthesis using an overlap-add technique for speech waveforms concatenation," in *Proc. IEEaE Int. Conf. Acoust. Speech Signal Process.*, Tokyo, Japan, 1986, pp. 2015-2018.

[64] J. Makhoul, "Linear prediction: a tutorial review," *Proc. IEEE*, vol. 63, no. 4, pp. 561–580, Apr. 1975.

[65] Audio lossless coding (ALS), new audio profiles and BSAC extensions, ISO/IEC, 14496-3:2005/Amd 3:2006.

[66] A. Härmä and U. K. Laine, "A comparison of warped and conventional linear predictive coding," *IEEE Trans. Speech, Audio, Process.*, vol. 9, no. 5, pp. 579–588, July 2001.

[67] M. Deriche and D. Ning, "A novel audio coding scheme using warped linear prediction model and the discrete wavelet transform," *IEEE Trans. Audio, Speech, Lang. Process.*, vol. 14, no. 6, pp. 2039–2048, Nov. 2006.

[68] R. Kumaresan, "An inverse signal approach to computing the envelope of a real valued signal," *IEEE Signal Process. Lett.*, vol. 5, no. 10, pp. 256–259, Oct. 1998.

[69] R. Kumaresan and A. Rao, "Model-based approach to envelope and positive instantaneous frequency estimation of signals with speech applications," *J. Acoust. Soc. Amer.*, vol. 105, no. 3, pp. 1912–1924, Mar. 1999.

[70] R. Kumaresan, "On minimum/maximum/all-pass decompositions in time and frequency domains," *IEEE Trans. Signal Process.*, vol. 48, no. 10, pp. 2973–2976, Oct. 2000.

[71] R. Kumaresan and Y.Wang, "On the relationship between line-spectral frequencies and zero-crossings of signals," *IEEE Trans. Speech Audio Process.*, vol. 9, no. 4, pp. 458–461, May 2001.

[72] R. Kumaresan and Y. Wang, "On representing signals using only timing information," *J. Acoust. Soc. Amer.*, vol. 110, no. 5, pp. 2421–2439, Nov. 2002.

[73] M. Athineos and D. Ellis, "Autoregressive modeling of temporal envelopes," *IEEE Trans. Signal Process.*, vol. 55, no. 11, pp. 5237–5245, Nov. 2007.

[74] J. P. Princen, A. W. Johnson, and A. B. Bradley, "Subband/transform coding using filter bank designs based on time domain aliasing cancellation," in *Proc. IEEE ICASSP'87*, Dallas, TX, Apr. 1987, pp. 2161–2164.

[75] H. S. Malvar, *Signal Processing with Lapped Transforms*, Norwood, MA: Artech House, 1992.

[76] S. A. Martucci, "Symmetric convolution and the discrete sine and cosine transforms," *IEEE Trans. Signal Process.*, vol. 42, no. 5, pp.1038–1051, May 1994.

[77] G. Bongiovanni, P. Corsini, and G. Frosini, "One-dimensional and two-dimensional generalized discrete Fourier transforms," *IEEE Trans. Acoust., Speech, Signal Process.*, vol. ASSP–24, pp. 97–99, Feb. 1976.

[78] J. L. Vemet, "Real signals fast Fourier transform: storage capacity and step number reduction by means of an odd discrete Fourier transform," *Proc. IEEE*, vol. 59, pp. 1531–1532, Oct. 1971.

[79] L. S. Marple, Jr., "Computing the discrete-time 'analytic' signal via FFT," *IEEE Trans. Signal Process.*, vol. 47, no. 9, pp. 2600–2603, Sep. 1999.

# VITA

**Han-Wen Hsu** was born in Tainan, Taiwan in Oct. 1977. He received his B.S. degree from the Division of Applied Mathematics, the Department of Mathematics, National Tsing Hua University, Hsinchu, Taiwan in June 2000. He received his M.S. degree from the Department of Computer Science and Information Engineering, National Chiao Tung University, Hsinchu, Taiwan in June 2004, where he is currently working toward a Ph. D. degree in Computer Science and Engineering. His research interests are in audio coding and signal processing.
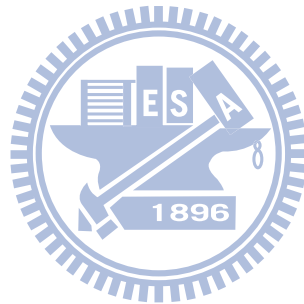
# PUBLICATION LIST

## Journal Papers

1. C.M. Liu, **H.W. Hsu**, and W.C. Lee, "Compression artifacts in perceptual audio coding," *IEEE Trans. Audio Speech Lang. Process.*, vol. 16, no. 4, pp. 681-695, May 2008.

2. **H.W. Hsu** and C.M. Liu, "Fast radix-*q* and mixed-radix algorithms for type-IV DCT," *IEEE Signal Process. Lett.*, vol. 15, pp.910-913, Dec. 2008.

3. **H.W. Hsu** and C.M. Liu, "Autoregressive modeling of temporal/spectral envelopes with finite-length discrete trigonometric transforms," Accepted with minor revisions, *IEEE Trans. Signal Process.*, 2010.

4. **H.W. Hsu** and C.M. Liu, "Decimation-whitening filter in spectral band replication," submit to *IEEE Trans. Audio Speech Lang. Process.*, 2010.

## Conference Papers

1. D.P. Chen, H.F. Hsiao, **H.W. Hsu**, and C.M. Liu, "Gram-Schmidt-based downmixer and decorrelator in the MPEG Surround Coding," appear to *Proc. AES 128th Conv.*, London, UK, May 22–25, 2010.

2. C. M. Liu, **H. W. Hsu**, Y. H. Kao, and W. C. Lee, "Spatial parameter decision by least squared error in Parametric Stereo Coding and MPEG Surround," in *Proc. AES 126th Conv.*, Munich, Germany, May 7–10, 2009, preprint 7731.

3. C.M. Liu, **H.W. Hsu**, C.H. Yang, and W.C. Lee, "Low-power MPEG-4 HE-AAC version-2 encoder," in *Proc. AES 124th Conv.*, Amsterdam, Netherlands, May 17–20, 2008, preprint 7338.

4. C.M. Liu, C.H. Yang, **H.W. Hsu**, and W.C. Lee, "Design of framing in MPEG Surround based on dynamic programming algorithm," in *Proc. AES 124th Conv.*, Amsterdam, Netherlands, May 17–20, 2008, preprint 7487.

5. **H.W. Hsu**, C.L Hu, C.M Liu, and W.C. Lee, "On the design of low power MPEG-4 HE-AAC encoders," in *Proc. AES 122nd Conv.*, Vienna, Austria, May 5–8, 2007, preprint 6999.

6. **H.W. Hsu**, H.Y. Tseng, C.M Liu, W.C. Lee, and C. H. Yang, "High quality, low power QMF bank design for SBR, Parametric Coding, and MPEG Surround decoders," in *Proc. AES 122nd Conv.*, Vienna, Austria, May 5–8, 2007, preprint 7000.

7. C.H. Yang, C. M. Liu, **H.W. Hsu**, K.C. Lee, S.H. Tang, Y.C. Yang, C.M. Chang, and W.C. Lee, "Design of HE-AAC version 2 encoder," in *Proc. AES 121st Conv.*, San Francisco, USA, October 5–8, 2006, preprint 6873.

8. **H.W. Hsu**, C.M. Liu, and W.C. Lee, "Fast complex quadrature mirror filterbanks for

MPEG-4 HE-AAC," in *Proc. AES 121st Conv.*, San Francisco, USA, October 5–8, 2006, preprint 6871.

9.  C. M. Liu, **H. W. Hsu**, C. H. Yang, K. C. Lee, S. H. Tang, Y. C. Yang, and W. C. Lee, "Compression artifacts in perceptual audio coding," in *Proc. AES 121st Conv.*, San Francisco, USA, October 5–8, 2006, preprint 6872.

10. **H.W Hsu**, Y.C Yang, C.M. Liu, and W.C Lee, " Design for high frequency adjustment module in MPEG-4 HEAAC encoder based on linear prediction method," in *Proc. AES120th Conv.*, Paris, France, May 20–23, 2006, preprint 6755.

11. K.C. Lee, C.H. Yang, **H.W. Hsu**, W.C. Lee, C.M. Liu, and T.W. Chang, "Efficient design of time-frequency stereo parameter sets for parametric HE-AAC," in *Proc.* AES 119th Conv., New York, USA, October 7–10, 2005, preprint 6600.

12. C.M. Liu, L.W. Chen, **H.W. Hsu**, and W.C. Lee, "Bit reservoir design for HE-AAC," in *Proc.* AES 118th Conv., Barcelona, Spain, May 28-31, 2005, preprint 6382.

13. C.M. Liu, W.C. Lee, C.H. Yang, K.Y. Peng, T. Chiou, T.W. Chang, Y.H. Hsiao, **H.W. Hsu**, and C.T. Chien, "Design of MPEG-4 AAC encoders," in *Proc. AES 117th Conv.*, San Francisco, USA, Oct. 28-31, 2004, preprint 6201.

14. **H.W. Hsu**, C.M. Liu, W.C. Lee, and Z.W. Li, "Audio patch method in MPEG-4 HE AAC decoder," in *Proc. AES 117th Conv.*, San Francisco, USA, Oct. 28-31, 2004, preprint 6221.

15. **H. W. Hsu**, C. M. Liu, and W. C. Lee, "Audio patch method in audio decoders—MP3 and AAC," in *Proc. AES 116th Conv.*, Berlin, Germany, May 8-11, 2004, preprint 6014.

16. C. M. Liu, W. C. Lee, and **H. W. Hsu**, "High frequency reconstruction for band-limited audio signal," in *Proc. the 6th Int. Conf. Digital Audio Effects (DAFX-03)*, University of London, September 8-11, 2003.

17. C. M. Liu, W. C. Lee, and **H. W. Hsu**, "High frequency reconstruction by linear extrapolation", in *Proc. AES115th Conv.*, New York, USA, Oct. 10-13, 2003, preprint 5968.